

FAULT-TOLERANT CONTROL OF HYDRAULICALLY-POWERED  
ACTUATORS USING FRACTIONAL-ORDER PID SCHEMES

by

Ali Maddahi

A thesis submitted to the Faculty of Graduate Studies of  
The University of Manitoba  
in partial fulfillment of the requirements for the degree of

Doctor of Philosophy

Department of Mechanical Engineering  
University of Manitoba  
Winnipeg, Manitoba, Canada

Copyright © 2019 Ali Maddahi

## ABSTRACT

Hydraulic actuators are used extensively in various equipment including aircraft, robots and heavy-duty machinery. One of the common problems in hydraulic systems is occurrence of faults such as the actuator internal leakage. Some faults need to be detected properly to prevent actuator malfunctioning. For example, the internal leakage deteriorates the system performance as it causes the fluid to move between cylinder chambers. Model-based fault detection techniques require a model of the hydraulic actuator and faults or an estimation of system parameters. In practice, there is no accurate model to describe some faults. Application of *data-driven fault detection techniques* is more desirable.

One of the main challenges, due to the faults, in hydraulic actuation systems is the controller design. If a controller is not able to compensate for fault effects, it may lead to considerable losses. Therefore, there is a need for designing fault-tolerant controllers (FTCs). *Data-driven techniques of controller design* are good solutions to overcome challenges associated with obtaining models or estimating system and fault parameters.

In this thesis, the applications of data-driven techniques of the fault detection and controller design to the hydraulic actuators are investigated and exemplified with detection of the internal leakage fault and design of a control system tolerant to the leakage. First, a set of multiscale measures is quantified in various healthy and faulty operating modes and a comparison is carried out, between the measures, to identify the most reliable indicator(s) in detecting various levels of

the leakage. Comparison results indicate that the wavelet transform is the best technique, amongst the employed multiscale measures, for the internal leakage detection. Next, a fractional-order PID (FOPID) position controller is designed using experimental data. Efficacy of the designed controller in tracking various reference inputs, in presence of different system uncertainties, is examined through experiments. Finally, a methodology is developed for designing an FOPID-based FTC that does not require a prior knowledge about the model and parameters of the system and fault or emulation of the fault in experimental setup. The methodology is based on introduction of a set of synthetic errors to the hydraulic actuator. Experimental results prove that the methodology works well for a hydraulic actuator experiencing the internal leakage.

## ACKNOWLEDGMENT

My first and special acknowledge needs to go to my advisor, Dr. Nariman Sepehri whose support and encouragement have always been invaluable. My profound gratitude is extended to Dr. Witold Kinsner who taught me how to do fundamental research. Many thanks to Dr. Qing Zhao, from the University of Alberta, and Dr. Subramaniam Balakrishnan, from the University of Manitoba, for serving on my Ph.D. examining committee and for their constructive comments on this thesis.

Special thanks are also due to my parents for encouragement and for supplying incentive to finish. I owe a big debt of appreciation to my wife, Parisa, and my brothers, Yaser, Saeid and Vahid who encouraged me to develop my strengths and work hard on my weaknesses.

Thanks to the NSERC and the University of Manitoba for providing financial support during my Ph.D. program. Thanks to Shahriar Bagheri, Vikram Banthia, Maziar Mardan, Dr. Ehsan Jalayeri, Alireza Asadi, Guangan Ren and my other peers in the “Fluid Power and Telerobotics Research Laboratory” at the University of Manitoba.

Lastly, I would like to thank all of the friends during my years at the University of Manitoba who supplied the ridiculous moments to compliment my otherwise sublime life as a graduate student.

# TABLE OF CONTENT

ABSTRACT .....	I
ACKNOWLEDGMENT .....	III
LIST OF FIGURES .....	VII
LIST OF TABLES .....	XI
LIST OF NOMENCLATURES .....	XII
LIST OF ACRONYMS .....	XV
<b>1. INTRODUCTION</b> .....	<b>1</b>
1.1. Motivation .....	1
1.2. Problem Statement .....	2
1.2.1. Problem Definition .....	2
1.2.2. Proposed Solutions .....	4
1.3. Thesis Formulation .....	5
1.3.1. Thesis Statement .....	5
1.3.2. Thesis Objectives .....	5
1.3.3. Research Questions .....	6
1.3.4. Methods and Techniques .....	6
1.4. Thesis Organization .....	8
<b>2. RELEVANT BACKGROUND</b> .....	<b>10</b>
2.1. Fault Detection in Hydraulic Actuators .....	10
2.2. Controller Design in Hydraulic Actuators .....	13
2.3. Summary .....	17
<b>3. EXPERIMENTAL SETUP</b> .....	<b>18</b>
3.1. Test Rig .....	18
3.2. Mathematical Model .....	23
<b>4. ACTUATOR INTERNAL LEAKAGE DETECTION</b> .....	<b>25</b>
4.1. Data Collection .....	26

4.2. Analysis Procedure .....	29
4.2.1. Fundamental Tests .....	29
4.2.1.1. Stationarity Test.....	29
4.2.1.2. Sampling Test .....	31
4.2.1.3. Fractality Test.....	34
4.2.1.4. Tsonis Test.....	38
4.2.2. Preliminary Calculations .....	40
4.2.2.1. Optimum Lag.....	41
4.2.2.2. Reconstruction of Embedding Space.....	42
4.2.2.3. Minimum Embedding Dimension .....	44
4.2.3. Quantification of Multiscale Measures .....	46
4.2.3.1. Correlation Fractal Dimension .....	47
4.2.3.2. Variance Fractal Dimension .....	49
4.2.3.3. Maximal Lyapunov Exponent .....	50
4.2.3.4. Correlation Entropy .....	52
4.2.3.5. Wavelet Transform .....	54
4.3. Results and Discussion .....	58
4.4. Leakage Detection Using Displacement Error Data.....	60
4.5. Summary .....	66
<b>5. POSITION CONTROLLER DESIGN</b> .....	<b>67</b>
5.1. Fractional-order Operators.....	68
5.1.1. Advantages of Different Definitions of Fractional Operators.....	70
5.1.2. Disadvantages of Different Definitions of Fractional Operators .....	71
5.1.3. Geometric and Physical Meanings of Fractional-order Operators.....	71
5.2. Approximation of Fractional-order Operators in Laplace Domain .....	81
5.3. Fractional-order PID Controllers .....	85
5.4. Controller Parameters Tuning.....	85
5.5. Design Procedure .....	90
5.6. Results and Discussion .....	92
5.7. Summary .....	106
<b>6. FAULT-TOLERANT CONTROLLER DESIGN</b> .....	<b>107</b>
6.1. Introduction of Synthetic Error .....	108
6.2. Wavelet Analysis .....	110
6.3. Controller Design for Faulty Operating Modes .....	115
6.4. Prefilter Design .....	119
6.5. Results and Discussion .....	123
6.6. Summary .....	129

<b>7. CONCLUSIONS</b>	<b>131</b>
7.1. Thesis Contributions .....	131
7.2. Thesis Conclusions .....	133
7.3. Extension of This Work .....	134
APPENDIX A – COMPARISON BETWEEN FOPID CONTROLLERS .....	135
APPENDIX B – STABILITY ANALYSIS .....	139
REFERENCES .....	145

# LIST OF FIGURES

<b>Figure 3.1</b> Experimental setup of valve-controlled hydraulic actuator with data acquisition system. ....	19
<b>Figure 3.2</b> Schematic of valve-controlled hydraulic actuator. ....	20
<b>Figure 3.3</b> Setup of internal leakage emulator comprising ball valve, needle valve and flowmeter. Needle valve is used to change level of leakage. Flowmeter measures flow rate of internal leakage between two chambers. ....	21
<b>Figure 3.4</b> (a) Extra masses added to main actuator in order to investigate effect of change in inertia on performance of controller; (b) slave actuators are connected in parallel to main actuator to emulate changes in friction as well as inertia. ....	22
<b>Figure 3.5</b> Setup of loading actuation system used to apply controlled force to main actuator. .	23
<b>Figure 4.1</b> Steps followed to quantify multiscale measures. ....	26
<b>Figure 4.2</b> Typical signals taken from an experiment in healthy operating mode ( $\bar{Q}_l = 0.09 L/min$ ). ....	27
<b>Figure 4.3</b> Pressure data ( $P_1$ ) and corresponding internal leakage flow rates ( $\bar{Q}_l$ ) taken from experimental setup in three levels of leakage: (a) small leakage ( $\bar{Q}_l = 0.22 L/min$ ), (b) medium leakage ( $\bar{Q}_l = 0.65 L/min$ ), and (c) large leakage ( $\bar{Q}_l = 1.19 L/min$ ). ....	28
<b>Figure 4.4</b> Autocorrelation (AC) and mean of signal $P_1$ ( $\mu_{P_1}$ ) at sliding window size of 1000 samples, step size of 50 and lag of 1. Time interval of [2, 10] sec is equivalent to samples of [2001, 10000]. ....	31
<b>Figure 4.5</b> Typical representation of power spectral density of (a) narrowband and (b) broadband signals. ....	32
<b>Figure 4.6</b> Normalized power spectral density of signal $P_1$ taken from an experiment in healthy operating mode. Highest frequency component is estimated at $\log(f_h) = 2.47$ . ....	34
<b>Figure 4.7</b> Typical representation of fractal: (a) a non-fractal curve; (b) a fractal curve (Koch curve). Both curves have $D_T = 1$ and $D_E = 2$ . ....	35
<b>Figure 4.8</b> Successive dilations of chamber one pressure signal ( $P_1$ ) taken from an experiment in healthy operating mode. Samples of interval [2001, 10000] are equivalent to time interval of [2, 10] sec. ....	37

**Figure 4.9** Log-log plot for calculating box-counting dimension. Line is obtained using linear Least Squares technique. Slope of line reflects box-counting dimension. .... 39

**Figure 4.10** Mutual information ( $I$ ) in terms of different lags ( $\tau$ ); Results were obtained by applying mutual information technique to pressure data  $P_1$  of Figure 4.2. .... 42

**Figure 4.11** Cao’s index ( $E_1$ ) as a function of embedding dimension ( $m$ ). Plot was obtained by calculating  $E_1$  of pressure signal of Figure 4.2. .... 46

**Figure 4.12** Representation of log-log plot for calculation of correlation fractal dimension. Line is obtained from linear Least Square regression of scattered points. Slope of line is equal to correlation dimension. .... 48

**Figure 4.13** Log-log plot of variance of amplitude increments vs. different data window sizes. Line is obtained using linear Least Squares method. Hurst exponent equals half the slope value. .... 50

**Figure 4.14** Plot of index  $L_k$  in terms of different time steps  $k$  for determining maximal Lyapunov exponent. Slope ( $\lambda_1$ ) equals maximal Lyapunov exponent. .... 51

**Figure 4.15** Plot of  $\log(C_r)$  vs.  $\log(r)$  for different embedding dimensions ( $m = 6, \dots, 13$ ). ... 53

**Figure 4.16** Plot of index  $K_{2,r}$  in terms of embedding dimension  $m$ . .... 53

**Figure 4.17** Schematic of multiresolution signal decomposition technique based on quadrature mirror filter pair [12]. Two levels of decomposition are illustrated. .... 56

**Figure 4.18** Detailed coefficients of  $P_1$  of healthy hydraulic actuator. Time interval of [5.5, 6.5] sec is equivalent to samples of [5501, 6500]. .... 57

**Figure 4.19** Approximation coefficients of  $P_1$  of healthy hydraulic actuator. .... 57

**Figure 4.20** Block diagram of closed-loop positioning system for a hydraulic actuator experiencing internal leakage:  $r$  denotes reference input;  $u$  is control signal;  $e_r$  is displacement error and  $y$  is piston position measured by encoder. .... 61

**Figure 4.21** Error signal,  $e_r$ , of healthy and faulty operating modes based on fixed-step reference input of 5 mm. Close-up version shows behavior of error signal over interval [0.4, 1] sec. .... 62

**Figure 4.22** Error signal,  $e_r$ , of seven operating modes considering variable-step input. Average value of internal leakage flow rate varies from almost zero to 3.24 L/min. .... 64

**Figure 5.1** Graph of  $f(x) = x^3$  with triangle generated by fractional order derivative ( $\alpha = 0.5$ ). .... 74

**Figure 5.2** Behavior of function  $h_\alpha(t)$  for various values of  $\alpha$ . .... 77

**Figure 5.3** Integration and differentiation operators in Laplace domain: (a) first-order integer operator; (b) fractional-order operator;  $\alpha$  is a non-integer value. .... 81

**Figure 5.4** Bode plot of  $s^\alpha$  for various values of  $\alpha$  between 0 and 1. .... 84

**Figure 5.5** Block diagram of control system:  $C$  is controller;  $r$  denotes reference signal;  $u$  is control signal;  $v$  represents output disturbance applied to output  $y$ . .... 86

**Figure 5.6** Steps of FOPID controller design based on Oustaloup and IFT techniques. .... 91

<b>Figure 5.7</b> Performance of FOPID and QFT controllers in tracking a step input of 5 mm pushing against a spring with stiffness of 160 kN/m. $x_p$ represents piston displacement, and $u$ is control signal. ....	96
<b>Figure 5.8</b> Tracking responses to: (a) alternating step inputs and (b) random step inputs. Actuator is pushing against the spring with stiffness of 160 kN/m. ....	97
<b>Figure 5.9</b> Tracking responses to sinusoidal input. Stiffness of spring is 160 kN/m. ....	98
<b>Figure 5.10</b> Error signals and control inputs of five separate experiments showing robustness of FOPID controller when piston tracks step input of 5 mm. Stiffness of springs are equal to 45 kN/m, 80 kN/m and 160 kN/m, and extra masses and slave actuators are added to main actuator. ....	100
<b>Figure 5.11</b> Set of five experimental results considering various system uncertainties. Tracking responses of all experiments are comparable indicating robustness of FOPID controller. ....	101
<b>Figure 5.12</b> Result of tracking step input of 30 mm when actuator experiences a sudden external force: (a) piston displacement; (b) control input. Stiffness of spring is 160 kN/m. ....	102
<b>Figure 5.13</b> Block diagram of hydraulic actuation system with load emulator; $x_{p,ref}$ and $x_{p,act}$ are position reference input and actual position, respectively; $F_{ext,ref}$ and $F_{ext,act}$ are desired and actual forces, respectively. ....	103
<b>Figure 5.14</b> Tracking of variable-step piston displacement when actuator is under variable-step external load. ....	104
<b>Figure 5.15</b> Resulting position of hydraulic actuator under sinusoidal external load. ....	105
<b>Figure 6.1</b> Variable-step reference input ( $x_{p,ref}$ ) ....	109
<b>Figure 6.2</b> Seven levels of synthetic error ( $e_{syn}$ ) generated based on reference input of different magnitudes. Synthetic errors range from 5% to 65% resembling effect of “very small” to “very large” internal leakage on piston displacement, respectively. ....	110
<b>Figure 6.3</b> Block diagram of closed-loop system affected by synthetic error: $r$ denotes reference input; $u$ is control signal; $e_c$ is controller input; $e_{syn}$ represents synthetic error introduced to closed-loop system; $e_r$ is error between reference input and plant output. FOPID control scheme is presented by Eq. (6.3). ....	111
<b>Figure 6.4</b> Typical error signals, $e_r$ , corresponding to three levels of synthetic errors. ....	112
<b>Figure 6.5</b> Block diagram of closed-loop system consisting of a two-degree of freedom fault-tolerant controller. ....	119
<b>Figure 6.6</b> Tracking responses to alternating step input in four operating modes NL, SL, ML and LL: (a) piston position; (b) close-up of piston position response. ....	124
<b>Figure 6.7</b> (a) control signals corresponding to each level of internal leakage introduced to hydraulic actuator when tracking alternating step input of Figure 6.6; (b) leakage flow rates. .	125
<b>Figure 6.8</b> Tracking responses to alternating step input of high magnitudes in four operating modes: (a) position response; (b) leakage flow rates. ....	126

<b>Figure 6.9</b> Tracking responses to step inputs of 10 mm, 15 mm and 25 mm, each in four operating modes: (a) position response; (b) leakage flow rates. ....	127
<b>Figure 6.10</b> Tracking responses to step input of 20 mm in presence of varying internal leakage: (a) displacement response; (b) leakage flow rates. ....	129
<b>Figure A.1</b> Tracking responses to step input of 10 mm when no prefilter is used and there is no internal leakage in the hydraulic actuator. ....	136
<b>Figure A.2</b> Tracking responses to step input of 20 mm with prefilter and no internal leakage. ....	136
<b>Figure A.3</b> Tracking responses to step input of 20 mm when there is a large internal leakage ( $\bar{Q}_l = 11.19 L/min$ ). No prefilter is used. ....	137
<b>Figure A.4</b> Tracking responses to step input of 20 mm with prefilter and large internal leakage ( $\bar{Q}_l = 11.3 L/min$ ). ....	137
<b>Figure A.5</b> Control signals generated by FTC in healthy operating mode with and without prefilter. ....	137
<b>Figure B.1</b> Input signal given to servovalve in open-loop configuration. ....	140
<b>Figure B.2</b> Piston displacement data measured by position encoder of test rig. ....	141
<b>Figure B.3</b> Outputs obtained from transfer functions $G_1(s)$ and $G_2(s)$ . ....	141
<b>Figure B.4</b> Nyquist diagram of open-loop transfer function $C_{FTC}(s)G_1(s)$ . ....	142
<b>Figure B.5</b> Nyquist diagram of open-loop transfer function $C_{FTC}(s)G_2(s)$ . ....	143

## LIST OF TABLES

<b>Table 4.1</b> Mean and variance of pressure signal at different dilation levels. ....	37
<b>Table 4.2</b> Reconstruction of embedding space based on embedding dimension and lag. ....	43
<b>Table 4.3</b> Multiscale measures obtained in healthy and faulty operating modes. Three experiments were conducted in each operating mode. ....	58
<b>Table 4.4</b> Percentage of change of average values of multiscale measures in faulty modes with respect to those of healthy operating mode. ....	60
<b>Table 4.5</b> Wavelet detailed coefficients of displacement error data obtained from healthy and faulty operating modes. Reference signal is step input of 5 mm. ....	63
<b>Table 4.6</b> Percentage of change of average values of wavelet detailed coefficients in faulty modes with respect to those of healthy operating mode. Reference signal is step input of 5 mm. ....	63
<b>Table 4.7</b> Wavelet detailed coefficients of displacement error data obtained from healthy and faulty operating modes. Reference signal is a variable-step input. ....	65
<b>Table 4.8</b> Percentage of change of average values of wavelet detailed coefficients in faulty modes with respect to those of healthy operating mode. Reference signal is a variable-step input. ....	65
<b>Table 5.1</b> Experiments required to obtain gradient of objective function based on IFT technique. ....	89
<b>Table 5.2</b> Control parameters of each iteration with corresponding objective functions values. ....	93
<b>Table 6.1</b> Results of wavelet analysis on real errors of eight different conditions. No internal leakage was introduced into hydraulic actuator. ....	113
<b>Table 6.2</b> RMS values of level three wavelet approximation coefficient, $a_3$ , and fault-sensitive parameter, $\beta$ , corresponding to various levels of synthetic error. ....	115
<b>Table 6.3</b> FOPID controller parameters of seven faulty operating modes and those of base mode. Faulty mode means synthetic error was introduced to closed-loop system. ....	117
<b>Table B.1</b> Result of Routh-Hurwitz stability analysis considering $G_1(s)$ as plant transfer function. ....	143
<b>Table B.2</b> Result of Routh-Hurwitz stability analysis considering $G_2(s)$ as plant transfer function. ....	144

## LIST OF NOMENCLATURES

$\lambda$	Fractional order of integrator
$\mu$	Fractional order of differentiator
$s^\alpha$	Fractional-order operator in Laplace domain
$P_1$	Chamber 1 pressure signal ( $Pa$ )
$P_2$	Chamber 2 pressure signal ( $Pa$ )
$Q_1$	Flow rate between chamber 1 and servovalve ( $m^3/sec$ )
$Q_2$	Flow rate between chamber 2 and servovalve ( $m^3/sec$ )
$Q_i$	Internal leakage flow between two chambers of cylinder ( $m^3/sec$ )
$K_i$	Internal leakage coefficient ( $m^3/sec/\sqrt{Pa}$ )
$\beta$	Fluid bulk modulus ( $Pa$ )
$V_{pipe}$	Volume of each of two connecting pipes ( $m^3$ )
$V_0$	Volume of each chamber when the piston is centered ( $m^3$ )
$A$	Annulus area of the piston ( $m^2$ )
$m_p$	Mass of piston ( $kg$ )
$x_p$	Piston displacement ( $m$ )
$v_p$	Piston Velocity ( $m/sec$ )
$u$	Control signal ( $V$ )
$K_m$	Servomotor gain ( $rad/V.sec$ )
$F_{ext}$	External force ( $N$ )
$K_{ext}$	Spring stiffness ( $N/m$ )
$F_f$	Friction force ( $N$ )
$x_v$	Position of servovalve spool ( $m$ )
$v_v$	Velocity of servovalve spool ( $m/sec$ )
$\omega_v$	Servovalve natural frequency ( $rad/sec$ )
$\xi$	Servovalve damping ratio
$w$	Servovalve area gradient ( $m$ )
$k_v$	Position gain of servovalve spool ( $m/V$ )
$K_v$	Servovalve flow gain ( $m^{3/2}/\sqrt{kg}$ )
$P_r$	Return pressure ( $Pa$ )
$P_s$	Supply pressure ( $Pa$ )
$\tau$	Time delay or lag ( $sec$ or $sample$ )
$\mu_{P_1}$	Mean value of pressure data ( $Pa$ )
$f_c$	Cut-off frequency ( $Hz$ or $Sample/sec$ )
$f_h$	Highest frequency component ( $Hz$ or $Sample/sec$ )

$f_s$	Sampling frequency ( <i>Hz</i> or <i>Sample/sec</i> )
$D_E$	Euclidean dimension
$D_T$	Topological dimension
$\delta_{var}$	Percentage of change of variance
$\delta_{mean}$	Percentage of change of mean
$N_{min}$	Minimum number of data points
$D_c$	Correlation fractal dimension
$D_{HM}$	Box-counting fractal dimension
$N_r$	Number of volume elements covering the time series
$r$	Size of each volume element
$I(\tau)$	Mutual information index as function of lag
$x(n)$	Value of $n^{\text{th}}$ sample of signal
$P_i$	Probability that the time series $x(n)$ is located in bin $i$
$P_{ij}$	Probability that $x(n)$ is in bin $i$ and $x(n + \tau)$ is in bin $j$
$M$	Number of reconstructed points
$m$	Embedding dimension
$N$	Total number of data points
$X_i$	$i^{\text{th}}$ reconstructed point
$E_1(m)$	Cao's index as a function of embedding dimension
$C(r)$	Correlation sum
$r_{ij}$	Spatial separation between two points labeled $i$ and $j$
$\Theta(\cdot)$	Heaviside function
$H$	Hurst exponent
$D_\sigma$	Variance fractal dimension
$\lambda_1$	Largest Lyapunov exponent
$K_2$	Correlation entropy
$\psi$	Mother wavelet function
$\varphi$	Wavelet scaling function
$h[n]$	Wavelet low-pass filter coefficient
$g[n]$	Wavelet high-pass filter coefficient
$a_i$	Approximation coefficient of $i^{\text{th}}$ level of decomposition
$d_i$	Detailed coefficient of $i^{\text{th}}$ level of decomposition
$D^\alpha$	Fractional derivative of order $\alpha$
$J^\alpha$	Fractional integral of order $\alpha$
$\Gamma(\cdot)$	Gamma function
$E_\alpha(\cdot)$	Mittag-Leffler function
$\omega_u$	Unit frequency gain used in Oustaloup method ( <i>rad/sec</i> )
$\omega_b$	Low transitional frequency ( <i>rad/sec</i> )
$\omega_h$	High transitional frequency ( <i>rad/sec</i> )
$D(s)$	Transmittance
$K_P$	Proportional gain
$K_I$	Integral gain
$K_D$	Derivative gain
$\vec{p}$	Vector of control parameters
$J_P$	Performance index of objective function

---

$J_R$	Robustness index of objective function
$\alpha_y$	Tracking weighting index
$\alpha_u$	Control weighting index
$\alpha_s$	Robust stability weighting index
$\gamma_i$	Step size of each iteration used in IFT algorithm
$R_i$	Positive definite matrix used in IFT algorithm
$x_{p,ref}$	Reference displacement input of main actuator
$x_{p,act}$	Actual displacement of main actuator
$F_{ext,ref}$	Reference force of load actuator
$F_{ext,act}$	Actual force of load actuator
$e_c$	Controller input defined for FTC design ( $m$ )
$e_{syn}$	Synthetic error defined for FTC design ( $m$ )
$e_r$	Real error defined for FTC design ( $m$ )
$y$	System output defined for controller design ( $m$ )
$r$	Reference input defined for controller design ( $m$ )
$\beta^j$	Fault-sensitive parameter corresponding to $j^{th}$ operating mode
$T_U(s)$	Transfer function of upper bound used in prefilter design
$T_L(s)$	Transfer function of lower bound used in prefilter design

## LIST OF ACRONYMS

PID	Proportional-integral-derivative
FOPID	Fractional-order PID
IOPID	Integer-order PID
FTC	Fault-tolerant control
RMS	Root mean square
QFT	Quantitative feedback theory
IFT	Iterative feedback tuning
FOC	Fractional-order control
IOI	Integer-order integral
PF	Prefilter
FFT	Fast Fourier transform
AC	Autocorrelation
PSD	Power spectral density
LS	Least Squares
KS	Kolmogorov-Sinai
WT	Wavelet transform
DWT	Discrete wavelet transform
MSD	Multiresolution signal decomposition
QMF	Quadrature mirror filter
LPF	Low-pass filter
HPF	High-pass filter
NL	No leakage
SL	Small leakage
ML	Medium leakage
LL	Large leakage
RL	Riemann-Liouville

# CHAPTER 1

## INTRODUCTION

Engineering problems often require practical solutions which are of interest to industries. Practical solutions mean the solutions that lead to cost-effective and realizable results. One of the main problems that exists in industrial machinery is occurrence of faults. Fault refers to any phenomenon that may impair the system functionality. One solution to overcome the issues originating from the faults is design of controllers that are capable of compensating for effects of the faults. This thesis addresses one of the commonly-faced faults in the hydraulic actuation systems, namely the actuator internal leakage, and detect it followed by proposing a methodology for designing a fault-tolerant position controller.

### **1.1. Motivation**

Previous research studies, in fluid power systems, have mostly focused on the fault detection and design of controllers based on a system model and/or values of the system parameters. In real applications, finding models to describe behavior of the hydraulic actuators accurately is difficult. Moreover, values of the system parameters vary over time. Since the hydraulic actuators undergo

various parametric and non-parametric uncertainties, the use of model-free and data-driven techniques, for the analysis and control purposes, could be more attractive than the model-based ones. Therefore, fault-detection and development of a methodology for designing fault-tolerant controllers (FTCs) without relying on a prior knowledge about the model and parameters of the hydraulic actuators motivated the research undertaken in this thesis.

## 1.2. Problem Statement

Hydraulic actuators are used extensively in various industrial applications such as aircrafts [1], [2] and robots [3]-[6]. Two main features of the hydraulic systems are: (i) high incompressibility property of the fluid, which allows the pressure to be transmitted to any element attached to the actuator, and creates high speed motion with low shock compared to the pneumatic systems, as well as (ii) high power-to-weight ratio property, which leads to the generation of high forces with low inertia compared to other power generation devices such as electric motors. However, there exist issues associated with the hydraulic actuators: (i) existence of structured and unstructured uncertainties, and (ii) occurrence of faults [7], [8]. To avoid the actuator malfunctioning, there is a need for the fault detection and fault-tolerant control of the hydraulic systems.

### 1.2.1. Problem Definition

Faults in the hydraulic systems include actuator internal leakage, external leakage, change in the values of fluid bulk modulus and the supply pressure. The system functionality is impaired by the faults if they are not detected properly and their effects are not compensated [8], [9]. For instance, the internal leakage occurs between the chambers of the cylinder and causes the flow to

move between the two chambers. Detection of the internal leakage is difficult without dismantling the cylinder and piston [8]; thus, the actuator internal leakage is preferred to be detected by analyzing the system performance using advanced diagnostic methods [8], [10]. With respect to the fault detection in hydraulic actuators, most of the previous studies have been conducted using a system model and/or estimation of the system parameters.

On the control front, there is a need for design of controllers, which are both robust to the system uncertainties and tolerant to the faults. Most of the robust controllers, developed in this field, are model-based. Some efforts have also been done for designing fault-tolerant controllers in the hydraulic actuators. However, they all require a prior knowledge about the faults (*e.g.*, flow rate of the internal leakage or the leakage orifice area). In practice, faults may not be quantified. With respect to the internal leakage, for example, there is no instrumentation to measure the flow rate of the internal leakage in real applications. In this thesis, some solutions to solve the above problems are proposed. Specifically, the following problems are investigated:

- (i) The occurrence of some faults, *e.g.*, the actuator internal leakage, deteriorates the system performance. There is a need for the fault detection and fault-tolerant control of hydraulic actuators.
- (ii) There exist parametric and non-parametric uncertainties which affect the system performance if the controller is not robust enough.
- (iii) Model-based techniques of the fault detection and fault-tolerant controller design may not be attractive to certain industrial applications as there always exist some un-modeled dynamics and variations in the values of system parameters over time.

### 1.2.2. Proposed Solutions

The use of signal processing-based techniques may be a good solution for the fault detection as they can overcome the challenges associated with obtaining the dynamic models or estimating the system parameters [11]. Using data-driven fault detection techniques, experimental data could directly be utilized for extracting useful information about the system and faults once they occur [12].

There are various types of analyses based on experimental data. The signal processing-based fault detection studies have been performed mostly using single-scale techniques such as the Fourier transform, low-order and higher-order statistical analyses [10], [11]. Single-scale techniques are adequate for single-scale patterns or processes; however, many outputs from the dynamic systems are not single-scale [13], as they are independent of scale over many orders of magnitude. Such objects are called scale-free, *e.g.*, fractals [12]. In a fractal pattern, the single-scale analysis results in extracting incomplete information about the pattern. Since the pressure signals of the hydraulic actuators reveal the fractality property, the single-scale analysis is inadequate for some feature extractions such as the internal leakage detection. Hence, the application of multiscale approaches to the analysis of multiscale processes should be investigated as a possibly better solution for the fault detection [12].

Since signal processing-based techniques of fault detection are of concern, it is important to conduct a set of essential tests when dealing with experimental data. Essential tests must be performed regardless of the type of analysis (either single-scale or multiscale analysis). Two important tests are: (i) stationarity test, and (ii) sampling test. Stationarity is a quality of a process whose statistical moments do not vary over time. Sampling is a process of converting a continuous-time signal to a discrete-time signal. Improper sampling may discredit further analyses as it results

in loss of information about the signal. Therefore, the essential tests must be performed before analyzing experimental data using signal processing-based techniques.

With respect to design of fault-tolerant controllers for the hydraulic actuators, there is a need for development of a methodology which does not rely on a model and/or system parameters. To accomplish this goal, data-driven techniques of the controller design are proposed in combination with the introduction of a set of synthetic errors into the hydraulic actuators. Synthetic errors are proposed to emulate the fault effects on the system response without the need for modeling the fault or reproducing it during experiments.

### 1.3. Thesis Formulation

#### 1.3.1. Thesis Statement

This thesis aims to develop an experiment-based methodology for designing fault-tolerant position controllers in hydraulic actuators. The methodology employs *fractional-order PID* (FOPID) schemes as the controller structure, and the *iterative feedback tuning* (IFT) technique for the controller parameter tuning. Moreover, the actuator internal leakage is detected using multiscale analysis of experimental data, and the results are used for design of the fault-tolerant controller.

#### 1.3.2. Thesis Objectives

The objectives of the thesis are:

- (i) to investigate the efficacy of signal processing-based techniques and multiscale analysis of experimental data in diagnosis of the actuator internal leakage,

- (ii) to present properties of the FOPID schemes by introducing some concepts from the Fractional Calculus,
- (iii) to design an FOPID position controller using a data-driven controller parameters tuning technique, and
- (iv) to develop a practical methodology for designing fault-tolerant position controllers without using the system and fault models or emulating a fault in experiments. To achieve this objective, results of the items (i) and (iii) are employed.

### 1.3.3. Research Questions

In order to meet the above objectives, the following research questions will be answered:

- (i) What are the concepts of stationarity and proper sampling in analyzing experimental data taken from a hydraulic actuation system?
- (ii) What are the requirements of conducting a multiscale analysis on experimental data, and how to detect a fault using multiscale measures?
- (iii) How are the FOPID control schemes employed to design a position controller using experimental data only?
- (iv) How to design a fault-tolerant controller without introducing the fault into the experimental setup, and without having a prior knowledge about the fault model and parameters?

### 1.3.4. Methods and Techniques

There are various methods to diagnose faults, and control the piston position of the hydraulic actuators. In this thesis, a set of multiscale measures is employed for the fault detection. Moreover,

fractional-order PID schemes are used to design a robust and fault-tolerant controller. This research is built upon two studies conducted previously [14], [15].

First, the actuator internal leakage is detected by performing some signal processing-based and multiscale analyses on experimental data taken from an instrumented hydraulic actuation system in various healthy and faulty operating modes. The multiscale measures, used for the fault detection, consist of *the correlation fractal dimension, variance fractal dimension, maximal Lyapunov exponent, correlation entropy* (close lower bound on Kolmogorov-Sinai entropy) and *wavelet coefficients* [16], [17]. All analyses are applied to the chamber one pressure signal of the hydraulic actuator. Then, the most reliable multiscale measure is recognized in terms of the sensitivity to the various levels of the internal leakage. The chosen multiscale measure is then applied to the displacement error data of various operating modes, and the results are employed, for the verification purpose, when designing a fault-tolerant controller later.

From the controller design perspective, a data-driven technique called the *iterative feedback tuning* is used to tune the FOPID parameters. Furthermore, fractional-order operators that exist in the FOPID structure are realized by employing the *Oustaloup recursive technique*. The robustness of the controller against various types of the system uncertainties is examined through different experiments. The system uncertainties include external loads, frictions and inertia.

Finally, the robust FOPID scheme is employed as a base controller for designing a fault-tolerant position controller. Exemplified with designing an FTC for a valve-controlled hydraulic actuator experiencing the internal leakage, a set of errors is synthesized and introduced to the hydraulic actuator that is otherwise operating in the healthy mode. Healthy operating mode means that there is no fault in the system. Synthetic errors are used to emulate the internal leakage effect on the system response. The multiscale technique, chosen in first part of this thesis, is employed

to conduct a sensitivity analysis for investigating effect of the synthetic errors on the displacement error signal. Note that the synthetic error is different from the displacement error that is defined as the difference between the reference input and actual displacement taken from a position encoder. Based on the results of the sensitivity analysis, a *fault-sensitive parameter* is defined which is further used in the controller design procedure for faulty operating modes. Overall, an FOPID-based FTC is developed whose design procedure is completely data-driven and does not require any information about the fault (*i.e.*, the flow rate of the internal leakage or the leakage orifice area).

#### **1.4. Thesis Organization**

Chapter 2 presents a literature review on various techniques used for the fault detection in hydraulic actuators as well as methods for the controller design, parameters tuning and the realization of fractional-order operators. In Chapter 3, the experimental setup and electromechanical components are explained. In addition, mathematical modelling of the hydraulic actuators is presented. Chapter 4 describes procedure of the internal leakage detection using multiscale analysis of experimental data. Details on the sampling, stationarity and fractality tests are presented followed by explaining a set of preliminary procedures required for the multiscale analysis. Various multiscale measures, used for the internal leakage detection, along with the implementation results are presented. Chapter 5 provides details on definitions of the fractional-order operators and their geometrical and physical meanings. The techniques of realizing fractional-order operators and tuning the controller parameters are also described. The controller design procedure is then presented and experimental results are illustrated to show the robustness of the proposed FOPID controller against system uncertainties. In Chapter 6, the entire procedure

of designing a fault-tolerant position controller, based on the results obtained from Chapters 4 and 5, is described. Experimental validations are presented to show the efficacy of the proposed methodology in designing an FTC for a hydraulic actuation system experiencing the internal leakage. Chapter 7 outlines the contributions of this thesis as well as the conclusions and possible extensions of this work.

## CHAPTER 2

# RELEVANT BACKGROUND

Fault detection and fault-tolerant controller design in hydraulic actuators require extensive knowledge on various techniques and design methods. With respect to the fault detection, previous studies have been carried out using both model-based and signal processing-based techniques – the latter being mostly dealt with the single-scale analysis of experimental data. On the controller design front, various methods have been employed each having their own pros and cons. This chapter provides a literature review on previous studies devoted to the fault detection and controller design in the hydraulic actuation systems.

### **2.1. Fault Detection in Hydraulic Actuators**

Fault detection in hydraulic systems is important to prevent serious actuator malfunctioning. Faults, in hydraulic actuation systems, have been classified into various categories [18]. Amongst the faults addressed in [18], the actuator internal leakage is particularly important. It occurs due to wearing in the piston seal that separates the cylinder chambers. The internal leakage affects the actuation performance significantly as the flow moves between two chambers of the cylinder [8].

A comprehensive survey on techniques used for the fault detection in hydraulic actuators has been provided in [14]. To name a few, Tan and Sepehri [19] utilized the Volterra nonlinear model to detect actuator leakage faults. They reported a method that requires a model of leakage for the prediction. Le *et al.* [20] classified types and levels of the leakage in the hydraulic actuators by simulating the internal leakage levels using neural networks and dynamic feature extractions. Shi *et al.* [21] used a linearized model with an adaptive threshold to detect the internal leakage. In another study, Frank [22] employed nonlinear observers to detect faults in the hydraulic systems. Faults in the shaft speed sensor of a hydraulic pump was detected using a bilinear fault detection observer [23]. The feasibility of using the extended Kalman filter to detect incorrect supply pressure in a hydraulic system has been reported in [24]. Wang and Syrmos [25] employed multiple models to estimate the parameters needed to detect changes in the torque motor and the effective bulk modulus of a hydraulic actuation system. Afshari *et al.* [26] developed a dynamic second-order smooth variable structure filter and an interacting multiple model strategy for the fault detection in an electro-hydrostatic system. A scheme has been developed for the fault diagnosis using unscented Kalman filter in a hydraulic system [27]. The above model-based techniques require some information or estimation of the model parameters to detect faults properly. In practice, there is no accurate model to describe dynamics of some faults. For example, an accurate model for the actuator internal leakage has not been well-established [12].

Signal processing-based fault detection methods are quite attractive, for certain industrial applications, since they can overcome the challenges associated with obtaining dynamic models or estimating the system parameters [11]. Goharrizi and Sepehri [11], [28], [29] conducted a study on the internal and external leakage detections in a valve-controlled hydraulic system using the Fourier, wavelet and Hilbert-Huang transforms. They demonstrated that the Hilbert-Huang and

wavelet coefficients are more sensitive to the leakage as compared to the Fourier transform. From the computational time perspective, the wavelet transform was much more efficient than the Hilbert-Huang transform.

Most signal processing-based studies have been built upon single-scale techniques. Using a single-scale analysis, the measures are obtained considering a window of data whose size does not vary throughout the analysis. In a single-scale pattern or process, conducting an analysis on different sizes of data is not required as the results are almost the same for different sizes of data points. An example of the Fourier transform-based single-scale analysis is the work mentioned above [11]. In that study, the root mean square (RMS) value of the Fourier transform amplitude was used, over a certain feature frequency band, to detect the internal leakage; however, the Fourier transform did not show a promising sensitivity to various levels of the leakage. Single-scale techniques are adequate for the single-scale patterns or processes. Many outputs from dynamic systems are not single-scale [13], as they are independent of scale over many orders of magnitude. Such outputs are called scale-free (*e.g.*, self-similar or self-affine fractals). According to the definition, an object is a fractal if a portion of the whole is the scaled-down version of the whole [30]. Self-similar fractal is an object whose scaling is isotropic, *i.e.*, it has the same scale along different coordinates. Self-affine fractals, on the other hand, have different scales along different coordinates [30]. For a fractal pattern, a single-scale analysis results in extracting incomplete information about the pattern. Since the actuator pressure signal of the hydraulic actuator reveals the fractality property [12], a single-scale analysis is inadequate for some feature extractions such as the internal leakage detection. Multiscale techniques are better tools for analyzing fractal patterns because multiscale measures (*e.g.*, fractal dimensions [30]) are quantified considering different sizes of data.

With respect to the application to fault detection, the number of research work based on the multiscale analysis of experimental data is still limited. Li *et al.* [31] used the concept of multiscale permutation entropy to extract features of the roller bearing vibration signal in different scales followed by detecting the fault using an improved support vector machine-based binary tree. An approach was introduced based on the wavelet packet decomposition principal component analysis in order to carry out the laser welding process monitoring and the welded defect diagnosis [32]. Jiang *et al.* [33] employed a multiscale analysis to demodulate the fault features of the hydraulic pump fault signals based on the local mean decomposition and an improved adaptive multiscale morphology analysis. With respect to the internal leakage detection, there is a need to investigate the application of multiscale techniques to the analysis of multiscale patterns such as the pressure signals in hydraulic actuators.

## 2.2. Controller Design in Hydraulic Actuators

There are three main issues that make the problem of designing a controller challenging in the hydraulic actuators. The first one is nonlinearities associated with the hydraulic systems, *e.g.*, the flow rate of the fluid moving between the ports of servovalve and chambers of the cylinder. The second issue is the existence of structured and unstructured uncertainties such as the changes in system parameters over time. Some uncertainties, in hydraulic actuators, comprise the variation in the external load applied to the piston or the change in values of the inertia and friction. Third issue is the occurrence of faults. The functionality of hydraulic actuators is impaired if the controller is not tolerant to the faults.

Sekhavat *et al.* [34] designed a nonlinear Lyapunov controller to regulate the impact of a hydraulic actuator that comes in contact with a nonmoving environment. As the friction model and

the control law were discontinuous, the control system was non-smooth. Therefore, they investigated the existence, continuity, and uniqueness of the Filippov's solution to the system [34]. The feasibility of using the feedback linearization technique in designing a controller for a rotational hydraulic drive has been studied by Seo *et al.* [35]. Nakkarat and Kuntanapreeda [36] developed a nonlinear controller based on the backstepping approach to control the force applied to the piston of an electrohydraulic actuator. In their study, they used a PI observer to estimate some states of the system. Karpenko and Sepehri [7] employed the quantitative feedback theory (QFT) to design a robust position controller in the presence of certain uncertainties. Despite good results reported in [7], the procedure of the controller design requires one to obtain a family of the transfer functions describing the system. With respect to design of fault-tolerant controllers (FTCs) for hydraulic actuators, Niksefat and Sepehri [37], [38] designed a set of FTC schemes, based on the QFT, to compensate for effects of the sensor failure and the faults occurring in the servovalve and the supply pump. Karpenko and Sepehri [15], [39], [40] emulated the internal leakage in a valve-controlled hydraulic actuation setup, and designed QFT-based FTC schemes to retain the system performance in presence of the internal leakage. In that work, some information about either the flow rate of the internal leakage or leakage orifice area were required. Zhang and Jiang [41] employed a two-stage adaptive Kalman filter to estimate the states and fault parameters simultaneously and utilized an eigenstructure assignment technique to design a reconfigurable feedback controller based on the results obtained from the fault detection.

The above control schemes are model-based and rely on a knowledge about the model and parameters of the system or faults, which can be challenging for uncertain nonlinear hydraulic actuators. In practice, some faults may not be quantified. With respect to the internal leakage, for example, there is no instrumentation to measure the flow rate of the internal leakage. Data-driven

control schemes are desirable as they do not need a model of the hydraulic actuators.

One of the well-known control schemes is the family of integer-order proportional-integral-derivative (IOPID) controllers which are also known as conventional PID controllers. IOPID controllers are attractive to industry because they are simple to implement and can be tuned based on experimental data (*i.e.*, using data-driven tuning techniques) as well. Conventional PID controllers, however, are not robust enough to operate well under a wide range of system uncertainties [7].

Drawbacks of conventional PID schemes have been overcome to a large extent by the development of fractional-order PID (FOPID) controllers. There are two more tuning parameters in an FOPID scheme (which is shown as  $PI^\lambda D^\mu$ ) as compared to the conventional PID controllers.  $\lambda$  and  $\mu$  are orders of the integral and derivative parts, respectively. In fact,  $\lambda$  and  $\mu$  have been added to the conventional PID controllers to enhance performance of the controller and make the controller design more flexible [42]. Fractional-order differentiator and integrator have been used in the control of dynamic systems since 1990s [42]. Design of an FOPID controller entails understanding of basic concepts from the Fractional Calculus. Overall, there exist two main challenges in designing an FOPID controller:

- (i) In theory, the FOPID structure is an infinite dimensional linear filter, as the orders of integrator and differentiator are fractional [42]. Therefore, fractional-order operators should be realized by equivalent finite dimensional transfer functions. In the Fractional Calculus, many efforts have been done to obtain a realizable form for fractional-order operators [42]-[44]. To name a few, Oustaloup *et al.* [45] and Charref *et al.* [46] have introduced some techniques to approximate the continuous version of the fractional-order operators based on the curve fitting and identification approaches. Moreover, general

continued fraction expansion [47], Carlson's [48] and Matsuda's [49] techniques have been developed for this purpose. A comparison between the above-mentioned techniques has been carried out which shows a better performance of the Oustaloup's technique in realization of fractional-order operators [44].

- (ii) The second challenge is the controller parameters tuning. Most of the parameter tuning methods have been built upon a mathematical model of the system or require some information about the system parameters. For example, the iterative correlation-based tuning [50], virtual reference feedback tuning [51], tuning based on Haar wavelet operational matrix [52], Astrom-Haggland's method [53] and Shekher's method [54] are all model-based or need an estimation of parameters. The iterative feedback tuning (IFT) [55] is a data-driven technique which can tune the FOPID control parameters using the experimental data. In Chapter 5, more details about the IFT technique will be provided.

Recently, several studies have been carried out to design fractional-order controllers (FOCs) for various systems [56]-[61]. As far as hydraulic actuation systems are concerned, the number of studies on design of FOC schemes is still sparse. Ma *et al.* [62] combined a fractional-order controller with the traditional model reference adaptive theory to promote the performance of the hydraulic flight simulator. Jiangbo *et al.* [63] designed two FOPI and FOPID force controllers, for a composite hydraulic system, to generate alternating and fixed forces aiming at driving an insulator fatigue test device. In another study, they improved a fluid parameter slow-varying problem, in an electro-hydraulic system, using a fractional-order PI controller [64]. Gao *et al.* [65] developed two extended state observer-based FOPID controllers, for a novel electro-hydraulic servo system, to realize active balancing of the inherent gravitational torque and tracking control of a barrel. Rajasekhar *et al.* [66] designed an FOC using a micro artificial bee colony algorithm

to compensate for the leakage effects in a faulty actuator. Previously developed FOC-based position controllers for the hydraulic actuation systems are model-based.

### **2.3. Summary**

This chapter provided a literature review on the fault detection and controller design in hydraulic actuation systems. First, model-based and signal processing-based fault detection techniques were discussed followed by presenting a number of studies carried out using multiscale analysis of experimental data. On the controller design front, several research studies were reviewed each being built upon a system model or an estimation of system parameters. A brief description on fractional-order PID controllers as well as various techniques developed for the realization of fractional-order operators were presented followed by discussing model-based and data-driven techniques of controller parameters tuning. Based on the literature review, there is a lack of studies, in the hydraulic actuators, on fault detection using multiscale analysis of experimental data as well as design of fault-tolerant controllers based on data-driven tuning techniques and without relying on a fault model or fault parameters.

## CHAPTER 3

# EXPERIMENTAL SETUP

In this chapter, the experimental setup of a valve-controlled hydraulic actuation system is explained followed by presenting equations describing the hydraulic actuator. Although this study is based on the experimental data directly taken from the test rig, a mathematical model of the hydraulic system is provided to help readers understand the system dynamics.

### 3.1. Test Rig

The experimental setup and overall schematic of the valve-controlled hydraulic actuators are shown in Figure 3.1 and Figure 3.2, respectively. The system comprises a power unit with maximum supply pressure of 3000 *psi*. Several ball valves, needle valves, and relief valves as well as steel pipes constitute the connecting part. The actuating part includes a two-stage servovalve, three double-rod actuators and a combination of a spring and mass for interacting with environment. Two of the actuators play role of slave actuators and are used to increase the friction and inertia imposed on the main cylinder-piston. Moreover, the spring is replaced by a setup of loading actuator as shown in Figure 3.5.

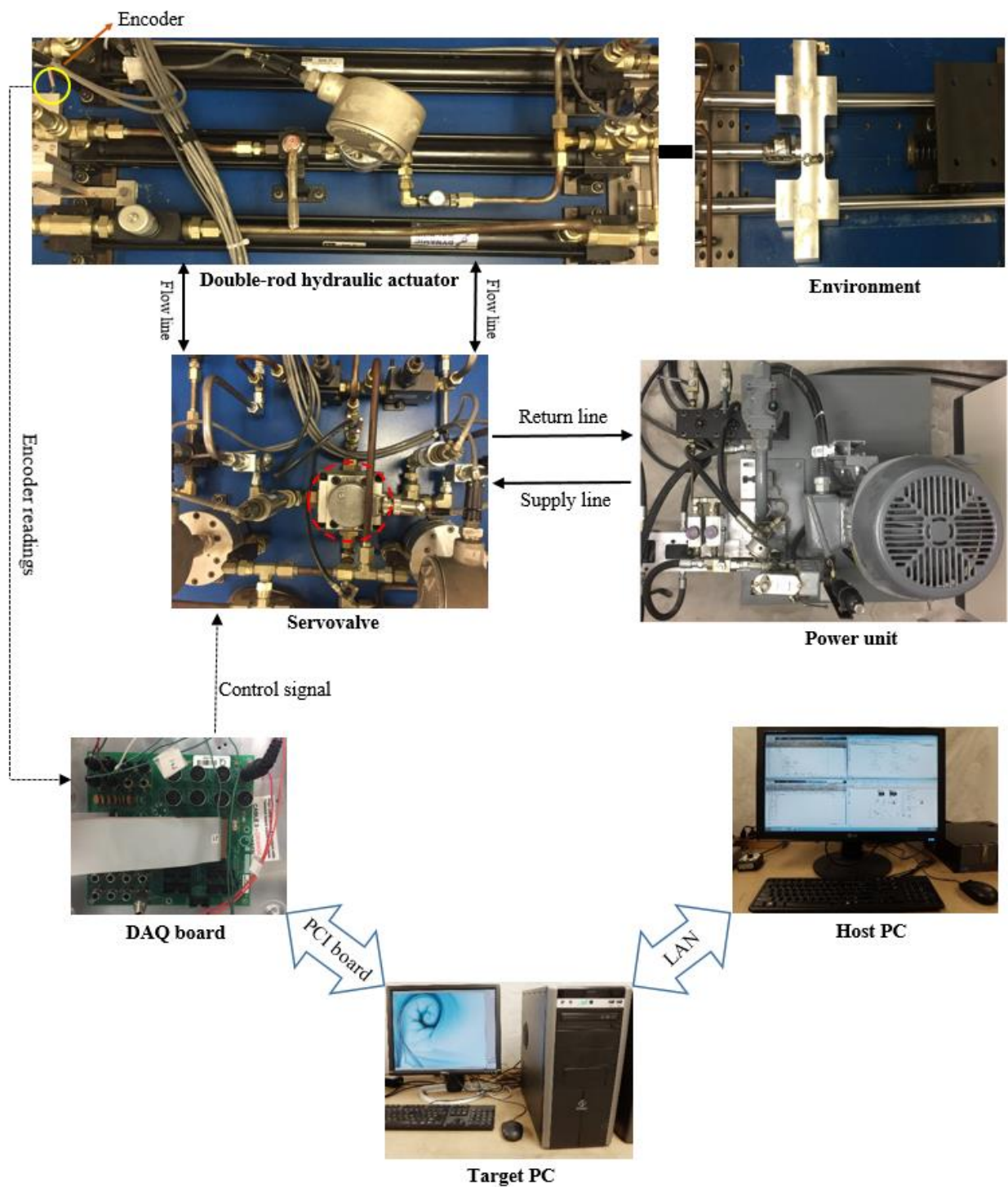


**Figure 3.1** Experimental setup of valve-controlled hydraulic actuator with data acquisition system.

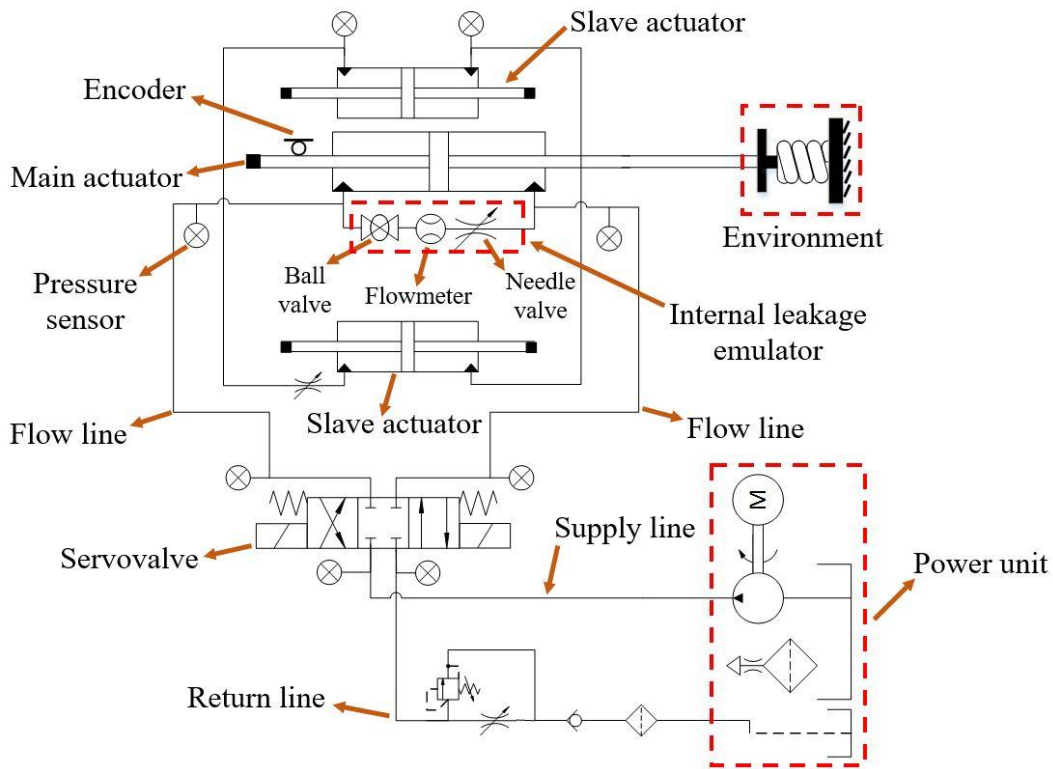


**Figure 3.2** Schematic of valve-controlled hydraulic actuator.

The data acquisition system of the valve-controlled hydraulic actuator consists of a host PC, a target PC and a Quanser<sup>®</sup> Q8 data acquisition board that includes eight I/O analog ports, eight encoders and 32 digital I/O within a PCI card. Readings of sensory system are sent to the host PC through a PCI board and the target PC. The host PC is utilized for implementing the controller. Thus, the control input is generated in the host PC, and is then sent to the servovalve via the analog output of the Q8 board mounted on the target PC. All sensors and the servovalve command input are also connected to the Q8 board and the target PC. The target PC operates under the QNX Operating System (QNX-OS). One of the main features of the QNX-OS is its special architecture, which consists of a real-time microkernel surrounded by a collection of resource managers [67]. This architecture allows each process to run in its own virtual memory space. The advantage of

using the virtual memory is that one process cannot interrupt another process memory space [67]. This feature prevents the occurrence of the delay in sending/ receiving data to/ from an experimental setup.

Details of the components that create the internal leakage are shown in Figure 3.3. They are employed to emulate various levels of the leakage between two chambers of the cylinder. The leakage emulator includes a ball valve, a needle valve and a flowmeter. The needle valve is responsible for producing different levels of the internal leakage. The available flowmeter measures flow rate of the leakage during the experiments.

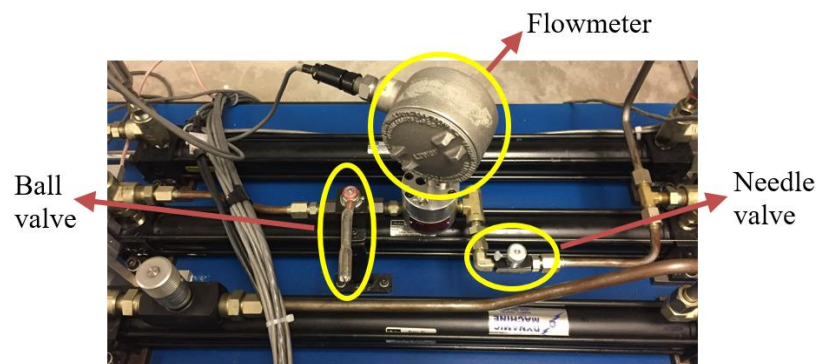


**Figure 3.3** Setup of internal leakage emulator comprising ball valve, needle valve and flowmeter. Needle valve is used to change level of leakage. Flowmeter measures flow rate of internal leakage between two chambers.

To design a robust position controller, data of the position encoder is used. With respect to the available hydraulic actuator, the piston mass, the external load, and the friction force are usually considered as uncertainties in the hydraulic system [68]. Therefore, a set of extra masses, various springs and extra actuators are employed to verify the efficacy of the designed position controller

in terms of the robustness to changes in the values of inertia, external load and friction. To achieve this goal, two slave actuators and extra masses are added to the main actuator as shown in Figure 3.4. Various experiments are conducted using combinations of (i) three different springs ( $K_{ext} = 45, 80 \text{ and } 160 \text{ kN/m}$ ) emulating the external loads, (ii) two extra masses resembling the uncertainties that may happen in the mass of the implement over time, and (iii) two slave actuators showing the effect of change in the friction and inertia.

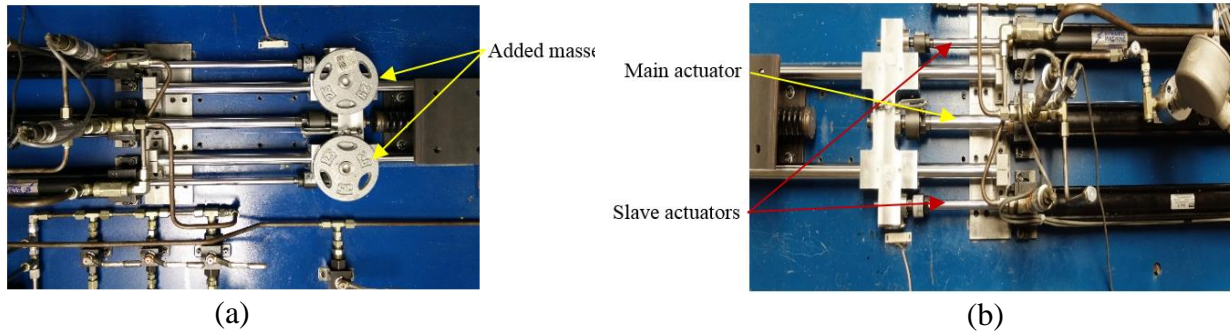


**Figure 3.4** (a) Extra masses added to main actuator in order to investigate effect of change in inertia on performance of controller; (b) slave actuators are connected in parallel to main actuator to emulate changes in friction as well as inertia.

In order to investigate the performance of the position controller under controlled external loads, a loading actuation system is employed. Figure 3.5 shows the experimental setup designed for this purpose. A loading actuator is run by a servovalve which itself is controlled by a proportional force controller. A load cell sensor is required to measure the actual force applied to the main actuator. Moreover, a flexible coupling is used, between the loading and main actuators, to reduce the stiffness of the joint between them [15].

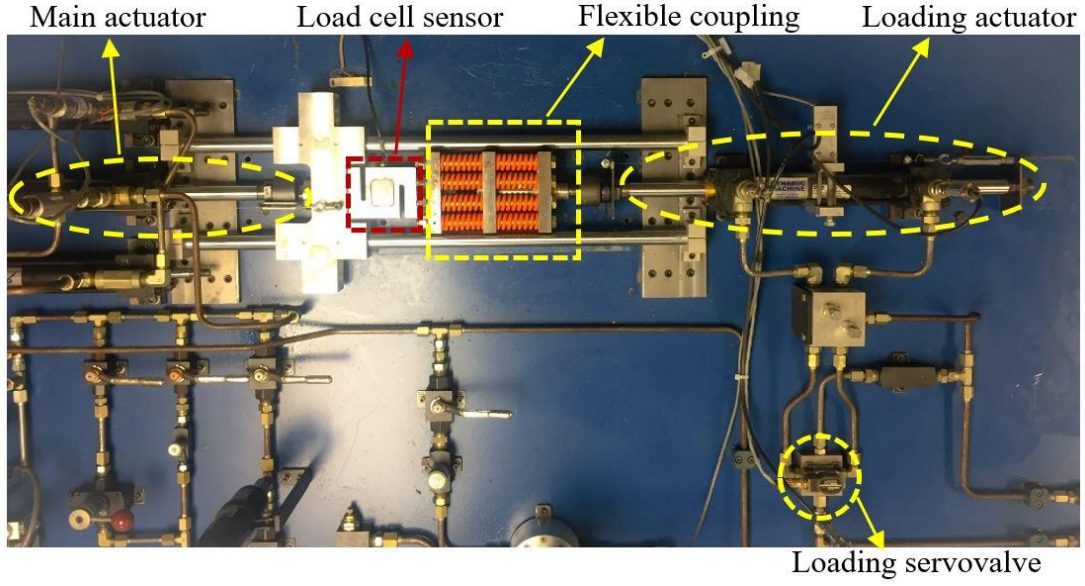


**Figure 3.5** Setup of loading actuation system used to apply controlled force to main actuator.

### 3.2. Mathematical Model

The dynamics of the hydraulic actuation system are expressed by the following equations:

$$\dot{x}_p = v_p \quad (3.1)$$

$$\dot{v}_p = \frac{1}{m_p} (AP_1 - AP_2 - F_f - F_{ext}) \quad (3.2)$$

$$\dot{x}_v = v_v \quad (3.3)$$

$$\dot{v}_v = -\omega_v^2 x_v - 2\xi\omega_v v_v + k_v \omega_v^2 u \quad (3.4)$$

$$\dot{P}_1 = \frac{\beta}{V_0 + V_{pipe} + Ax_p} (Q_1 - Av_p - Q_i) \quad (3.5)$$

$$\dot{P}_2 = \frac{\beta}{V_0 + V_{pipe} - Ax_p} (-Q_2 + Av_p + Q_i) \quad (3.6)$$

$$Q_1 = K_v w x_v \sqrt{\frac{P_s - P_r}{2} + \text{sgn}(x_v) \left( \frac{P_s + P_r}{2} - P_1 \right)} \quad (3.7)$$

$$Q_2 = K_v w x_v \sqrt{\frac{P_s - P_r}{2} + \text{sgn}(x_v)(P_2 - \frac{P_s + P_r}{2})} \quad (3.8)$$

$$Q_i = K_i \text{sgn}(P_1 - P_2) \sqrt{|P_1 - P_2|} \quad (3.9)$$

where  $x_p$  and  $v_p$  are the piston displacement and velocity, respectively;  $P_1$  and  $P_2$  denote hydraulic pressures in chambers “one” and “two” of the actuator, respectively;  $m_p$  is the moving mass and  $A$  represents the annulus area of the piston;  $F_{ext}$  and  $F_f$  refers to the external force and friction force applied to the piston, respectively;  $x_v$  and  $v_v$  are the position and the velocity of the servovalve spool, respectively;  $k_v$  denotes the spool position gain;  $\omega_v$  and  $\xi$  are the servovalve natural frequency and damping ratio;  $u$  is the control signal given to the servovalve;  $Q_1$  and  $Q_2$  represent the flow rates between the servovalve ports and cylinder chambers;  $V_0$  is the volume of each chamber when the piston is centered and  $V_{pipe}$  refers to the volume of each of two connecting pipes;  $\beta$  is the effective bulk modulus of the fluid and  $K_v$  is the servovalve flow gain while  $w$  represents the servovalve area gradient;  $P_s$  and  $P_r$  are the supply and return pressures, respectively;  $Q_i$  refers to the internal leakage flow rate between two chambers of cylinder while  $K_i$  is the internal leakage coefficient;  $\text{sgn}(\ast)$  denoted the sign function. According to Eqs. (3.1) to (3.9), the valve-controlled hydraulic actuation system is composed of six state variables as follows

$$\vec{x} = [x_1, x_2, x_3, x_4, x_5, x_6]^T = [x_p, v_p, P_1, P_2, x_v, v_v]^T \quad (3.10)$$

The number of state variables is mentioned here to prove the efficacy of a technique used in Chapter 4 in order to determine the minimum embedding dimension (see Section 4.2.2.3).

## CHAPTER 4

# ACTUATOR INTERNAL LEAKAGE DETECTION<sup>1</sup>

This chapter focuses on the actuator internal leakage detection using multiscale analysis of experimental data. Multiscale techniques are strong tools in analysis of time series because they are able to extract more useful information about the systems as compared to the single-scale approaches. Multiscale measures, used in this thesis, consist of the correlation fractal dimension, the variance fractal dimension, maximal Lyapunov exponent, the correlation entropy and the wavelet coefficients [16], [17]. There exist many measures potentially suitable for the fault detection. In this thesis, only five measures have been chosen that are distinct and cover a wide range of concepts related to the information extracted from a self-affine time series. By quantifying the multiscale measures in different operating modes, a set of comparisons is performed to identify the most sensitive indicator(s) in detecting various levels of the actuator internal leakage.

Before obtaining the multiscale measures of pressure data in various operating modes, some fundamental tests are carried out to ensure the pressure data are stationary and sampled properly.

---

1. The content of this chapter is partially published in *IEEE Trans. on Instrumentation and Measurement*, Dec. 2016.

Moreover, a fractality test is conducted to see whether the pressure signal could be considered as a fractal object. One special test so-called “*Tsonis criterion test*” is also conducted to ensure the number of sampled data is enough for further analyses. Figure 4.1 shows the main steps followed to quantify the multiscale measures of the pressure signal for the internal leakage detection.

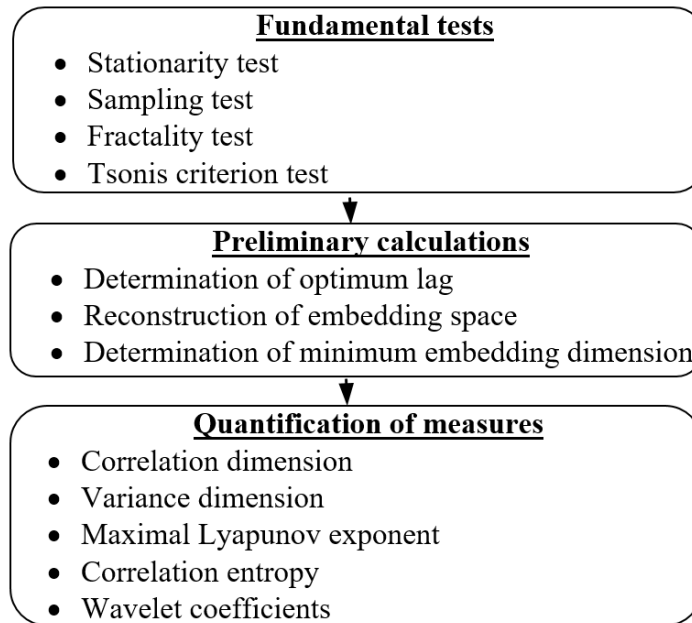


**Figure 4.1** Steps followed to quantify multiscale measures.

#### 4.1. Data Collection

Experimental measurements of the chamber one pressure signal ( $P_1$ ) are collected and employed as the data required for the internal leakage detection. The signal is achieved from a feedback control system in all healthy and faulty operating modes. Since the focus of this chapter is on the internal leakage detection, no controller has been designed for this part of the study, and a previously-developed QFT control scheme is used. The controller structure ( $C_{QFT}$ ) and prefilter ( $PF$ ), presented in [7], are as follows

$$C_{QFT}(s) = \frac{3.21 \times 10^7 (s + 4.7)(s + 42)}{s(s + 29)(s^2 + 225s + 250^2)} \quad (4.1)$$

$$PF(s) = \frac{23(s + 13)}{(s + 7.5)(s + 40)} \quad (4.2)$$

Note that the values of zeros and poles used in the QFT controller and prefilter structures have been obtained from a loop-shaping procedure such that a set of tracking and robust stability criteria has been met. Details of the QFT controller design are provided in [7]. First, this control system is employed in the healthy operating mode and typical experimental data are collected as shown in Figure 4.2. The signals are measured for 10 sec; however, they are shown over the interval of [2, 5] sec for the sake of clarity. The position controller causes the actuator to follow the step input of 5 mm with very small variations. It is noted that the needle valve, responsible for creating the internal leakage between two chambers, is completely closed; however, the flowmeter shows a very small internal leakage which is due to the measurement noise. This mode of experiment is considered as the healthy operating mode.

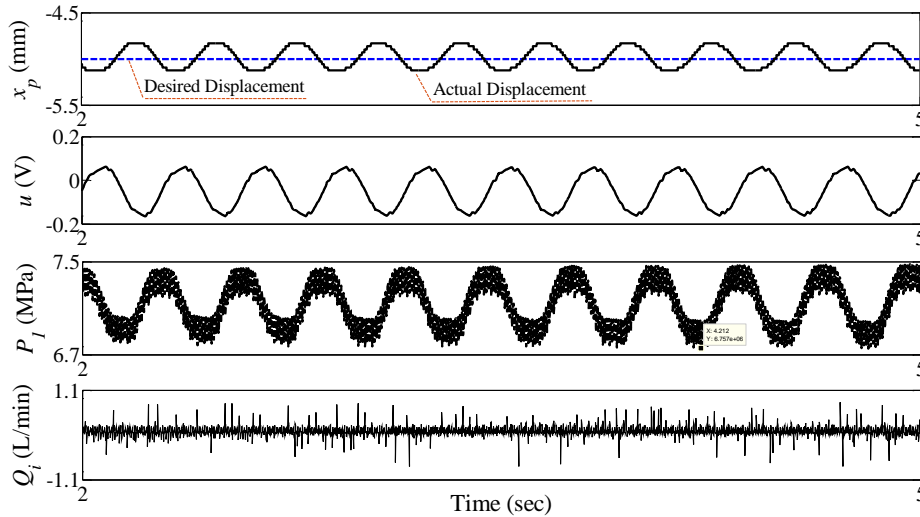


**Figure 4.2** Typical signals taken from an experiment in healthy operating mode ( $\bar{Q}_i = 0.09 \text{ L/min}$ ).

By employing the control scheme (4.1) and the prefilter (4.2) in three faulty operating modes, experimental data of the pressure signal ( $P_1$ ) were recorded. Figure 4.3 illustrates three levels of the internal leakage and their corresponding chamber one pressure data. The flow rate of the internal leakage increases by opening the needle valve of the leakage emulator. The first level of the internal leakage is small leakage with the flow rate of  $0.22 \text{ L/min}$  in average (*i.e.*,  $\bar{Q}_l = 0.22 \text{ L/min}$ ). The corresponding values for the medium and large internal leakages are  $0.65 \text{ L/min}$  and  $1.19 \text{ L/min}$ , respectively.

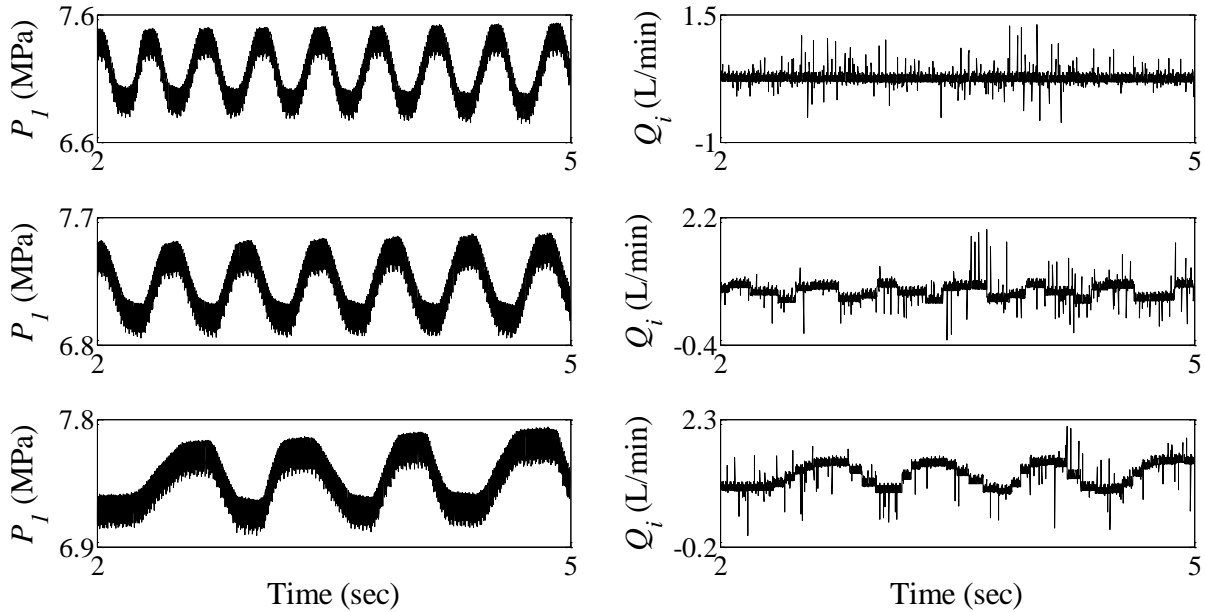


**Figure 4.3** Pressure data ( $P_1$ ) and corresponding internal leakage flow rates ( $Q_i$ ) taken from experimental setup in three levels of leakage: (a) small leakage ( $\bar{Q}_l = 0.22 \text{ L/min}$ ), (b) medium leakage ( $\bar{Q}_l = 0.65 \text{ L/min}$ ), and (c) large leakage ( $\bar{Q}_l = 1.19 \text{ L/min}$ ).

## 4.2. Analysis Procedure

As illustrated in Figure 4.1, three main steps are followed for the analysis of the pressure data: fundamental tests, preliminary calculations, and quantification of measures. To clarify the application of each step to the multiscale analysis of experimental data, details are provided in this section followed by presenting the analysis results obtained from the pressure signal of an experiment in the healthy operating mode (*i.e.*, the signal  $P_1$  shown in Figure 4.2).

### 4.2.1. Fundamental Tests

It is important to ensure about the proper sampling as well as the stationarity and fractality properties of experimental data before analyzing a signal using multiscale techniques.

#### 4.2.1.1. Stationarity Test

Stationarity is a quality of a process whose statistical moments do not vary over time [10]. Investigation of the stationarity of a signal is essential especially when there is a need for using the fast Fourier transform (FFT). If the experimental data are non-stationary, the signal has to be segmented into short-time windows within which the signal is stationary. In other words, one can use the short-time Fourier transform for a non-stationary signal [12]. There are two main definitions, between many interpretations, for the stationarity: (i) strong stationarity, and (ii) weak stationarity. Strong stationarity means that all statistical moments of a signal (*i.e.*, mean, variance, skewness, kurtosis and *etc.*) do not change as time evolves. In real applications, it is difficult to find a strong stationary signal. Therefore, the weak stationarity requirements are usually investigated for the stationarity test. According to [69], a time series is weakly stationary if its

mean and autocorrelation hold constant over time. The mean value of a set of experimental data is calculated as follows

$$\bar{x} = \frac{1}{N} \sum_{n=1}^N x_n \quad (4.3)$$

where  $\bar{x}$  is the mean value, and  $\{x_n\}$  ( $n = 1, 2, \dots, N$ ) represents each data point; also,  $N$  is the total number of data points. The autocorrelation function of a time series is the Fourier transform of its power spectrum in the time domain, and is expressed by [13]

$$AC(\tau) \cong \frac{\sum_{n=1}^{N-\tau} (x_n - \bar{x})(x_{n+\tau} - \bar{x})}{\sum_{n=1}^{N-\tau} (x_n - \bar{x})^2} \quad (4.4)$$

where,  $AC$  and  $\tau$  are the autocorrelation function and the time delay (lag) between the data points, respectively. The autocorrelation and the mean of the pressure signal ( $P_1$ ) of the healthy operating mode are obtained to find out if this signal is weakly stationary. The first 2000 data points of  $P_1$  were omitted because they pertain to the transient behavior of the hydraulic actuator. To achieve reliable results for the stationarity test, data interval [2001, 10000] (equivalent to the time interval [2, 10] sec) was considered. Results were obtained under sliding window size of 1000 samples, step size of 50 (5% of window size) and lag of 1. The chosen window size, step size and lag was obtained by trial and error and revealed best results in proving the stationarity of the experimental data. Figure 4.4 shows the variations of the autocorrelation coefficient and the mean over the time between 2 and 10 sec. With respect to Figure 4.4, both the autocorrelation coefficient and the mean did not change significantly when time evolves. The difference between the maximum and minimum values of the mean ( $\mu_{P_1}$ ) was around 6% of the corresponding value in the original signal  $P_1$ . Therefore, the pressure signal could be assumed as a weakly stationary signal.

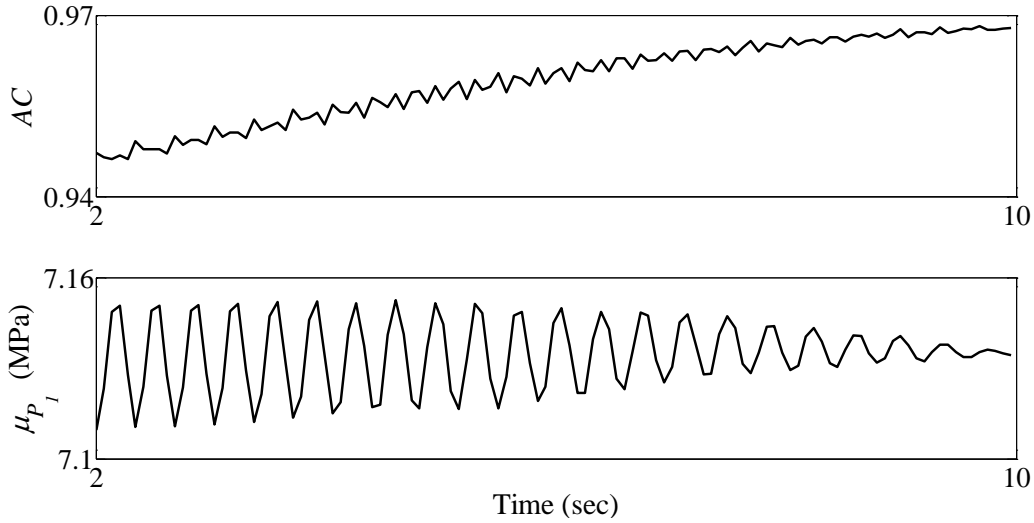


**Figure 4.4** Autocorrelation ( $AC$ ) and mean of signal  $P_1$  ( $\mu_{P_1}$ ) at sliding window size of 1000 samples, step size of 50 and lag of 1. Time interval of  $[2, 10]$  sec is equivalent to samples of  $[2001, 10000]$ .

#### 4.2.1.2. Sampling Test

Sampling is the process of converting a continuous-time signal into a discrete-time signal. Improper sampling results in the aliasing phenomenon. Aliasing means that replicas of a signal spectrum within the Fourier transform overlap, and part of the information content from the input signal is lost [69]. To avoid aliasing, the sampling rate should be well above the Nyquist rate [69]. In this study, the data were sampled at a rate of 1000 *Samples/sec* (*Sps*) using the Quanser<sup>®</sup> data acquisition system. Sampling must be performed based on the Nyquist-Shannon sampling theorem. According to this theorem, the sampling frequency ( $f_s$ ) should be at least twice the highest/ cut-off frequency which exists in a signal. The choice of the cut-off or highest frequency depends upon whether the signal is broadband or narrowband. A narrowband signal is a signal

whose power spectral density (PSD) represents a limited range of frequencies (significant frequencies) clearly distinguishable from other frequency components. In other frequencies, the power of a signal drops considerably after a certain frequency which is called the cut-off frequency ( $f_c$ ) and is defined as the frequency at which the power drops to  $-3$  db of its maximum value. The power of a narrowband signal at significant frequencies is almost at the same level as shown in Figure 4.5.

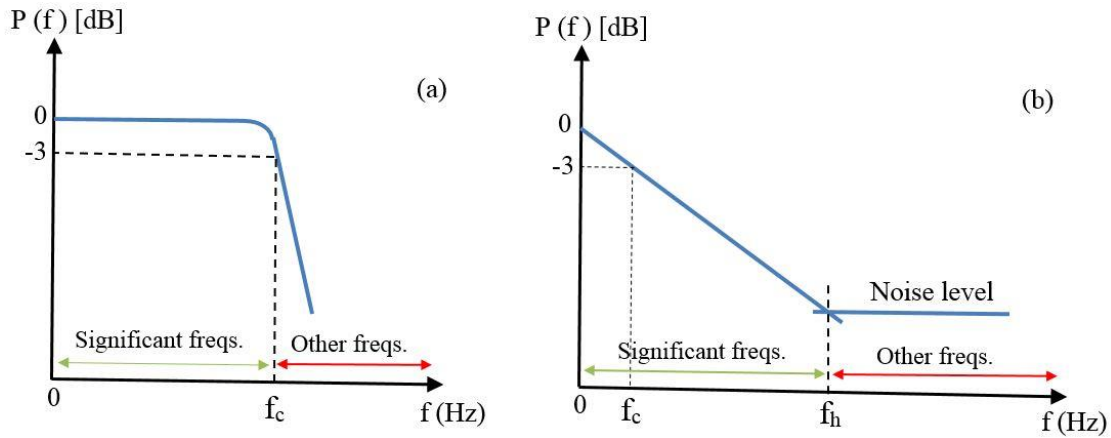


**Figure 4.5** Typical representation of power spectral density of (a) narrowband and (b) broadband signals.

On the other hand, a broadband signal contains a wide range of frequencies which constitute the power of the signal. In a broadband signal, the power changes gradually over a range of significant frequencies without having the same power level over that range. This gradual change of the power does not allow to consider the definition of cut-off frequency ( $-3$  db drop-off) for broadband signals when dealing with the Nyquist sampling theorem. Instead, the highest frequency component ( $f_h$ ) of a broadband signal is employed to find the sampling rate, *i.e.*,

$$\begin{aligned}
 f_s &\geq 2f_h \quad \text{for broadband signal} \\
 f_s &\geq 2f_c \quad \text{for narrowband signal}
 \end{aligned}
 \tag{4.5}$$

The highest frequency component is the frequency, according to the PSD plot, at which the noise level intersects the original power signal. To find the noise level, the Least Squares (LS) method can be employed. According to the definition, the noise level has a slope of zero in the PSD diagram. The LS is used to find out after which frequency the slope of the PSD plot equals almost zero (see Figure 4.5). One reason for using the highest frequency in lieu of the cut-off frequency is that there may be a power-law relationship between the frequencies and the power in a broadband signal [30]. Therefore, the use of cut-off frequency in a broadband signal leads to the loss of information about the signal. It should be noted that the classification of the broadband and narrowband signals entails comprehensive explanations, especially in the field of Communications, which is outside the scope of this thesis.

Based on the above explanation, one needs to find the PSD of the pressure signal to ensure if the signal is broadband or narrowband. Figure 4.6 shows the normalized PSD of the pressure signal taken from an experiment in the healthy operating mode. The highest frequency component was estimated at  $\log(f_h) \cong 2.47$  (i.e.,  $f_h \cong 295 \text{ Hz}$ ) because the slope of the yellow line, superimposed on the plot, became almost zero as shown in Figure 4.6. According to the Nyquist sampling theorem,  $f_s \geq 2f_h = 590 \text{ Hz}$ . Since the pressure data were captured at the sampling rate of  $1000 \text{ Hz}$ , the original pressure signal was therefore sampled properly by the Quanser<sup>®</sup> data acquisition system.

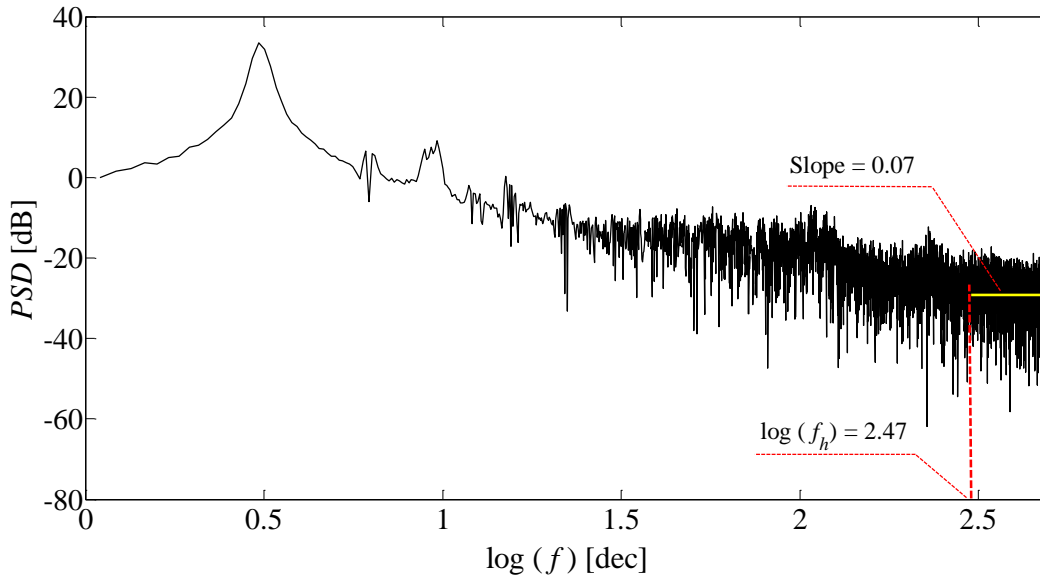


**Figure 4.6** Normalized power spectral density of signal  $P_1$  taken from an experiment in healthy operating mode. Highest frequency component is estimated at  $\log(f_h) = 2.47$ .

#### 4.2.1.3. Fractality Test

Many natural signals are scale-free which are called fractals. An object (*e.g.*, a geometric figure, a process or a time series) is fractal, if a portion of the whole is the scaled down version of the whole [30]. A well-known example of a fractal object is the Koch curve. As shown in Figure 4.7, small segments of the Koch curve resemble the structure of the whole curve. This feature leads to the definition of a new class of objects called “fractals”. There exist many dimensions describing fractal objects. These dimensions distinguish between the fractals (*e.g.*, Koch curve) and non-fractals (*e.g.*, a simple curve on a plane). There are two familiar dimensions: (i) Euclidean dimension ( $D_E$ ), and (ii) topological dimension ( $D_T$ ). Many objects have the same Euclidean and topological dimensions; however, they are not the same in the sense of geometric and information-

based features. Figure 4.7 compares a simple curve and the Koch curve. Both geometries have the same Euclidean ( $D_E = 2$ ) and same topological ( $D_T = 1$ ) dimensions. However, it does not mean that there is no difference between these two geometries. The Euclidean and topological dimensions are unable to provide enough information about some geometries (*e.g.*, Koch curve) and processes, and there is a need for a new definition of dimensions (*i.e.*, fractal dimensions). Note that the concept of fractality is not limited to the geometric objects. Extensive explanations on the fractals are found in [13], [30].

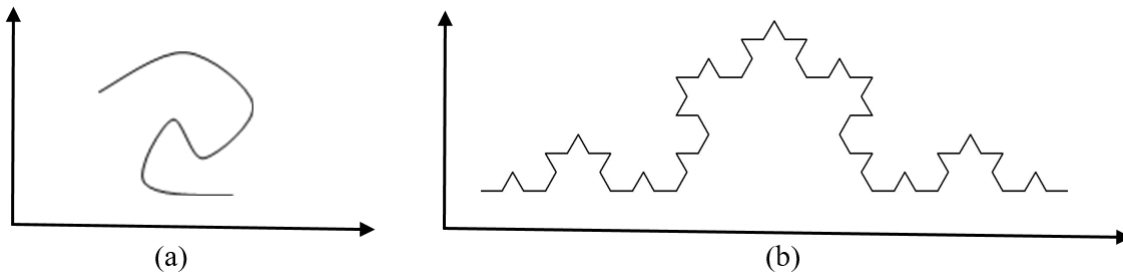


**Figure 4.7** Typical representation of fractal: (a) a non-fractal curve; (b) a fractal curve (Koch curve). Both curves have  $D_T = 1$  and  $D_E = 2$ .

Fractal objects can either be self-similar or self-affine. Self-similarity means that the scaling is isotropic (*i.e.*, the same scale along different coordinates). On the other hand, the self-affinity means that the scales along different coordinates are different [30]. A time series (*e.g.*, a time-domain signal) is self-similar, if

$$g(t, y) = g(rt, ry) \quad (4.6)$$

On the other hand, a time series is self-affine, if

$$g(t, y) = g(r_t t, r_y y) \quad (4.7)$$

where  $r_t \neq r_y$ . In industrial applications, there is no self-similar experimental data. Therefore, the self-affinity property of the signal is investigated mostly. To perform the multiscale analysis on the experimental data, one needs to ensure if the signal is a self-affine fractal. One of the fractality tests is to prove the self-affinity characteristic of a time series statistically. Statistical self-affinity means the statistical moments of the signal do not change under successive dilations. By dilation, a signal is captured in different partitioning sizes (*i.e.*, window sizes).

In this study, several successive dilations were performed on the pressure data, taken from an experiment in the healthy operating mode ( $P_1$  in Figure 4.2), to ensure that the signal is a self-affine fractal (see Figure 4.8). In each dilation level, first two statistical moments were calculated. Results showed that both mean and variance values of the pressure data hold almost constant under successive dilations. Therefore, the pressure signal could be considered as a self-affine time series. Table 4.1 reports the absolute values of the percentage of change of the mean ( $|\delta_{mean}|$ ) and that of the variance ( $|\delta_{var}|$ ) of each dilation level with respect to the mean and variance of the original signal. The percentage of changes confirms that the mean and the variance did not change considerably under successive dilations.

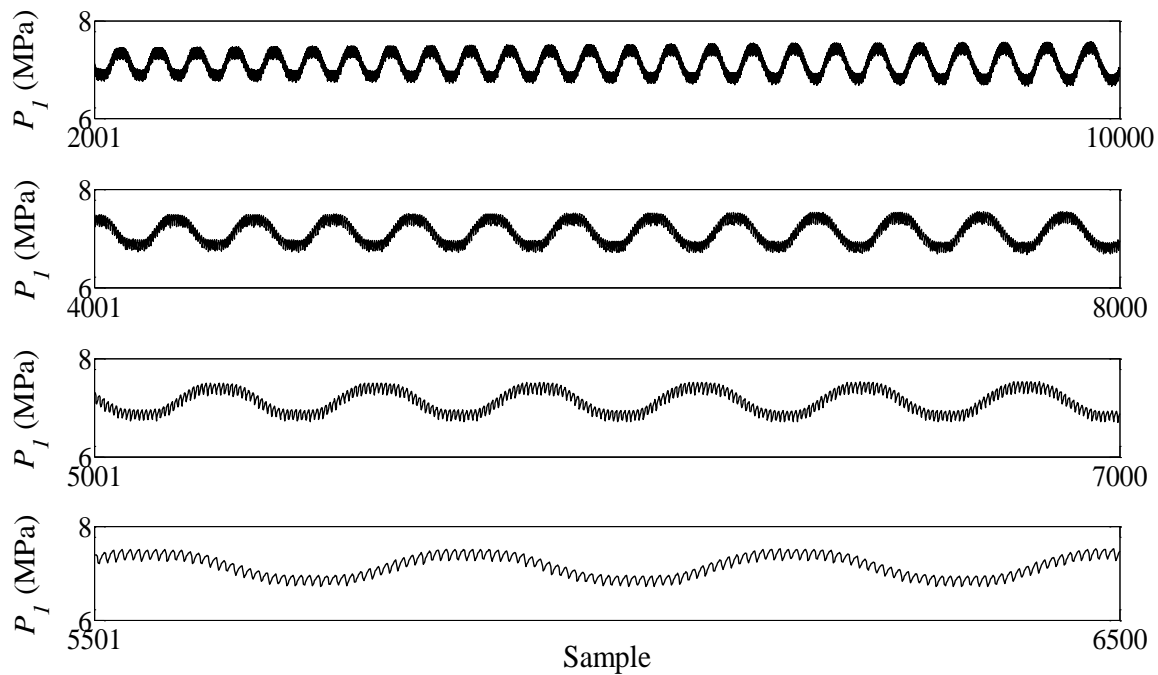


**Figure 4.8** Successive dilations of chamber one pressure signal ( $P_1$ ) taken from an experiment in healthy operating mode. Samples of interval [2001, 10000] are equivalent to time interval of [2, 10] sec.

**Table 4.1** Mean and variance of pressure signal at different dilation levels.

Dilation level [Samples]	Mean ( $\times 10^6$ )	$ \delta_{mean} $	Variance ( $\times 10^{10}$ )	$ \delta_{var} $
<b>Original signal</b> [2001, 10000]	7.1308	0	5.3466	0
<b>First level</b> [4001, 8000]	7.1320	0.017 %	5.3979	0.959 %
<b>Second level</b> [5001, 7000]	7.1248	0.084 %	5.3640	0.325 %
<b>Third level</b> [5501, 6500]	7.1485	0.248 %	5.4378	1.704 %

#### 4.2.1.4. Tsonis Test

To analyze a fractal time series, a minimum number of data points is required, because most of the fractal dimensions are obtained by reconstructing an embedding space from a single time series. The reconstruction procedure is explained later in this chapter. Some techniques have been proposed to calculate the number of data points required for the reconstruction of the embedding space properly [70]-[72]. Tsonis [72] developed a formula based on the correlation fractal dimension of a self-affine time series. According to [72], if the number of data points is less than a threshold ( $N_{min}$ ), further investigations may lead to false results. The relationship between a minimum number of required data points and the correlation fractal dimension is given by [13], [72]

$$N_{min} = 10^{2+0.4D_c} \quad (4.8)$$

where  $D_c$  is the correlation dimension. Since the correlation dimension should be calculated after reconstructing the embedding space (see section 4.2.2.2), one can use the box-counting fractal dimension instead of the correlation one in this step of analysis. The box-counting dimension is always equal or larger than the correlation dimension, for a self-affine time series, and can be considered as the upper bound of the correlation fractal dimension [16]. There exist various dimensions indicating rate of the complexity of a fractal [16]. Box-counting dimension is one of the morphological fractal dimensions that, in this study, is used to determine the minimum number of required data points. To calculate this dimension, the sampled data of the pressure signal are covered by non-overlapping volume elements (so called “vels” or “r-covers”) [16]. The vels attribute different sizes in different stages of covering. For a fractal object, there is a power-law relationship between the number of the vels covering the fractal and the size of each vel. This

power-law relationship leads to the definition of the box-counting fractal dimension as follows [16]

$$D_{HM} = \lim_{r \rightarrow 0} \frac{\log(N_r)}{\log(1/r)} \quad (4.9)$$

In Eq. (4.9),  $N_r$  is the number of vels covering the time series, and  $r$  is the size of each vel.  $D_{HM}$  is called the box-counting dimension. To plot  $\log(N_r)$  over  $\log(1/r)$ , several stages of iteration are required based on different vel sizes. The box-counting dimension is then calculated from the slope of  $\log(N_r) - \log(1/r)$  plot using the linear Least Squares technique, as shown in Figure 4.9. With respect to Figure 4.9,  $D_{HM}$  of the pressure signal  $P_1$  of Figure 4.2 was equal to 1.619. Then, the minimum number of required data points was set to 445 based on Tsonis criterion [Eq. (4.8)]. In all calculations, at least 1000 sampled data of the pressure signal were used; therefore, the Tsonis criterion was met in this study.

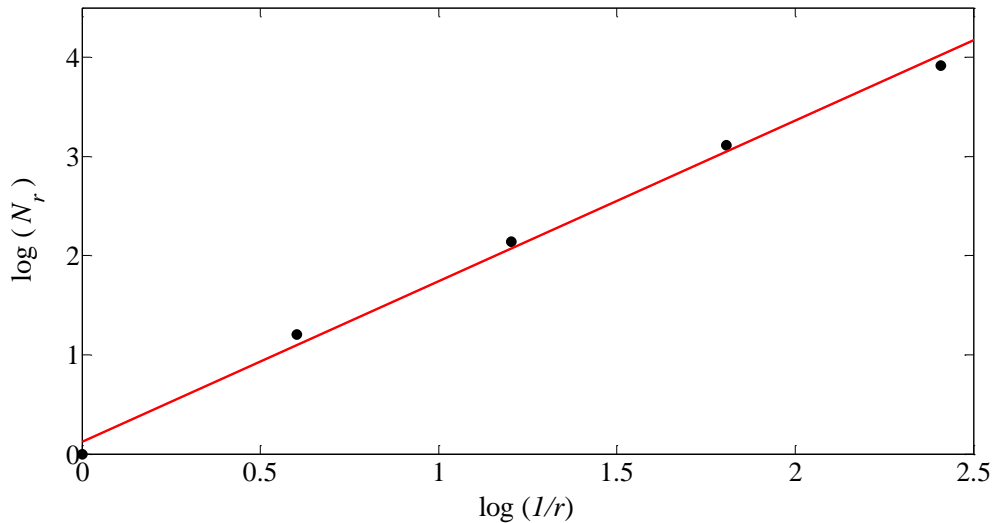


**Figure 4.9** Log-log plot for calculating box-counting dimension. Line is obtained using linear Least Squares technique. Slope of line reflects box-counting dimension.

Total number of data points obtained from the experimental setup was equal to 10000 (equivalent to the time interval  $[0, 10]$  sec). By excluding the data of the transient response (*i.e.*, first 2000 data points), only 8000 data of the pressure signal ( $[2, 10]$  sec) have so far been used for the analysis (see Table 4.1). Considering the long computational time for calculating various multiscale measures and fractal dimensions for the internal leakage detection, 1000 sampled data points were employed in steps 2 and 3 of Figure 4.1. The fractality property of the pressure signal allows us to use this number of data points ( $= 1000$ ) in further calculations; because, a portion of a fractal signal can be used, for the analysis, instead of the whole signal. Moreover, the third level of dilation (*e.g.*, data points of the interval  $[5501, 6500]$ ) contains 1000 samples, and the pressure signal is stationary within the window size of 1000 samples (see section 4.2.1.1). Thus, the third level of the dilation was chosen for further multiscale analysis.

#### 4.2.2. Preliminary Calculations

A preliminary study is required before quantifying the multiscale measures. To perform most parts of the multiscale analysis, an embedding space must be constructed from a single signal (*e.g.*, the pressure signal  $P_1$ ). Furthermore, finding an optimum lag between the data points is a key factor in reconstructing the embedding space properly [73]. In addition to the optimum lag, one needs to find a minimum embedding dimension for further analyses. The calculation of the minimum embedding dimension is essential because the reconstruction may give rise to the false results if the number of dimensions is less than a certain minimum value. Therefore, this section deals with the calculation of an optimal lag, the reconstruction of the embedding space and the determination of a minimum embedding dimension.

### 4.2.2.1. Optimum Lag

Determination of an optimum lag (*i.e.*, time delay) between the data points is one of the important stages in the multiscale analysis of experimental data. Optimum lag is required to reconstruct an embedding space using available sampled data. In this study, the optimal lag is obtained by using the concept of the minimum mutual information [74]-[76]. The mutual information is a concept dealing with the probability of the existence of each data point of time series in various bins. It is a measure of how much one knows about each sampled data at next time step [*i.e.*,  $x(i + 1)$ ] if  $x(i)$  is given [13]. Considering different bins, the mutual information index is calculated as a function of the lag ( $\tau$ ) between the data points as follows [74]-[76]

$$I(\tau) = \sum_{i=1}^N \sum_{j=1}^N P_{ij}(\tau) \ln(P_{ij}(\tau)) - 2 \sum_{i=1}^N P_i \ln(P_i) \quad (4.10)$$

where  $I$  is the mutual information index;  $P_i$  denotes the probability that  $x(n)$  is located in bin  $i$ , and  $P_{ij}$  represents the probability that  $x(n)$  is in bin  $i$  and  $x(n + \tau)$  is in bin  $j$ . Note that  $x(n)$  is the value of the signal in  $n^{\text{th}}$  sample. The Optimum value of the lag, for a given time series, is where the first local minimum of the index  $I$  is generated. Details about the mutual information technique are provided in [74]-[76]. In this step of the analysis of the pressure signal ( $P_1$  in Figure 4.2), the values of the index  $I$  was obtained for various lags. Figure 4.10 shows how the value of  $I$  changes in terms of the lag values. As shown, the first minimum of mutual information index occurred at the lag equal to 9. Therefore, this value was considered as an optimum lag for reconstructing the embedding space.

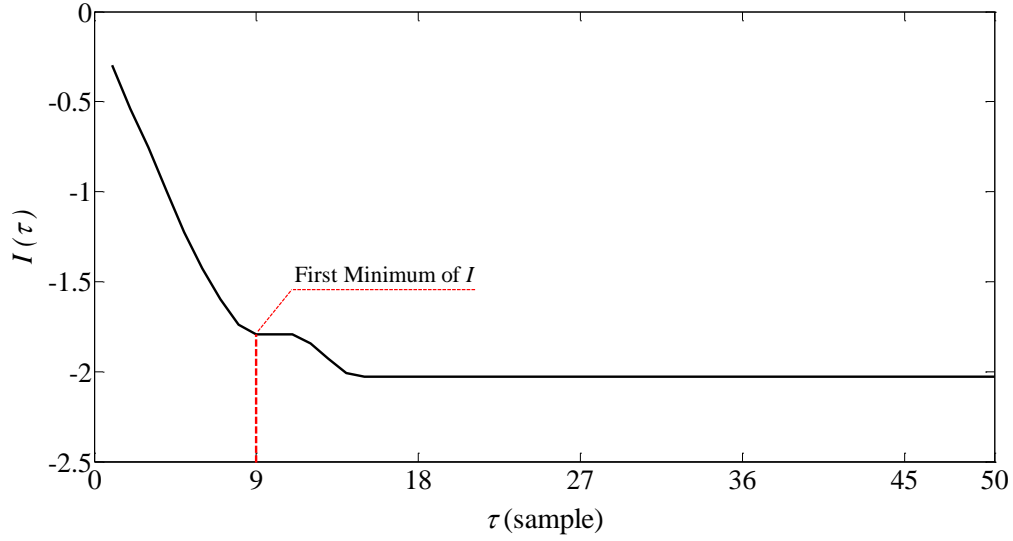


**Figure 4.10** Mutual information ( $I$ ) in terms of different lags ( $\tau$ ); Results were obtained by applying mutual information technique to pressure data  $P_1$  of Figure 4.2.

#### 4.2.2.2. Reconstruction of Embedding Space

The first step in calculation of the minimum embedding dimension and some of the fractal dimensions is the reconstruction of an embedding space. Suppose that there is only one available set of sampled data (*e.g.*, the pressure data in our case of study). It is possible to reconstruct an embedding space from the available set of data points. The sampled data contains more information than only a set of pressure values at different time steps. Because, the change in the value of the pressure data from sample  $n_i$  to  $n_{i+1}$  is an implicit function of other state variables of the system. The procedure of reconstructing an embedding space from a single time series (*e.g.*, the pressure data  $P_1$  in this research) is shown in Table 4.2 given  $N$  data points. As illustrated, the number of the reconstructed points ( $M$ ), in the embedding space, depends upon the lag ( $\tau$ ) between the data points and the embedding dimension  $m$ . This relationship is given by [73]

$$M = N - (m - 1)\tau \quad (4.11)$$

**Table 4.2** Reconstruction of embedding space based on embedding dimension and lag.

Reconstructed points	Different embedding dimensions					
	1	2	3	...	$m-1$	$m$
$\mathbf{X}_1$	$x_1$	$x_{1+\tau}$	$x_{1+2\tau}$	...	$x_{1+(m-2)\tau}$	$x_{1+(m-1)\tau}$
$\mathbf{X}_2$	$x_2$	$x_{2+\tau}$	$x_{2+2\tau}$	...	$x_{2+(m-2)\tau}$	$x_{2+(m-1)\tau}$
$\vdots$	$\vdots$	$\vdots$	$\vdots$	$\vdots$	$\vdots$	$\vdots$
$\mathbf{X}_M$	$x_{N-(m-1)\tau}$	$x_{N-(m-2)\tau}$	$x_{N-(m-3)\tau}$	...	$x_{N-\tau}$	$x_N$

The set  $\{\mathbf{X}_i\}$  ( $i = 1, 2, \dots, M$ ) constitutes the reconstructed points in an  $m$ -dimensional embedding space, where  $m$  is the embedding dimension obtained in section 4.2.2.3. The components of each vector  $\mathbf{X}_i$  is obtained from the data points of the single time-series (*i.e.*, the pressure signal  $P_1$ ) as follows

$$\mathbf{X}_i = (x_i, x_{1+\tau}, x_{1+2\tau}, \dots, x_{1+(m-2)\tau}, x_{1+(m-1)\tau}) \quad i = 1, 2, \dots, M \quad (4.12)$$

To reconstruct an embedding space properly, it is important to obtain a minimum embedding dimension for the reconstruction. If the embedding space reconstructed from experimental data has a dimension less than a certain value, the further analyses based on that embedding space may lead to false results, because, each  $\mathbf{X}_i$  will not represent a unique state vector of the original system. This concept is equivalent to the concept of the state-space variables in the dynamic systems. As known, the number of state variables is equal to the number of independent variables which describe dynamic behaviors of a system. For instance, a system of mass-spring-damper, cannot be represented, in the state space form, with only one state variable, and at least two state variables are required in order to describe the system dynamic properly. The minimum embedding

dimension has the equivalent meaning in the dynamic systems. Next section explains how to determine of a minimum embedding dimension followed by the results representing the consistency between the obtained embedding dimension and the number of state variables defining the experimental setup under study.

#### 4.2.2.3. Minimum Embedding Dimension

Given an optimum lag, different embedding spaces can be reconstructed based on different embedding dimensions. For a time series, a minimum embedding dimension is required for further analyses such as the quantification of maximal Lyapunov exponent or the correlation entropy. There exist various techniques to find a minimum embedding dimension for a dynamic system with a given time series [77]-[81]. These techniques have their own shortcomings. For instance, the one proposed by Grassberger and Procaccia [79] is often very subjective and time consuming for computation [82]. The method of false neighbors [81] is also subjective in some sense for saying that a neighbor is false, where different values of thresholds may lead to different results [82]. Cao's method [82] is a practical technique for obtaining a minimum embedding dimension from a single time series. This technique is based on the idea of the false neighbor developed by Kennel *et al* [81]. Cao's method has overcome shortcomings of previously presented techniques [82]. This method considers a reconstructed embedding space, described earlier, using an optimum lag. First, the following index is defined [82]:

$$a(i, m) = \frac{\|\mathbf{X}_i(m+1) - \mathbf{X}_{n(i,m)}(m+1)\|}{\|\mathbf{X}_i(m) - \mathbf{X}_{n(i,m)}(m)\|} \quad (4.13)$$

where  $\|\cdot\|$  is the distance between two reconstructed points in  $m$ -dimensional space. Here, the Euclidian distance is used for further calculations.  $\mathbf{X}_i(m)$  is the  $i^{th}$  point in  $m$ -dimensional

reconstructed space. The subscript  $n(i, m)$  is an integer such that  $\mathbf{X}_{n(i, m)}(m)$  is the nearest neighbor of  $\mathbf{X}_i(m)$ . Then, the index  $a(i, m)$  is calculated for all reconstructed points followed by obtaining the following ratio

$$E(m) = \frac{1}{M} \sum_{i=1}^M a(i, m) \quad (4.14)$$

Lastly, to investigate the variation of  $E(m)$  from the embedding dimension of  $m$  to  $m + 1$ , the index  $E_1(m)$  is defined as follows

$$E_1(m) = \frac{E(m + 1)}{E(m)} \quad (4.15)$$

By plotting  $E_1(m)$  for various values of the embedding dimension, Cao found that  $E_1(m)$  stops changing after a specific dimension of  $m_0$ , if the time series comes from an attractor. Then,  $(m_0 + 1)$  is the minimum embedding dimension [82]. Hereafter, the Cao's index is denoted by  $E_1$ . To calculate a minimum embedding dimension from the available experimental data (*i.e.*,  $P_1$  in Figure 4.2), nine embedding spaces were reconstructed based on the optimum lag of 9 and nine embedding dimensions ( $m = 2, 3, \dots, 10$ ). Then, the Cao's index ( $E_1$ ) was calculated using Eqs. (4.13) to (4.15). Figure 4.11 illustrates the variations of the Cao's index versus the embedding dimension. It confirms that minimum embedding dimension equals  $m = 6$  for given time series; because, the index  $E_1$  stops changing considerably after  $m = 5$ . Note that a minimum embedding dimension can be a representative of the number of state variables in the state space equations of a system. This is in line with the mathematical modeling of the tested hydraulic system [see Eq. (3.10)] as well as the result obtained by Cao's method.

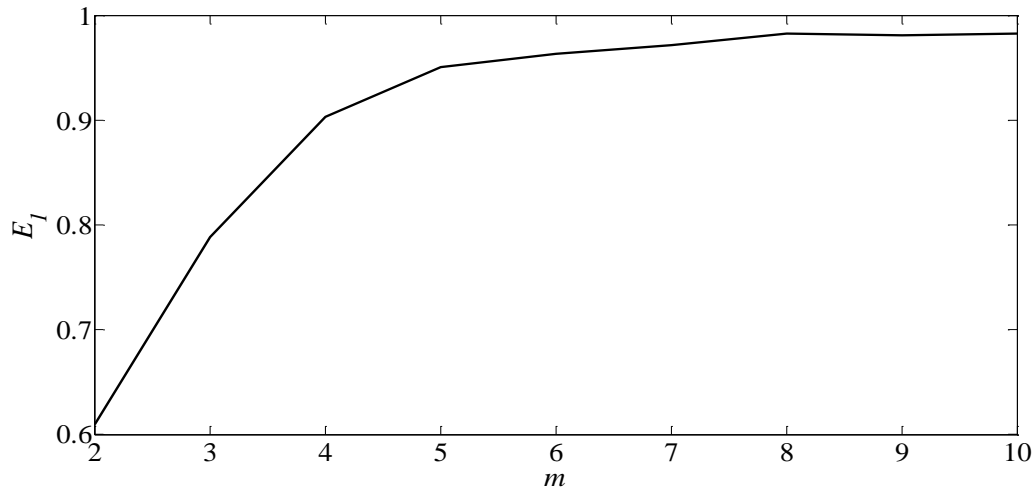


**Figure 4.11** Cao's index ( $E_1$ ) as a function of embedding dimension ( $m$ ). Plot was obtained by calculating  $E_1$  of pressure signal of Figure 4.2.

#### 4.2.3. Quantification of Multiscale Measures

Having performed the preliminary study, five multiscale measures were quantified in all healthy and faulty operating modes, and the sensitivity of each measure to the effect of the internal leakage on the pressure data was obtained by calculating the percentage of change of faulty measures with respect to values of the healthy operating mode. The measures consist of correlation fractal dimension, variance fractal dimension, maximal Lyapunov exponent, correlation entropy (the close lower bound on Kolmogorov-Sinai entropy) and wavelet coefficients. In this section, the explanations on each measure is provided. In addition, the results of calculating each multiscale measure for the pressure data of the healthy operating mode are pictorially shown here.

### 4.2.3.1. Correlation Fractal Dimension

Correlation fractal dimension is a major improvement of the geometric definition of a covering of a fractal (*e.g.*, self-affine time series) by  $N_r$  vels of size  $r$  by considering the average density of the fractal to resolution of  $r$  [30]. Visualize an embedding space with the embedding dimension of  $m$ . If the number of reconstructed points, in the embedding space, equals  $M$ , the correlation sum of all points lying within the  $m$ -dimensional hyper-sphere of radius  $r$  is calculated as follows [13]

$$C(r) = \frac{2}{M(M-1)} \sum_{j=1}^M \sum_{i=j+1}^M \Theta(r - r_{ij}) \quad (4.16)$$

where  $C(r)$  represents the correlation sum;  $r_{ij}$  is the spatial separation between two reconstructed points labeled  $i$  and  $j$ . According to the Pythagorean theorem,  $r_{ij}$ , in an  $m$ -dimensional time delay embedding space, is calculated as follows [13]

$$r_{ij} = \sqrt{\sum_{k=0}^{m-1} (\mathbf{X}_{i-k} - \mathbf{X}_{j-k})^2} \quad (4.17)$$

Note that  $\mathbf{X}$  denotes the vector of the reconstructed state space. In Eq. (4.16),  $\Theta$  is the Heaviside function, and is defined as [13]

$$\Theta(y) = \begin{cases} 0 & \text{if } y < 0 \\ 1 & \text{if } y \geq 0 \end{cases} \quad (4.18)$$

There is a power-law relationship between  $C(r)$  and  $r$  for a set of self-affine sampled data which is defined by [13]

$$D_c = \lim_{r \rightarrow 0} \frac{\log(C(r))}{\log(r)} \quad (4.19)$$

where  $r$  is the size of each vel ( $m$ -dimensional hyper-sphere) covering the points. To plot  $\log(C(r))$  vs.  $\log(r)$ , several stages of iteration are considered based on different values of  $r$ . The correlation fractal dimension is then calculated from the slope of the log-log plot by applying the linear Least Squares technique to the obtained data points.

For the pressure signal of the healthy operating mode (*i.e.*,  $P_1$  in Figure 4.2), the log-log plot of Eq. (4.19) was obtained. The embedding space was reconstructed based on  $m = 6$  and  $\tau_{opt} = 9$ . Figure 4.12 illustrates how  $\log(C(r))$  changes in terms of  $\log(r)$  in a 6-dimensional embedding space. The value of the correlation fractal dimension was obtained from the slope of the line superimposed on the plot.

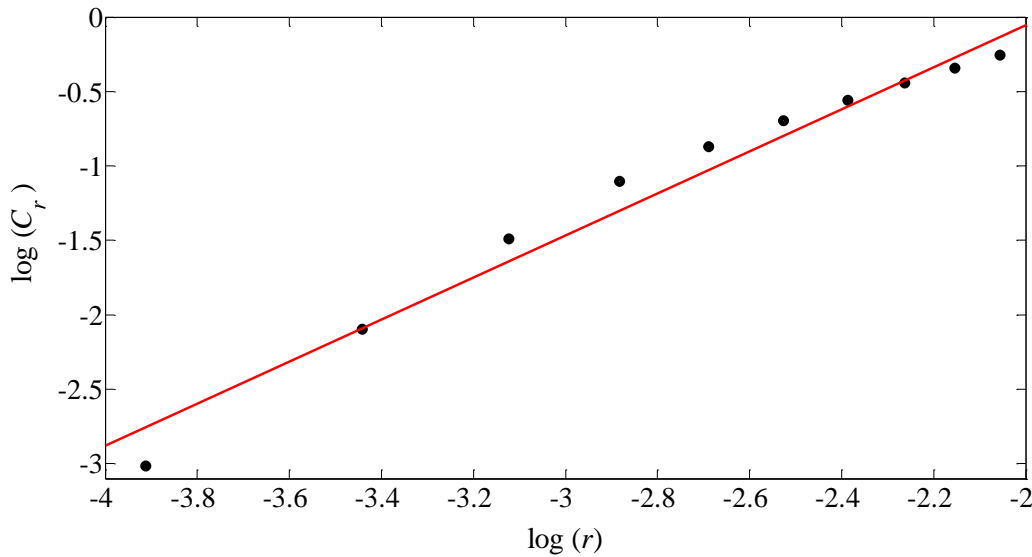


**Figure 4.12** Representation of log-log plot for calculation of correlation fractal dimension. Line is obtained from linear Least Square regression of scattered points. Slope of line is equal to correlation dimension.

### 4.2.3.2. Variance Fractal Dimension

A time series can be analyzed directly in time domain by analyzing spread of the increments in the signal amplitude measured necessarily at different scales [30]. In each step, the size of window, containing the data points, differs from that of another step. For a self-affine time series, there is a power-law relationship between the variance of amplitude increments and the time increment as follows [83], [84]

$$\text{Var}[B(t_2 - t_1)] \sim |t_2 - t_1|^{2H} \quad (4.20)$$

where,  $B$  means the amplitude of the signal, and  $H$  is called the Hurst exponent. For a set of sampled data, the term  $t_i$  is substituted by  $n_i$  indicating the counter of data point in  $i^{\text{th}}$  sample. The Hurst exponent is then obtained as follows

$$H = \frac{1}{2} \lim_{\Delta n \rightarrow 0} \frac{\log[\text{Var}(\Delta B)_{\Delta n}]}{\log(\Delta n)} \quad (4.21)$$

To calculate  $H$ , the procedure proposed in [83] is followed such that the windows of data are chosen based on a statistical range limiting method that does not allow the window size to be either too small or too large. The variance fractal dimension,  $D_\sigma$ , is defined as

$$D_\sigma = D_E + 1 - H \quad (4.22)$$

In Eq. (4.22),  $D_E$  is the number of the independent variables of the signal, which equals 1 for a single-variable time series. For the pressure signal of the healthy operating mode, the variance dimension was obtained based on Eqs. (4.20) to (4.22). First  $\log[\text{Var}(\Delta B)]$  vs.  $\log(\Delta n)$  was plotted, and the Hurst exponent ( $H$ ) was calculated from half of the slope of log-log plot. Afterwards, the variance fractal dimension was calculated using Eq. (4.22). With respect to Figure 4.13, the value of the variance fractal dimension of the pressure signal ( $P_1$ ) was equal to 1.17.

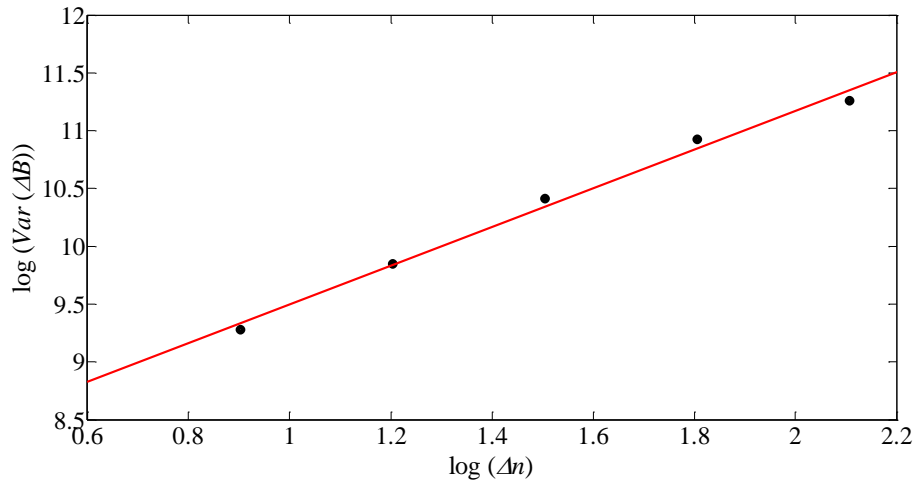


**Figure 4.13** Log-log plot of variance of amplitude increments vs. different data window sizes. Line is obtained using linear Least Squares method. Hurst exponent equals half of slope value.

#### 4.2.3.3. Maximal Lyapunov Exponent

Maximal Lyapunov exponent is usually utilized as one of the indicators in discerning the type of a system in the sense of chaos and reveals useful information about the stability problem of a dynamical system. In this study, this measure is used to observe if it is sensitive to a certain type of fault. The Lyapunov exponents can be determined using model-based techniques such as the one proposed by Gencay and Dechert [85]. According to [85], a model of the original system can be found from a set of observations using estimate techniques such as the neural network. Then, the  $n$  largest Lyapunov exponents of the estimate function will be the same as the Lyapunov exponents of the original system. Determination of Lyapunov exponent(s) of a system from experimental data is fraught with pitfalls and subtleties. Wolf's [86] and Kruel's [87] algorithms were proposed to obtain the Lyapunov exponents from experimental data; however, they were not strong in distinguishing chaos from the noise. Rosenstein *et al.* [73] developed a technique to find

the maximal Lyapunov exponent from the experimental data. Their approach is based on looking for the nearest point ( $X_l$ ) to each reconstructed point ( $X_n$ ) in an  $m$ -dimensional embedding space [13]. Note that  $m$  is the minimum embedding dimension obtained by Cao's method. According to [13] and [73], the logarithmic rate of separation of these two points ( $X_l$  and  $X_n$ ) for the next  $k$  time steps is obtained as

$$L_k = \frac{1}{2(N - k - m + 1)} \sum_{n=m}^{N-k} \log \left[ \sum_{j=0}^{m-1} (X_{l-j+k} - X_{n-j+k})^2 \right] \quad (4.23)$$

The largest Lyapunov exponent is then given by  $\lambda_1 = \frac{dL_k}{dk}$  at middle values of  $k$  [13]. To quantify the maximal Lyapunov exponent of given time series (the pressure signal of healthy operating mode), the plot of the index  $L_k$  in terms of some values of  $k$  was obtained based on the minimum embedding dimension (*i.e.*,  $m = 6$ ). Then, the slope was calculated for the middle time steps as shown in Figure 4.14. The result indicates that  $\lambda_1 \approx -0.14$  while the system operated under the healthy mode.

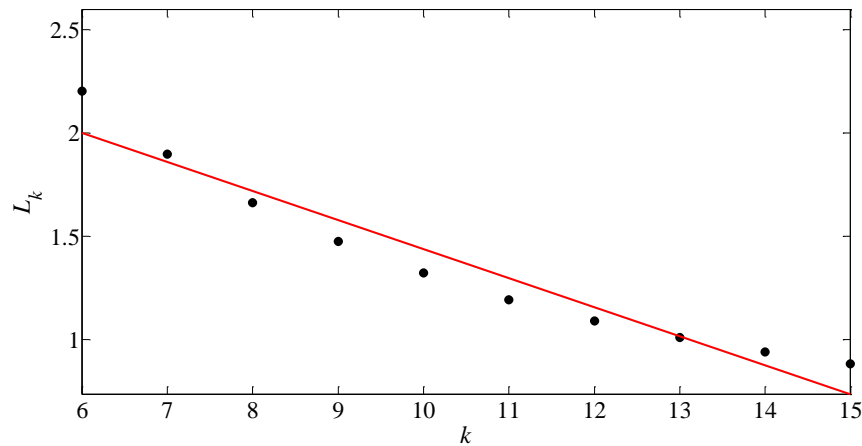


**Figure 4.14** Plot of index  $L_k$  in terms of different time steps  $k$  for determining maximal Lyapunov exponent. Slope ( $\lambda_1$ ) equals maximal Lyapunov exponent.

#### 4.2.3.4. Correlation Entropy

Another measure for distinguishing chaotic systems from non-chaotic ones and noise is the Kolmogorov-Sinai (KS) entropy proposed by Kolmogorov and refined by Sinai. The KS entropy is a measure of the information loss per iteration in an  $m$ -dimensional state space [13]. Mathematically, it is the sum of the positive Lyapunov exponents of a system [88]. In this research, a different version of this measure is obtained from the experimental data to find out how much sensitive it can be to the actuator internal leakage. The KS entropy is difficult to calculate. Another alternative is to use the higher-order entropy,  $K_2$ , which is a close lower bound on the KS entropy [89]-[91]. The Grassberger-Procaccia procedure uses the following definition for  $K_2$  [90]

$$K_2 = \lim_{m \rightarrow \infty} K_{2,r} \quad (4.24)$$

$$K_{2,r} = \lim_{r \rightarrow 0} \log \left[ \frac{C(m,r)}{C(m+1,r)} \right] \quad (4.25)$$

where,  $C(m,r)$  is the correlation sum, defined in Eq. (4.16), for an embedding dimension of  $m$ .  $K_2$  is so-called *the correlation entropy*. To find  $C(m,r)$ , the embedding space has been reconstructed based on the optimum lag obtained from the mutual information method. The close lower bound on the KS entropy (*i.e.*, the correlation entropy) was obtained for different embedding dimensions. The plot of  $\log(C_r)$  vs.  $\log(r)$  was sketched in different embedding dimensions as shown in Figure 4.15. Then, the index  $K_{2,r}$  was calculated using Eq. (4.25). For a chaotic system, the correlation entropy ( $K_2$ ) is the horizontal asymptote of index  $K_{2,r}$  when  $m$  approaches infinity [90]. Figure 4.16 shows variations of this index in terms of the embedding dimension. As this hydraulic system is non-chaotic, the correlation entropy cannot be calculated exactly. Instead, the average value of  $K_{2,r}$  ( $\bar{K}_{2,r}$ ) was used as an indicator to investigate its sensitivity to the actuator internal leakage.

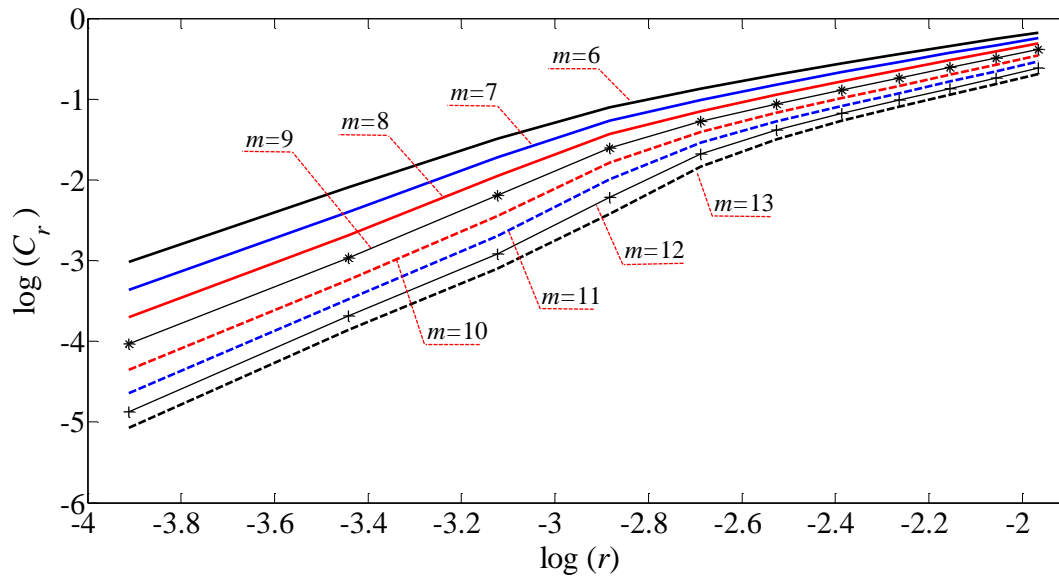


**Figure 4.15** Plot of  $\log(C_r)$  vs.  $\log(r)$  for different embedding dimensions ( $m = 6, \dots, 13$ ).

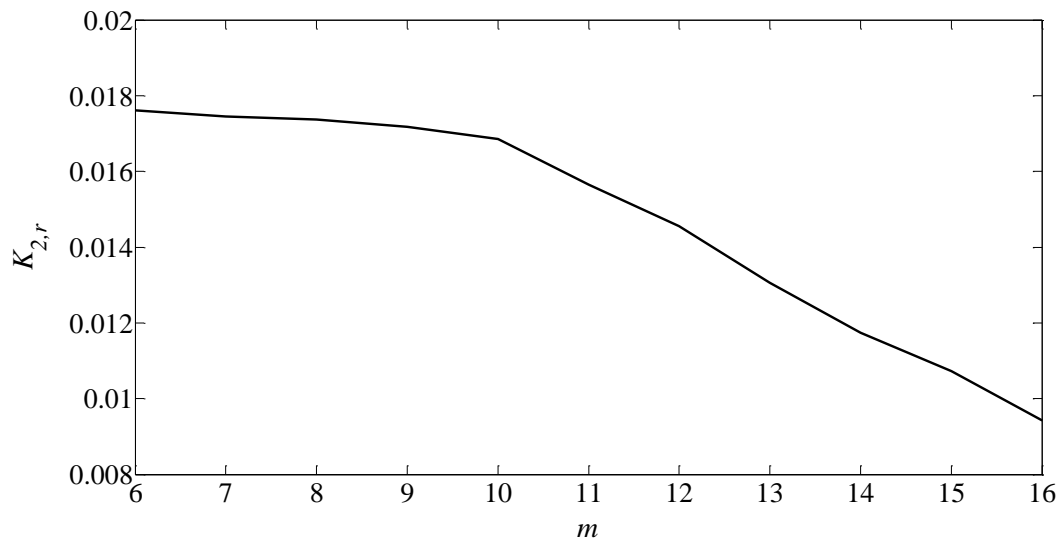


**Figure 4.16** Plot of index  $K_{2,r}$  in terms of embedding dimension  $m$ .

## 4.2.3.5. Wavelet Transform

A wavelet is a compactly-supported oscillatory waveform (of limited duration), with a zero average [92]. Wavelet Transform (WT) is an example of multiscale analysis as the wavelet coefficients are obtained from different partitioning of data points. Based on the wavelet theory, a basic function is defined as the mother wavelet function which is applied to the desired signal in order to extract a set of coefficients from that signal. The discrete wavelet transform (DWT) of discontinuous signal  $x(k)$  is defined as [93]

$$DWT(m, n) = a_0^{-\frac{m}{2}} \left[ \sum x(k) \psi^* \left( \frac{k - na_0^m b_0}{a_0^m} \right) \right] \quad (4.26)$$

where,  $a = a_0^m$  and  $b = na_0^m b_0$  are referred to as the scaling and shifting parameters;  $\psi(k)$  represents the mother wavelet function and the asterisk of  $\psi$  means its complex conjugate [11]. Note that the coefficients  $a_0$  and  $b_0$  are somehow chosen that the scaled and shifted mother wavelets construct an orthonormal basis. If  $a_0 = 2$  and  $b_0 = 1$ , the DWT constitutes an orthonormal basis called dyadic-orthonormal [93]. A well-known technique called *multiresolution signal decomposition* (MSD) has been developed to decompose the signal into scales with different time and frequency resolutions [94]. In order to apply the MSD technique to a signal, the following equations are defined [92]

$$\varphi(t) = \sum_{k=-\infty}^{+\infty} h(k) \sqrt{2} \varphi(2t - k) \quad (4.27)$$

$$g(k) = (-1)^k h(1 - k) \quad (4.28)$$

$$\psi(t) = \sum_{k=-\infty}^{+\infty} g(k) \sqrt{2} \varphi(2t - k) \quad (4.29)$$

where  $\varphi(t)$  is called the scaling function and  $h(k)$  is the impulse response coefficient for a low-pass filter which must fulfill the following conditions [92]

$$\sum_{k=-\infty}^{+\infty} |h(k)|^2 = 1 \quad ; \quad \sum_{k=-\infty}^{+\infty} h(k) = \sqrt{2} \quad (4.30)$$

The MSD technique decomposes signal  $x[n]$  into coefficients of  $a_1[n]$  and  $d_1[n]$  at first level of decomposition process. These coefficients are called the approximation and the detailed versions of the original signal  $x[n]$ , and are defined as [94]

$$a_1[n] = \sum_k h[k - 2n]x[k] \quad (4.31)$$

$$d_1[n] = \sum_k g[k - 2n]x[k] \quad (4.32)$$

where  $h[n]$  and  $g[n]$  are the associated low-pass and high-pass filter coefficients that decompose  $x[n]$  into  $a_1[n]$  and  $d_1[n]$ , respectively [11].

Quadrature mirror filter (QMF) pair is an approach that divides the signal into low- and high-frequency components at the dividing point of halfway between 0 Hz and half the data sampling frequency [95]. By passing the signal  $x$  from the low-pass filter (LPF) and the high-pass filter (HPF), the level one approximation and detailed versions of the signal are achieved as shown in Figure 4.17. Using the QMF approach, the detailed and approximation versions of the original signal are obtained up to the required level. In each level, the frequency bandwidth of decomposed signals is calculated by dividing the sampling frequency by  $2^j$ , where  $j$  is the decomposition level [11]. To find the required level of the decomposition, the feature frequency band must be determined first. The feature frequency band can be defined as a range of frequency at which the

signal behavior changes strictly after applying the fault [11]. By finding these bands, the decomposition levels required for the QMF approach are also obtained.

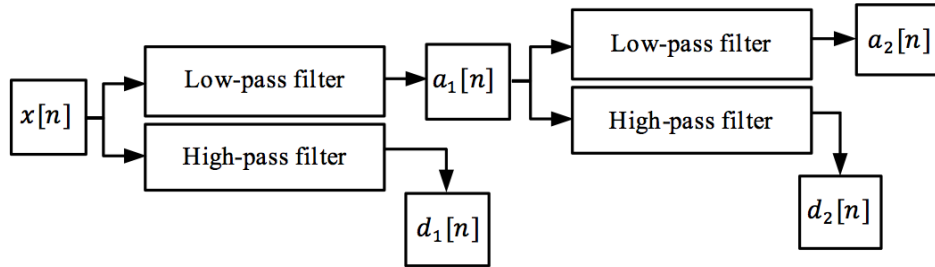


**Figure 4.17** Schematic of multiresolution signal decomposition technique based on quadrature mirror filter pair [12]. Two levels of decomposition are illustrated.

For the pressure signal of the healthy operating mode (*i.e.*,  $P_1$  in Figure 4.2), the plots of the wavelet detailed and approximation coefficients were obtained as illustrated in Figure 4.18 and Figure 4.19. The wavelet detailed and approximation coefficients of the pressure signal ( $P_1$ ) were obtained up to the level 5 of the decomposition using the combination of MSD and QMF techniques. The selection of an optimum mother wavelet function requires an extensive effort. In this study, various standard mother wavelet functions were examined to find out which one operates better in detecting various levels of the internal leakage. The mother wavelet function, used in this thesis, is Daubechies-8 function. From the implementation point of view, the Daubechies wavelet is a good choice for this application [28]. A high-order mother wavelet is better to avoid overlapping between two adjacent frequency bands [96].

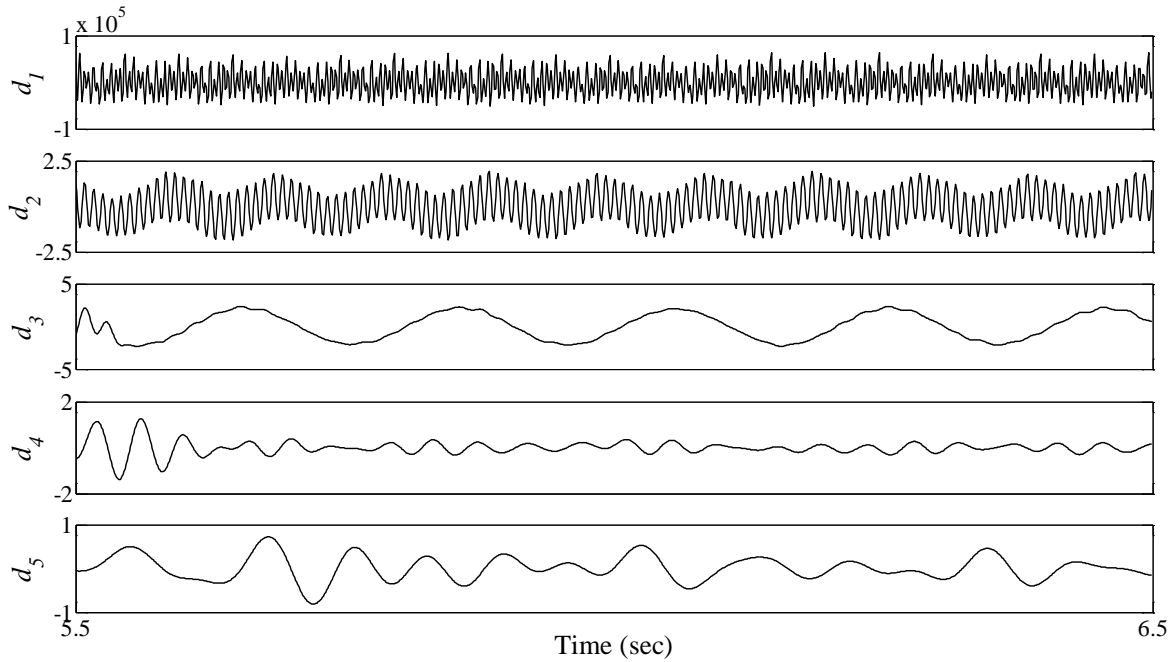


**Figure 4.18** Detailed coefficients of  $P_1$  of healthy hydraulic actuator. Time interval of [5.5, 6.5] sec is equivalent to samples of [5501, 6500].

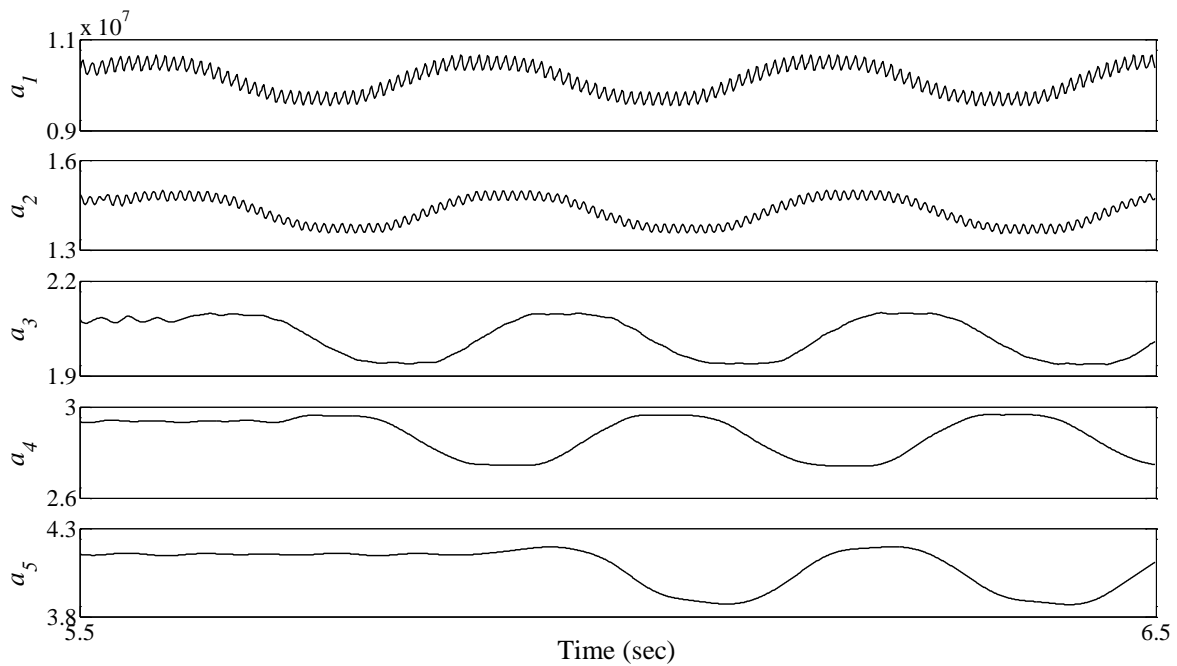


**Figure 4.19** Approximation coefficients of  $P_1$  of healthy hydraulic actuator.

**4.3. Results and Discussion**

A program was developed in MATLAB® to conduct the multiscale analysis. Steps of the given flowchart (Figure 4.1) were applied to the signal  $P_1$  measured in all healthy and faulty operating modes. Four operating modes, including (i) no leakage or “NL” ( $\bar{Q}_l = 0.09 L/min$ ), (ii) small leakage or “SL” ( $\bar{Q}_l = 0.22 L/min$ ), (iii) medium leakage or “ML” ( $\bar{Q}_l = 0.65 L/min$ ), and (iv) large leakage or “LL” ( $\bar{Q}_l = 1.19 L/min$ ), were considered and five multiscale measures were quantified for each mode in order to find the most reliable indicator(s) in detecting the actuator internal leakage. In each operating mode, three experiments were conducted, and all measures were obtained for each experiment. Table 4.3 lists the values of the correlation and variance fractal dimensions, the maximal Lyapunov exponent and the average of correlation entropy as well as the RMS values of wavelet coefficients for 12 experiments. Moreover, the average values of each multiscale measure, in separate operating modes, were calculated for further analysis.

**Table 4.3** Multiscale measures obtained in healthy and faulty operating modes. Three experiments were conducted in each operating mode.

Operating Mode	Healthy Mode				Faulty Modes												
	No Leakage (NL) ( $\bar{Q}_l = 0.09 L/min$ )				Small Leakage (SL) ( $\bar{Q}_l = 0.22 L/min$ )				Medium Leakage (ML) ( $\bar{Q}_l = 0.65 L/min$ )				Large Leakage (LL) ( $\bar{Q}_l = 1.19 L/min$ )				
Number of Experiment	Experiment 1	Experiment 2	Experiment 3	Average ( $\bar{H}$ )	Experiment 1	Experiment 2	Experiment 3	Average ( $F_{SL}$ )	Experiment 1	Experiment 2	Experiment 3	Average ( $F_{ML}$ )	Experiment 1	Experiment 2	Experiment 3	Average ( $F_{LL}$ )	
$D_c$	1.412	1.431	1.406	1.416	1.413	1.407	1.406	1.409	1.321	1.358	1.344	1.341	1.201	1.188	1.045	1.145	
$D_\sigma$	1.177	1.159	1.196	1.177	1.137	1.163	1.144	1.148	1.181	1.157	1.181	1.173	1.281	1.252	1.325	1.286	
$\lambda_1[(-1)]$	0.139	0.136	0.141	0.139	0.140	0.139	0.141	0.140	0.139	0.137	0.136	0.137	0.138	0.137	0.131	0.135	
$\bar{K}_{2,r} (\times 10^{-2})$	1.469	1.449	1.477	1.465	1.491	1.477	1.459	1.476	1.354	1.353	1.367	1.358	1.125	1.069	1.114	1.103	
RMS Values	$d_1 (\times 10^{+5})$	0.276	0.273	0.275	0.275	0.274	0.274	0.273	0.274	0.279	0.277	0.276	0.377	0.286	0.284	0.283	0.284
	$d_2 (\times 10^{+5})$	0.984	0.968	0.979	0.977	0.971	0.969	0.966	0.969	0.998	0.989	0.985	0.991	1.016	1.009	1.006	1.010
	$d_3 (\times 10^{+5})$	1.547	1.525	1.547	1.540	1.524	1.526	1.516	1.522	1.571	1.552	1.553	1.559	1.596	1.586	1.588	1.590
	$d_4 (\times 10^{+5})$	0.182	0.182	0.181	0.182	0.174	0.178	0.186	0.179	0.179	0.176	0.181	0.179	0.184	0.182	0.186	0.184
	$d_5 (\times 10^{+5})$	0.244	0.264	0.278	0.262	0.169	0.177	0.177	0.174	0.138	0.134	0.142	0.138	0.115	0.114	0.115	0.115
	$a_1 (\times 10^{+7})$	1.021	1.011	1.022	1.018	1.013	1.014	1.012	1.013	1.029	1.025	1.024	1.026	1.057	1.051	1.048	1.052
	$a_2 (\times 10^{+7})$	1.442	1.429	1.446	1.439	1.433	1.434	1.432	1.433	1.455	1.449	1.448	1.451	1.495	1.487	1.482	1.488
	$a_3 (\times 10^{+7})$	2.039	2.021	2.045	2.035	2.026	2.028	2.025	2.026	2.058	2.049	2.049	2.052	2.115	2.102	2.096	2.104
	$a_4 (\times 10^{+7})$	2.884	2.858	2.892	2.878	2.865	2.869	2.864	2.866	2.911	2.898	2.898	2.902	2.990	2.973	2.964	2.976
	$a_5 (\times 10^{+7})$	4.077	4.042	4.091	4.070	4.052	4.057	4.051	4.053	4.117	4.099	4.098	4.105	4.229	4.203	4.191	4.208

To observe the effect of the internal leakage on each measure, the percentage of change was determined using

$$\delta_i (\%) = \frac{H - F_i}{H} \times 100 \quad (4.33)$$

where  $\delta_i$  is the percentage of change of the faulty average value ( $F_i$ ) with respect to that of the healthy operating mode ( $H$ ). The subscript  $i$  is defined as "SL" for the small leakage, "ML" for the medium leakage and "LL" for the large leakage. By calculating the percentage of changes, the most sensitive measure to the actuator internal leakage was recognized. Table 4.4 shows how much the average value of each measure varies with respect to that of the healthy operating mode when the hydraulic actuator experiences the internal leakage. It is seen that variance fractal dimension and maximal Lyapunov exponent did not exhibit specific behaviors towards various levels of the internal Leakage. The average value of correlation entropy ( $\bar{K}_{2,r}$ ) and correlation fractal dimension could not detect a small level of the internal leakage ( $\bar{Q}_i = 0.22 \text{ L/min}$ ); however,  $\bar{K}_{2,r}$  has shown a change of 7.30% and 24.73% in the medium and large leakages, respectively. The corresponding values for the correlation dimension are 5.32% and 19.18%, which show the sensitivity of  $D_c$  to the medium and large levels of the internal leakage.

On the other hand, the level five wavelet detailed coefficient ( $d_5$ ) has shown a reliable sensitivity to various levels of the internal leakage. Therefore,  $d_5$  was found the most appropriate indicator to detect the internal leakage in the hydraulic actuator. In addition, other wavelet coefficients did not indicate considerable sensitivity to the internal leakage compared to  $d_5$ . Based on the multiscale analysis performed in this study, the computational time was variable for obtaining different multi-scale measures. For example, the wavelet transform was the most time-efficient technique for the internal leakage detection. All wavelet coefficients were obtained within

less than 2 sec, while the corresponding value for the calculation of average value of the correlation entropy was around 22 sec. All computations were performed using a PC with the processor Core i5-4590 running at 3.30 GHz.

**Table 4.4** Percentage of change of average values of multiscale measures in faulty modes with respect to those of healthy operating mode.

Operating Mode		Healthy Mode	Faulty Modes					
		NL	SL		ML		LL	
Average Value		$H$	$F_{SL}$	$\delta_{SL}$	$F_{ML}$	$\delta_{ML}$	$F_{LL}$	$\delta_{LL}$
$D_c$		1.416	1.409	0.54%	1.341	<b>5.32%</b>	1.145	<b>19.18%</b>
$D_\sigma$		1.177	1.148	2.49%	1.173	0.36%	1.286	-9.23%
$\lambda_1[\times(-1)]$		0.139	0.140	-0.96%	0.137	0.96%	0.135	2.40%
$\bar{K}_{2,r}(\times 10^{-2})$		1.465	1.476	-0.72%	1.358	<b>7.30%</b>	1.103	<b>24.73%</b>
RMS Values	$d_1(\times 10^{+5})$	0.275	0.274	0.36%	0.377	-0.97%	0.284	-3.52%
	$d_2(\times 10^{+5})$	0.977	0.969	0.85%	0.991	-1.39%	1.010	-3.41%
	$d_3(\times 10^{+5})$	1.540	1.522	1.14%	1.559	-1.23%	1.590	-3.27%
	$d_4(\times 10^{+5})$	0.182	0.179	1.28%	0.179	1.65%	0.184	-1.28%
	$d_5(\times 10^{+5})$	0.262	0.174	<b>33.46%</b>	0.138	<b>47.32%</b>	0.115	<b>56.23%</b>
	$a_1(\times 10^{+7})$	1.018	1.013	0.49%	1.026	-0.78%	1.052	-3.34%
	$a_2(\times 10^{+7})$	1.439	1.433	0.41%	1.451	-0.81%	1.488	-3.40%
	$a_3(\times 10^{+7})$	2.035	2.026	0.42%	2.052	-0.83%	2.104	-3.40%
	$a_4(\times 10^{+7})$	2.878	2.866	0.41%	2.902	-0.84%	2.976	-3.39%
	$a_5(\times 10^{+7})$	4.070	4.053	0.41%	4.105	-0.85%	4.208	-3.38%

#### 4.4. Leakage Detection Using Displacement Error Data

The above multiscale analysis was performed on the pressure data taken in different operating modes, and the wavelet transform showed the best results in detecting various levels of the internal leakage. Although the measurement of the cylinder pressures is common in the area of fluid power systems, some industries do not, however, prefer to utilize pressures sensors on the cylinder

chambers. The measurement of the piston displacement, using the position encoder, is more attractive in some applications such as in aircraft systems. One could take the advantages of the wavelet transform and apply it to displacement error data, obtained from the position encoder, for the internal leakage detection. In this section, the sensitivity of wavelet detailed coefficients of the piston displacement error to various levels of the internal leakage is investigated.

In this round of experiments, a controller, designed in Chapter 5, is employed in the closed-loop system as shown in Figure 4.20, and data of the piston displacement error,  $e_r$ , are obtained in different healthy and faulty operating modes.

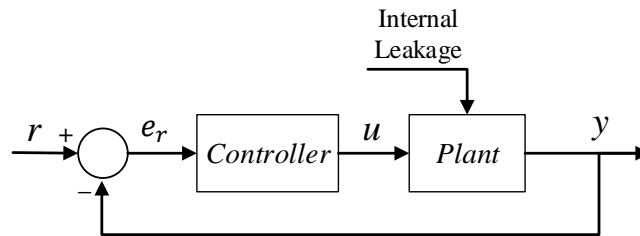


**Figure 4.20** Block diagram of closed-loop positioning system for a hydraulic actuator experiencing internal leakage:  $r$  denotes reference input;  $u$  is control signal;  $e_r$  is displacement error and  $y$  is piston position measured by encoder.

Four operating modes were considered, and three experiments were performed in each operating mode. In all experiments, the actuator was pushing against a spring with stiffness of  $160 \text{ kN/m}$ . Figure 4.21 shows a set of displacement error signals taken from the experimental setup considering step input of  $5 \text{ mm}$  in healthy and faulty operating modes. The operating modes “ $L_1$ ”, “ $L_2$ ” and “ $L_3$ ” correspond to the internal leakage with the flow rate of  $0.59 \text{ L/min}$ ,  $1.25 \text{ L/min}$  and  $1.94 \text{ L/min}$ , respectively. As shown, the magnitude of the error signal grows when the level of the internal leakage increases.

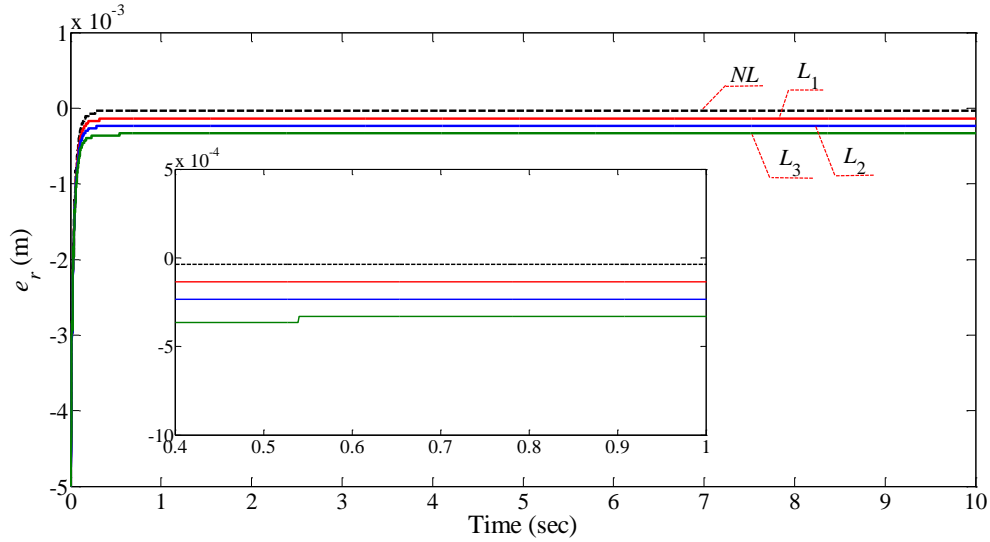


**Figure 4.21** Error signals,  $e_r$ , of healthy and faulty operating modes based on fixed-step reference input of 5 mm. Close-up version shows behavior of error signal over interval [0.4, 1] sec.

Having data of displacement errors of totally twelve experiments (three experiments in each operating modes), the wavelet analysis was performed to find out which wavelet detailed coefficient is sensitive to change in the level of the internal leakage.

Table 4.5 provides the analysis results, based on displacement error data, when the reference input is a constant step of 5 mm. The percentage of changes of faulty values with respect to those of the healthy operating mode is listed in Table 4.6. As illustrated, the more the flow rate of the internal leakage, the higher the percentage of change of the RMS value of  $d_4$  is. Therefore, the detailed coefficient of 4<sup>th</sup> level of decomposition has shown the best sensitivity to change in flow rate of the internal leakage. Other detailed coefficients did not reveal a specific behavior against the increase in the leakage level.

**Table 4.5** Wavelet detailed coefficients of displacement error data obtained from healthy and faulty operating modes. Reference signal is step input of 5 mm.

Operating Mode		Healthy Mode				Faulty Modes											
		No Leakage (NL) ( $\bar{Q}_i = 0.09$ L/min)				$L_1$ ( $\bar{Q}_i = 0.59$ L/min)				$L_2$ ( $\bar{Q}_i = 1.25$ L/min)				$L_3$ ( $\bar{Q}_i = 1.94$ L/min)			
Number of Experiment		Experiment 1	Experiment 2	Experiment 3	Average ( $H$ )	Experiment 1	Experiment 2	Experiment 3	Average ( $F_{L1}$ )	Experiment 1	Experiment 2	Experiment 3	Average ( $F_{L2}$ )	Experiment 1	Experiment 2	Experiment 3	Average ( $F_{L3}$ )
RMS Values	$d_1(\times 10^{-6})$	1.133	1.364	1.189	1.229	1.245	1.183	1.129	1.186	1.209	1.283	1.148	1.213	1.149	1.129	1.084	1.121
	$d_2(\times 10^{-6})$	9.703	7.213	9.433	8.783	7.426	6.861	7.777	7.354	7.659	7.065	7.199	7.308	8.076	9.138	6.828	8.014
	$d_3(\times 10^{-5})$	6.295	6.653	6.402	6.450	6.159	6.336	6.177	6.224	6.311	6.129	6.686	6.376	6.051	6.409	6.050	6.170
	$d_4(\times 10^{-4})$	3.090	2.871	3.065	3.009	2.369	2.652	2.772	2.597	2.401	2.638	2.551	2.530	2.445	2.383	2.516	2.448
	$d_5(\times 10^{-4})$	2.088	2.047	2.081	2.072	1.877	1.951	1.967	1.932	1.886	1.935	1.940	1.920	1.957	1.891	1.986	1.945

**Table 4.6** Percentage of change of average values of wavelet detailed coefficients in faulty modes with respect to those of healthy operating mode. Reference signal is step input of 5 mm.

Operating Mode		Healthy Mode	Faulty Modes					
		NL	$L_1$		$L_2$		$L_3$	
Average Value		$H$	$F_{L1}$	$\delta_{L1}$	$F_{L2}$	$\delta_{L3}$	$F_{L3}$	$\delta_{L3}$
RMS Values	$d_1(\times 10^{-6})$	1.229	1.186	3.49%	1.213	1.25%	1.121	8.79%
	$d_2(\times 10^{-6})$	8.783	7.354	16.26%	7.308	16.79%	8.014	8.75%
	$d_3(\times 10^{-5})$	6.450	6.224	3.51%	6.376	1.15%	6.170	4.34%
	$d_4(\times 10^{-4})$	3.009	2.597	<b>13.69%</b>	2.530	<b>15.92%</b>	2.448	<b>18.64%</b>
	$d_5(\times 10^{-4})$	2.072	1.932	6.77%	1.920	7.32%	1.945	6.13%

The second set of experiments was conducted considering a variable-step reference input. Displacement error data, obtained from seven operating modes, are shown in Figure 4.22. Results of the wavelet analysis on displacement error data and the percentage of changes of faulty values with respect to those of the healthy operating mode are listed in Table 4.7 and Table 4.8, respectively.

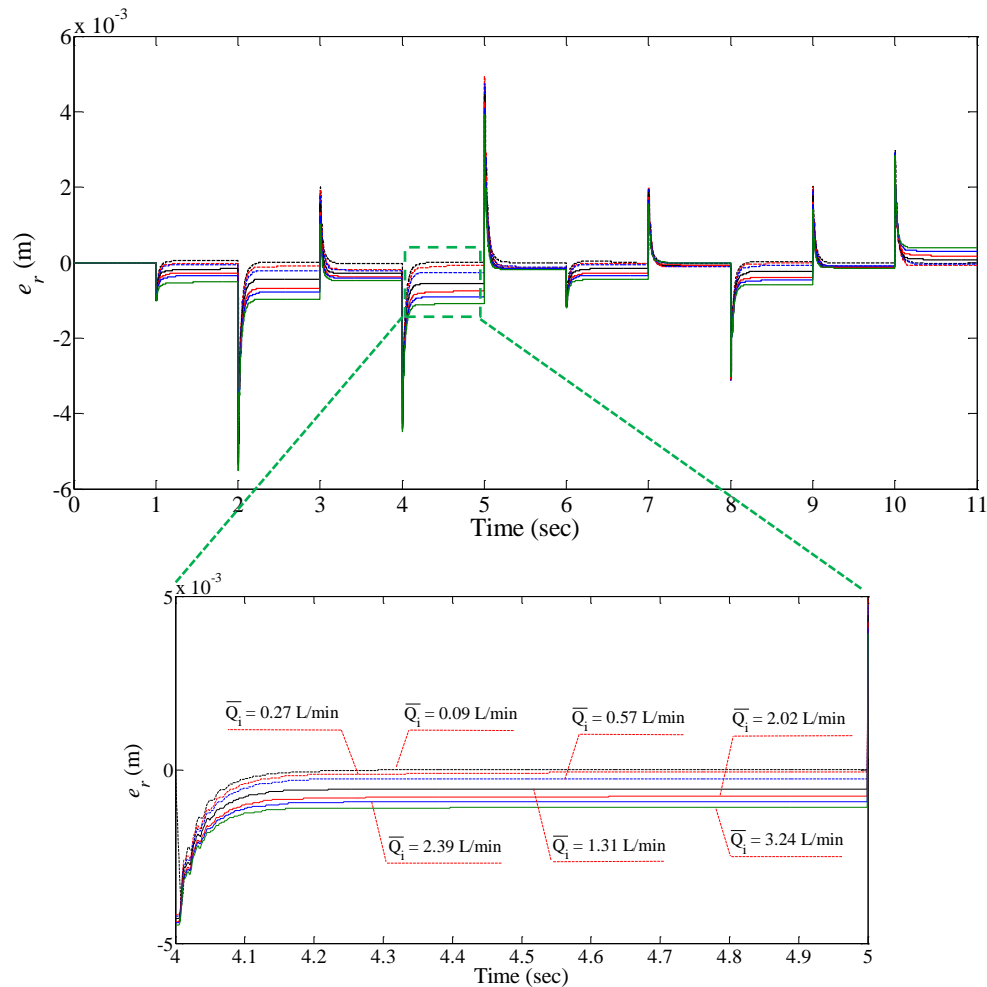


**Figure 4.22** Error signal,  $e_r$ , of seven operating modes considering variable-step input. Average value of internal leakage flow rate varies from almost zero to 3.24 L/min.

Same as the previous results, the 4<sup>th</sup> level of the wavelet detailed coefficients shows a specific behavior to change in the level of the internal leakage. This result will be employed, in Chapter 6, to justify why a set of synthetic errors is proposed to be incorporated into the hydraulic actuator in lieu of emulating the actual internal leakage in the system.

**Table 4.7** Wavelet detailed coefficients of displacement error data obtained from healthy and faulty operating modes. Reference signal is a variable-step input.

Operating Mode		Healthy Mode				Faulty Modes											
		No Leakage (NL) ( $\bar{Q}_i = 0.09 \text{ L/min}$ )				$L_1$ ( $\bar{Q}_i = 0.27 \text{ L/min}$ )				$L_2$ ( $\bar{Q}_i = 0.57 \text{ L/min}$ )				$L_3$ ( $\bar{Q}_i = 1.31 \text{ L/min}$ )			
Number of Experiment		Experiment 1	Experiment 2	Experiment 3	Average (H)	Experiment 1	Experiment 2	Experiment 3	Average (F <sub>L</sub> )	Experiment 1	Experiment 2	Experiment 3	Average (F <sub>L</sub> )	Experiment 1	Experiment 2	Experiment 3	Average (F <sub>L</sub> )
RMS Values	$d_1(\times 10^{-5})$	4.355	4.355	4.355	4.355	4.355	4.356	4.355	4.355	4.354	4.354	4.354	4.354	4.353	4.352	4.355	4.354
	$d_2(\times 10^{-5})$	8.598	8.596	8.596	8.596	8.573	8.575	8.597	8.582	8.567	8.581	8.586	8.578	8.585	8.584	8.578	8.582
	$d_3(\times 10^{-4})$	2.069	2.066	2.086	2.074	2.045	2.079	2.064	2.063	2.049	2.053	2.069	2.057	2.050	2.069	2.072	2.064
	$d_4(\times 10^{-4})$	4.382	4.376	4.368	4.376	4.324	4.323	4.325	4.324	4.315	4.320	4.325	4.320	4.297	4.285	4.299	4.294
	$d_5(\times 10^{-4})$	6.483	6.538	6.494	6.505	6.526	6.452	6.478	6.485	6.578	6.567	6.513	6.552	6.523	6.473	6.482	6.493
Operating Mode						$L_4$ ( $\bar{Q}_i = 2.02 \text{ L/min}$ )				$L_5$ ( $\bar{Q}_i = 2.39 \text{ L/min}$ )				$L_6$ ( $\bar{Q}_i = 3.24 \text{ L/min}$ )			
RMS Values	$d_1(\times 10^{-5})$					4.352	4.352	4.351	4.352	4.351	4.351	4.351	4.351	4.352	4.351	4.351	4.351
	$d_2(\times 10^{-5})$					8.560	8.568	8.559	8.562	8.544	8.538	8.534	8.539	8.536	8.544	8.546	8.542
	$d_3(\times 10^{-4})$					2.069	2.080	2.087	2.079	2.048	2.058	2.061	2.056	2.062	2.064	2.062	2.063
	$d_4(\times 10^{-4})$					4.273	4.276	4.275	4.275	4.263	4.265	4.273	4.267	4.237	4.248	4.257	4.247
	$d_5(\times 10^{-4})$					6.504	6.464	6.449	6.472	6.534	6.519	6.499	6.517	6.541	6.521	6.524	6.529

**Table 4.8** Percentage of change of average values of wavelet detailed coefficients in faulty modes with respect to those of healthy operating mode. Reference signal is a variable-step input.

Operating Mode		Healthy Mode	Faulty Modes					
		NL	$L_1$		$L_2$		$L_3$	
Average Value		H	$F_{L1}$	$\delta_{L1}$	$F_{L2}$	$\delta_{L3}$	$F_{L3}$	$\delta_{L3}$
RMS Values	$d_1(\times 10^{-5})$	4.355	4.355	0.00%	4.354	0.02%	4.354	0.02%
	$d_2(\times 10^{-5})$	8.596	8.582	0.16%	8.578	0.21%	8.582	0.16%
	$d_3(\times 10^{-4})$	2.074	2.063	0.53	2.057	0.82%	2.064	0.48%
	$d_4(\times 10^{-4})$	4.376	4.324	1.19%	4.320	1.28%	4.294	1.87%
	$d_5(\times 10^{-4})$	6.505	6.485	0.31%	6.552	-0.72%	6.493	0.18%
Operating Mode		$L_4$		$L_5$		$L_6$		
Average Value		$F_{L4}$	$\delta_{L4}$	$F_{L5}$	$\delta_{L5}$	$F_{L6}$	$\delta_{L6}$	
RMS Values	$d_1(\times 10^{-5})$	4.352	0.07%	4.351	0.09%	4.351	0.09%	
	$d_2(\times 10^{-5})$	8.562	0.39%	8.539	0.66%	8.542	0.63%	
	$d_3(\times 10^{-4})$	2.079	-0.24%	2.056	0.87%	2.063	0.53%	
	$d_4(\times 10^{-4})$	4.275	2.31%	4.267	2.49%	4.247	2.93%	
	$d_5(\times 10^{-4})$	6.472	0.51%	6.517	-0.18%	6.529	-0.37%	

#### **4.5. Summary**

This chapter presented a procedure for the fault detection using multiscale analysis of experimental data. The procedure was exemplified with detecting the internal leakage fault. The first set of results proved that the experimental data, taken from one of the pressure sensors, were sampled properly, and the pressure signal was stationary and a self-affine fractal. Then, an embedding space was reconstructed based on an optimal lag followed by quantification of five sets of multiscale measures. The measures were obtained in various healthy and faulty operating modes, and the comparisons were performed to find the most reliable multiscale technique in detecting the internal leakage in the hydraulic actuators. Results proved that the wavelet transform is the best technique, among the employed multiscale measures, in the sense of detecting various levels of the internal leakage and the computational time required for calculation of the measures.

The wavelet analysis was then conducted on the displacement error data to investigate the sensitivity of the wavelet detailed coefficients of error data to the change in flow rate of the internal leakage. Based on the experimental results, the fourth level of wavelet detail coefficients showed a specific behavior to various levels of the internal leakage. This observation will be employed for designing a fault-tolerant controller in Chapter 6.

Based on the results of this chapter, the objective (i) was achieved, and the research questions (i) and (ii) were answered.

## CHAPTER 5

# POSITION CONTROLLER DESIGN<sup>1</sup>

This chapter addresses procedure of the controller design using data-driven techniques. For the control structure, a fractional-order PID (FOPID) scheme is used to design a robust position controller. First, the concept of the fractional-order operators is presented followed by their geometrical and physical interpretations. Then, the Oustaloup recursive technique is explained which is used for the realization of fractional-order differentiators and integrators. The structure of the FOPID schemes is compared with the integer-order PID controllers, and the iterative feedback tuning (IFT) technique is employed for tuning control parameters of the FOPID scheme using experimental data. Experiments are conducted to show the robustness of the controller against various system uncertainties as well as its effectiveness in improving the settling time and the sensitivity to the friction effect.

---

1. The content of this chapter is partially published in *IEEE/ASME Trans. on Mechatronics*, Jan. 2019.

### 5.1. Fractional-order Operators

Fractional-order differentiators and integrators are the general version of integer-order ones. In the fractional calculus, the integration and differentiation operators are usually represented by  $J^\alpha$  and  $D^\alpha$ , respectively [44]. Two well-known definitions of  $J^\alpha$  and  $D^\alpha$ , in time domain, are [42]-[44]

$$J^\alpha u(t) = \frac{1}{\Gamma(\alpha)} \int_0^t (t-\tau)^{\alpha-1} u(\tau) d\tau, \quad \alpha > 0 \quad (5.1)$$

$$D^\alpha u(t) = \frac{1}{\Gamma(r-\alpha)} \int_0^t (t-\tau)^{r-\alpha-1} \frac{d^r u(\tau)}{d\tau^r} d\tau, \quad r-1 < \alpha < r \quad (5.2)$$

where  $\Gamma(\cdot)$  denotes the gamma function and is defined as

$$\Gamma(\alpha) = \int_0^\infty e^{-x} x^{\alpha-1} dx \quad ; \quad \alpha \in \mathbb{R} \quad (5.3)$$

If  $\alpha \in \mathbb{N}$ , Eq. (5.3) leads to the definition of the factorial. Therefore, the factorial function is a special case of the gamma function such that

$$\Gamma(z) = (z-1)! \quad ; \quad z \in \mathbb{N} \quad (5.4)$$

In Eqs. (5.1) and (5.2),  $\alpha$  is a positive and real value, and  $r$  is the first integer value greater than  $\alpha$ . In the Fractional Calculus, Eq. (5.1) is so-called the *Riemann-Liouville's* (RL) definition for the fractional-order integration, and Eq. (5.2) is known as the *Caputo's* definition for the fractional-order differentiation.

To evaluate an  $n$ -folded integral of a function  $u(t)$ , Eq. (5.5) is used which is known as the Cauchy's repeated integral equation.

$$J^n u(t) = \int \dots \int_0^t u(\tau) d\tau = \frac{1}{(n-1)!} \int_0^t (t-\tau)^{n-1} u(\tau) d\tau \quad (5.5)$$

Comparing Eq. (5.5) with (5.1), it is seen that the term  $(n-1)!$  has been replaced by  $\Gamma(\alpha)$  to define the fractional-order integral of the function  $u(t)$ . Therefore, the RL definition of integration has been derived from the Cauchy's repeated integral.

With respect to Eq. (5.2), a function requires to be differentiable up to the integer order  $r$  so that a fractional-order differentiation with the order of  $\alpha$  ( $r-1 < \alpha < r$ ) can be defined. This is a limitation of the definition of fractional differentiation proposed by Caputo. Another definition of the fractional-order differentiation is called the RL derivative which is similar to the definition of the RL integration in disguise:

$$D^\alpha u(t) = \frac{1}{\Gamma(r-\alpha)} \frac{d^r}{dt^r} \int_0^t (t-\tau)^{r-\alpha-1} u(\tau) d\tau, \quad \alpha > 0 \quad (5.6)$$

The difference between the Caputo's and RL definitions for the fractional-order differentiation is in the way the integer-order derivative is taken. In the Caputo's definition, the integer derivative of the original function  $u(t)$  is calculated first; then, the convolution of the function derivative and the term  $(t-\tau)^{r-\alpha-1}$  is obtained. In the RL definition, the convolution of the original function and the term  $(t-\tau)^{r-\alpha-1}$  is obtained followed by taking  $r^{th}$  integer derivative of the calculated integral. Another definition of the fractional-order differentiation was developed by Jumarie [97], which is the modified version of the RL definition. According to [97],

$$D^\alpha u(t) = \frac{1}{\Gamma(1-\alpha)} \frac{d}{dt} \int_0^t (t-\tau)^{-\alpha} (u(\tau) - u(0)) d\tau \quad (5.7)$$

The definitions for the fractional operators are not limited to the above-mentioned ones. Extensive explanations on the concept of fractional-order operators have been presented in the literature [42]-[44] and [98].

### 5.1.1. Advantages of Different Definitions of Fractional Operators

Various definitions of the fractional-order operators have their own advantages and limitations. In this section, the merits and disadvantages of the RL, Caputo's and Jumarie definitions are described.

The Riemann-Liouville definition of the fractional-order differentiator is useful for modeling in the viscoelasticity field and the viscoelastic deformation [99]. One of the important advantages of the RL derivative definition is that it does not require the condition of continuity at the origin. It also removes the problem of the singularity at the origin for a number of functions, *e.g.*, the exponential functions [100].

The Caputo's definition is more useful than the RL definition for real-life applications because it employs the integer-order derivatives of the original function, and thus, allows the traditional initial and boundary conditions to be included in the formulations [100]. Moreover, the fractional-order derivative of a constant function is zero according to the Caputo's definition. The most important property of the Caputo's definition is that it realizes the physical interpretation of the fractional-order derivative better than the RL definition, which is discussed in Section 5.1.3.

The Jumarie's definition has removed some limitations of the RL definition. That is why it is known as the modified RL definition of the fractional-order differentiation. It has the advantages

of both the Caputo's and RL definitions as it results in a zero value for the fractional differentiation of a constant function and it works for all non-differentiable functions [98].

### 5.1.2. Disadvantages of Different Definitions of Fractional Operators

The RL derivative of a constant function is not zero which makes the geometric interpretation of the fractional-order derivatives problematic. Additionally, this definition has a singularity at the origin for some functions such as the Mittag-Leffer function which is the generalized version of the exponential function. These disadvantages decrease the usability of this definition in real-life applications [100].

The Caputo's definition requires higher-order differentiability of the original function as it uses the integer derivative of the function inside the integrand [see Eq. (5.2)]. This is a problem as if the first derivative of a function  $u(t)$  does not exist, one cannot use the Caputo's definition for the calculation of a fractional-order derivative  $\alpha$  ( $0 < \alpha < 1$ ) [98].

With respect to the Jumarie's definition, the main problem is that the original function must be continuous at the origin because it uses the term  $u(0)$  in its definition [100]. Therefore, it cannot take the fractional-order derivative of some functions such as  $\ln(t)$ .

### 5.1.3. Geometric and Physical Meanings of Fractional-order Operators

The integer-order derivative and integral operators have established geometric and physical meanings. With respect to the geometric meaning, the first- and second-order derivatives of a function point out the slope and curvature/concavity of the function at a point. Therefore, integer-

order derivatives are local properties of a function and are determined by considering an infinitesimal neighborhood around the point. Based on the Taylor series:

$$f'(t) \approx \frac{f(t+h)-f(t)}{h} \quad (5.8)$$

where  $h$  is the step size or the radius of the neighborhood considered around the point. If  $h \rightarrow 0$ , the limit value will lead to the first derivative of the function. It is seen from Eq. (5.8) that the derivative is obtained from a linear approximation of the function behavior around the point, because the power of the step size  $h$  is not fractional. Therefore, the integer derivative gives a linear approximation of the smooth functions [100]. Smooth functions are the functions that have derivatives of all orders.

From the physical meaning perspective, the integer-order derivatives of a displacement function,  $f(t)$ , recall the meaning of the velocity (*i.e.*,  $\frac{df(t)}{dt}$ , in the time domain, or  $s^1$  in the Laplace domain), acceleration ( $\frac{d^2f(t)}{dt^2}$  or  $s^2$ ), and jerk ( $\frac{d^3f(t)}{dt^3}$  or  $s^3$ ). The concept of the jerk may not be very familiar to everyone. The jerk is the change in the acceleration and is non-zero when a mass is excited by a varying force. If there is a static load applied to a body, the acceleration will not vary, and the jerk will be zero [101].

However, there exists no generally-established physical interpretation for the fractional-order operators. The focus of most of the previous studies has been on the geometric and physical meaning of the fractional-order derivative [100], [102]-[104]; because, the fractional-order integral is, in effect, a fractional-order derivative, in disguise [102]. According to [104], the fractional-order derivative produces the change in the area of the triangle enclosed by the tangent line at a certain point and the vertical line passing through the point and above the  $x$ -axis with respect to

the fractional gradient line. This geometric interpretation has been developed for the polynomial functions only. To propose such an interpretation, the so-called *Euler formulae* has been employed to obtain the fractional derivative of the polynomials as follows

$$D^\alpha[x^\beta] = \frac{\Gamma(\beta+1)}{\Gamma(\beta+1-\alpha)} x^{\beta-\alpha} \quad (5.9)$$

As an example, the fractional derivative of the order 0.5 of the polynomial function  $f(x) = x^3$  is

$$D^{0.5}[x^3] = \frac{\Gamma(4)}{\Gamma(3.5)} x^{2.5} \quad (5.10)$$

By the area formed by the fractional order derivative, one means the triangle ABP shown in Figure 5.1. The angle  $\theta$  generated by the fractional order  $\alpha$  is defined as

$$\theta = \tan^{-1} D^\alpha[x^3] \quad (5.11)$$

Considering  $x = 2$ , the fractional order  $D^{0.5}[x^3]_{|x=2} = 10.2129$ . Therefore  $\theta = 1.4732 \text{ rad}$ .

Tavassoli *et al.* proved that the area of the triangle and the value of the fractional order derivative, for the polynomial functions, are inversely proportional. With respect to Figure 5.1, we have

$$D^\alpha[x^3] \times A_\alpha = \text{constant} \quad (5.12)$$

where  $A_\alpha$  is the area of the triangle ABP. From Eq. (5.12), it is concluded that the fractional order derivative results in the change in the area formed above. The change of the area is a physical property; therefore, the fractional order derivative can be used for measuring the change in the temperature, pressure, divergence and curl [104].

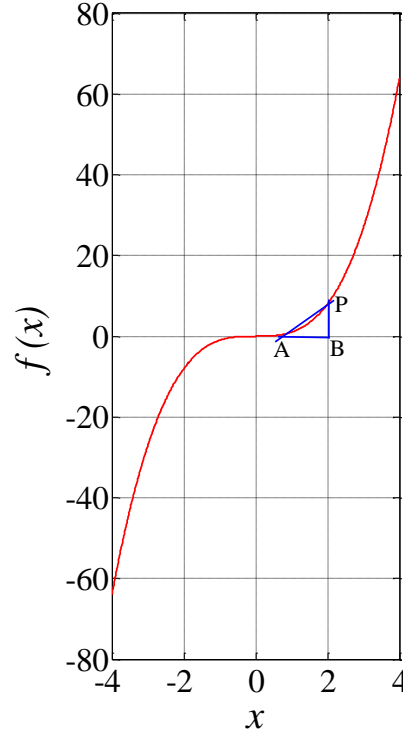


**Figure 5.1** Graph of  $f(x) = x^3$  with triangle generated by fractional order derivative ( $\alpha = 0.5$ ).

Another interpretation of the fractional order derivatives emphasizes the concept of the memory in the dissipative systems. Gomez-Aguilar *et al.* [103] exemplified the memory effect in an RC circuit response. They showed that the behavior of the capacitor discharge can change by formulating the RC circuit with a fractional differential equation. To accomplish this goal, they proposed a new definition of the time constant, in the RC circuits, based on the order of the fractional derivative. According to Kirchhoff's law, the conventional differential equation of an RC circuit is

$$R \frac{dq(t)}{dt} + \frac{1}{C} q(t) = v(t) \quad (5.13)$$

where  $q(t)$  is the charge;  $R$  and  $C$  are the resistance and capacitance and  $v(t)$  is the voltage source.

With respect to Eq. (5.13), the time constant is defined as  $\tau = RC$ . Assuming a step input for the

voltage source with the amplitude  $V_0$  [i.e.,  $v(t) = V_0 u(t)$ ], the time domain behavior of the charge is

$$q(t) = CV_0(1 - e^{-t/\tau}) \quad (5.14)$$

On the other hand, the fractional differential equation version of the RC circuit has the form

$$R \frac{d^\alpha q(t)}{dt^\alpha} + (\sigma^{1-\alpha}) \frac{1}{C} q(t) = (\sigma^{1-\alpha}) v(t) \quad (5.15)$$

where  $\alpha$  is the order of the fractional derivative and  $\sigma$  is a new parameter defined to keep the consistency with the dimensionality [103]. Therefore, the dimension of  $\sigma$  is *second*, i.e.,  $[\sigma] = \text{sec}$ . Having the parameter  $\sigma$ , the new time constant of Eq. (5.15) is defined as

$$\tau_\alpha = \frac{RC}{\sigma^{1-\alpha}} \quad (5.16)$$

It is seen that the time constant  $\tau_\alpha$  leads to the conventional definition ( $\tau = RC$ ) when  $\alpha = 1$ .

Considering Eq. (5.16), the charge behavior will be

$$q(t) = CV_0 \left[ 1 - E_\alpha \left( -\frac{t^\alpha}{\tau_\alpha} \right) \right] \quad (5.17)$$

where  $E_\alpha(\cdot)$  is the Mittag-Leffler function and is defined as

$$E_\alpha(t) = \sum_{m=0}^{\infty} \frac{t^m}{\Gamma(\alpha m + 1)} \quad (5.18)$$

In Eq. (5.18), if  $\alpha = 1$ ,  $E_1$  is an exponential function. Therefore, the Mittag-Leffler function is the generalization of the exponential function. In [103], it is proven that the behavior of the capacitor charge,  $q(t)$ , changes when the order of the fractional derivative varies. This change is in the sense of both the time constant and the steady-state value. According to Eq. (5.17), when the order of the fractional derivative decreases, the steady-state value of the charge reduces as well. Moreover,

the time constant corresponding to that steady state value decreases which leads to a faster transient response. Therefore, the fractional derivative can play an important role in both dissipating the value of the charge as well as changing the time constant. This behavior is equivalent to at what extent the memory of the system is employed by using the fractional derivative [103]. When the order of the derivative is equal to 1, the whole memory of the system has been lost. The loss of the memory means that only the local behavior of the function in an infinitesimal neighborhood of the point is considered which is equivalent to the conventional interpretation of the first order derivative. On the other hand, if  $\alpha$  tends to zero, the charge of the capacitor approaches zero at all times, *i.e.*,  $q(t) = 0$ , which means that the initial value of the function is considered at all times. The reason behind  $q(t) = 0$ , is that the initial value of the capacitor charge is zero. Consequently, the fractional order differentiation  $\alpha$  ( $0 < \alpha < 1$ ), may imply capturing the memory partially which affects the time constant and the steady state value of the capacitor charge.

An interesting interpretation of the fractional-order operators has been developed in [102] which deals with the concept of lost and preserved memory of a dynamic system. Let's start with the concept of the memory in the form of the integral. As known, the integer-order integral of a function  $f(t)$  is defined as the convolution of the function and a unit step function as follows

$$J^1 f(t) = (u * f)(t) = \int_0^t \underbrace{u(t-\tau)}_{=1} f(\tau) d\tau = \int_0^t f(\tau) d\tau \quad (5.19)$$

where  $J^1$  is the first-order integral operator and  $u(t)$  denotes the unit step function. The unit step function is, in fact, the impulse response of a function so-called  $h_\alpha$ , that is defined as follows [102]

$$h_\alpha(t) = \frac{t^{\alpha-1}}{\Gamma(\alpha)} \quad (5.20)$$

In Eq. (5.20), if  $\alpha = 1$ , then  $h_1(t) = \frac{t^0}{\Gamma(1)} = 1 = u(t)$ . Using this function, we can generalize the integer-order integral to the fractional-order one based on the RL definition; therefore,

$$J^\alpha f(t) = (h_\alpha * f)(t) = \frac{1}{\Gamma(\alpha)} \int_0^t (t - \tau)^{\alpha-1} f(\tau) d\tau \quad (5.21)$$

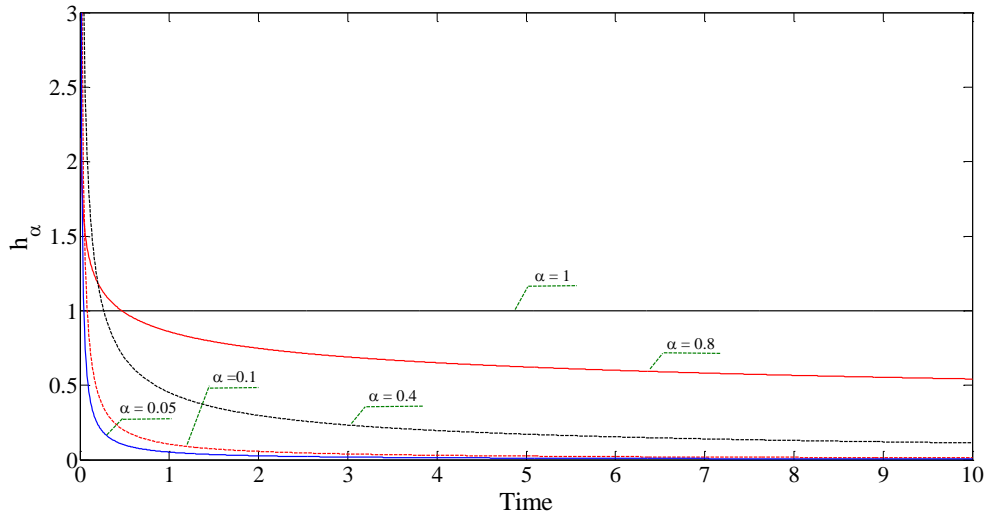


**Figure 5.2** Behavior of function  $h_\alpha(t)$  for various values of  $\alpha$ .

With respect to Figure 5.2, when  $\alpha$  tends to zero, the function  $h_\alpha(t)$  converges to the one-sided impulse function, *i.e.*,  $h_{\alpha=0}(t) = \delta(t)$ . Therefore,

$$J^{\alpha=0} f(t) = (h_{\alpha=0} * f)(t) = (\delta * f)(t) = \int_0^t \delta(t - \tau) f(\tau) d\tau = f(t) \quad (5.22)$$

As known, a unit step function  $u(t)$  corresponds to a filter whose impulse response has a perfect memory [see Eq. (5.19)]. Perfect memory means that it captures the whole history of the function during the time evolution of the system. On the other hand, the delta function,  $\delta(t)$ , plays the role

of a filter with no memory [see Eq. (5.22)]. As illustrated in Figure 5.2, the function  $h_\alpha$  varies between the unit step and delta functions based on the value of  $\alpha$ . Therefore,  $h_\alpha$  plays the role of a filter which captures the history of the function partially by accumulating the memory preserved proportional to the order  $\alpha$ . One property of this function is that it is a self-similar function meaning that it is invariant under a linear scale change in time [102], because,

$$h_\alpha(kt) = \frac{(kt)^{\alpha-1}}{\Gamma(\alpha)} = k^{\alpha-1} \frac{t^{\alpha-1}}{\Gamma(\alpha)} = k^{\alpha-1} h_\alpha(t) \quad (5.23)$$

The self-similarity property can be observed in Figure 5.2, when the value of the function  $h_\alpha$  changes over time for each value of  $\alpha$  ( $0 < \alpha < 1$ ). Considering Eqs. (5.19) to (5.23), it is concluded that the function  $h_\alpha$ , incorporated into the definition of the fractional-order integral, mitigates the effect of the history such that the process of capturing the history of the function decays in a self-similar manner [102]. In other words, the present value of the function is given a maximum weight and the past states features the weights that decrease at a rate proportional to the order of the integration [102].

The Caputo's definition of fractional-order derivative considering the order  $\alpha$  ( $0 < \alpha < 1$ ) is

$$D^\alpha f(t) = \frac{1}{\Gamma(1-\alpha)} \int_0^t (t-\tau)^{-\alpha} \frac{df(\tau)}{d\tau} d\tau, \quad 0 < \alpha < 1 \quad (5.24)$$

Choosing  $\beta = 1 - \alpha$ , Eq. (5.24) is rewritten as

$$D^\alpha f(t) = \frac{1}{\Gamma(\beta)} \int_0^t (t-\tau)^{\beta-1} \frac{df(\tau)}{d\tau} d\tau, \quad 0 < \alpha < 1 \quad (5.25)$$

where the right-hand side (RHS) of Eq. (5.25) is, in fact, the fractional-order integral of the function  $\frac{df(t)}{dt}$  with the order  $\beta$ . Comparing Eq. (5.25) with Eq. (5.21), it can be concluded that the

$\alpha^{th}$  fractional differentiation of a function  $f(t)$  is equivalent to  $(1 - \alpha)$ -folded integration of its first-order derivative [*i.e.*,  $\dot{f}(t)$ ]. If  $\alpha = 1$ , then  $\beta = 0$ , and the function  $h_\beta$  converges to the delta function “with no memory” for  $\dot{f}(t)$ . therefore,

$$D^{\alpha=1}f(t) = \int_0^t \delta(t - \tau) \frac{df(\tau)}{d\tau} d\tau = \frac{df(t)}{dt} \quad (5.26)$$

leading to the conventional first-order derivative. This conclusion seems correct as the function  $\dot{f}(t)$  does not deal with the past history and plays the role of the future predictor for the function  $f(t)$ . In contrast, if  $\alpha = 0$ , then  $\beta = 1$ , and the function  $h_\beta$  becomes a unit step function “with perfect memory” for  $\dot{f}(t)$  resulting in the function  $f(t)$  as follows

$$D^{\alpha=0}f(t) = \int_0^t \underbrace{u(t - \tau)}_{=1} \frac{df(\tau)}{d\tau} d\tau = \int_0^t df(\tau) = f(t) \quad (5.27)$$

According to Eq. (5.27), the convolution of the step input and  $\dot{f}(t)$  results in the function  $f(t)$ . Considering the definition of the memory for the original function  $f(t)$  only, we can conclude that the perfect memory for  $\dot{f}(t)$  means no memory for  $f(t)$ . In other words, the function  $h_\beta$  used for  $\dot{f}(t)$  deals with the lost memory of the original function  $f(t)$ . Using the concept of the lost memory, one may conclude that the fractional-order differentiation accumulates the lost memory of the original function such that the order  $\alpha = 0$  means no lost memory is accumulated, while  $\alpha = 1$  leads to the accumulation of the whole history of the lost memory. The lost and preserved memories of a system have analogies in the real applications [102]. Consider a mass-spring-damper system. The spring stores/preserves the input energy while the damper dissipates/loses the energy. The total energy of this system comprises a term including the displacement and one term including the velocity. As shown above, the fractional-order integrator operates on the input

function, and the fractional-order differentiation deals with the first order derivative of the input function [102].

The interpretation of the fractional-order operators deserves more discussions as there is no unique definition and interpretation on their physical meaning. From our point of view, the fractional-order differentiators may allow one to investigate the behavior of the function around a point from a different perspective; that is, unlike the integer derivatives, the fractional derivatives give a nonlinear approximation of the function behavior around a point. This nonlinearity can be in the form of a power-law approximation which conducts one to study the behavior of the dynamical systems. Dynamical systems are a type of dynamic systems that exhibit chaotic behavior where the chaos means a specific state in which a system behaves unpredictably [100]. As indicated earlier, the first order derivative plays the role of a predictor based on a linear approximation of the function behavior. The integer derivative is enough for predicting the behavior of the deterministic and non-chaotic systems, because the behavior of a non-chaotic system is not sensitive to the initial condition of the system, and the system behavior can be predicted even if the initial condition changes reasonably. On the other hand, the chaotic systems are highly sensitive to the initial conditions meaning that if the initial condition changes in a very small range, the behavior of system states changes considerably; however, it does not mean that the chaotic systems are completely unpredictable. For such systems, there is a horizon of predictability. Due to high sensitivity of the chaotic systems to the initial conditions, the integer-order derivatives (*i.e.*, linear approximations of the system behavior) are not useful tools for the prediction of the next states of such system. Therefore, there must exist a tool for determining this horizon of predictability. Based on the above explanations, the fractional-order derivatives may be able to play the role of an indicator in determining at what extent the behavior of a chaotic system

is predictable. Therefore, the application of the integer derivatives can be confined to the prediction of the non-chaotic systems while the fractional-order differentiators can be used for partial prediction of the behavior of chaotic systems. Nurturing this idea requires an extensive study which is a part of the future work.

## 5.2. Approximation of Fractional-order Operators in Laplace Domain

Figure 5.3 shows the graphical summary of fractional-order and integer-order differentiators and integrators in the Laplace domain.

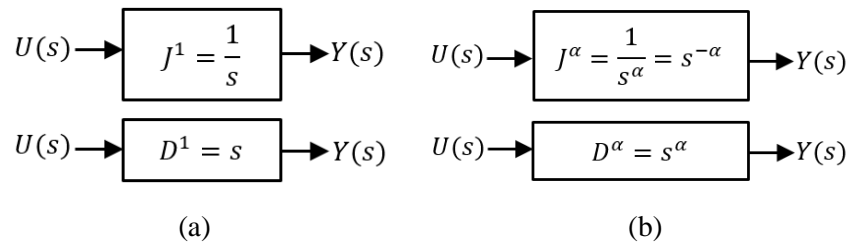


**Figure 5.3** Integration and differentiation operators in Laplace domain: (a) first-order integer operator; (b) fractional-order operator;  $\alpha$  is a non-integer value.

In the field of Control Engineering, the expression of the fractional-order operators in the Laplace domain is required. Many efforts have been performed to find realizable forms of the fractional-order derivative and integral terms in the  $s$ -domain. The fractional-order operators are infinite dimensional filters which are not realizable in practice. To approximate such filters with the equivalent finite dimensional transfer functions, a useful technique developed by Oustaloup *et al.* [45] has been employed. The Oustaloup technique proposes a realization form for the non-

integer operators based on a recursive distribution of real zeros and poles [45]. According to [45], the output of a non-integer differentiator, in time domain, can be expressed generally as

$$y(t) = \tau^\alpha \left( \frac{d}{dt} \right)^\alpha u(t) \quad (5.28)$$

where  $\tau$  is a real and positive time constant. The translation of Eq. (5.28) in  $s$ -domain is

$$Y(s) = \left( \frac{s}{\omega_u} \right)^\alpha U(s) \quad (5.29)$$

In (5.29),  $\omega_u$  is called the unit frequency gain, and  $\omega_u = \frac{1}{\tau}$ . Based on Eq. (5.29), the non-integer order transmittance  $D(s)$  is defined as

$$D(s) = \left( \frac{s}{\omega_u} \right)^\alpha \quad (5.30)$$

To cut-off both high and low frequencies, the differentiation transfer function  $\frac{s}{\omega_u}$  can be limited to a given frequency range  $[\omega_A, \omega_B]$ , and is replaced by the following frequency-bounded differentiation transfer function

$$\frac{s}{\omega_u} \cong C_0 \frac{1 + s/\omega_b}{1 + s/\omega_h} \quad (5.31)$$

such that,

$$\begin{cases} \omega_u = (\omega_b \cdot \omega_h)^{0.5} \\ C_0 = \frac{\omega_b}{\omega_u} = \frac{\omega_u}{\omega_h} \end{cases} \quad (5.32)$$

where  $\omega_b$  and  $\omega_h$  denote the low- and high-transitional frequencies such that:

$$\begin{cases} \omega_b \leq \omega_A \\ \omega_h \geq \omega_B \end{cases} \quad (5.33)$$

Combining Eqs. (5.30) - (5.33), the fractional-order transmittance  $D(s)$  is expressed as

$$D(s) = \left(\frac{\omega_u}{\omega_h}\right)^\alpha \left(\frac{1 + s/\omega_b}{1 + s/\omega_h}\right)^\alpha \quad (5.34)$$

To approximate  $D(s)$  by an integer-order transfer function, a recursive distribution of real poles and zeros is used such that

$$D(s) = \lim_{M' \rightarrow \infty} D_{M'}(s) \quad (5.35)$$

and,

$$D_{M'}(s) = \left(\frac{\omega_u}{\omega_h}\right)^\alpha \prod_{k=-M'}^{M'} \frac{1 + s/\acute{\omega}_k}{1 + s/\omega_k} \quad (5.36)$$

where  $\acute{\omega}_k$  and  $\omega_k$  are defined as

$$\acute{\omega}_k = \omega_b \left(\frac{\omega_h}{\omega_b}\right)^{\left[\frac{k+M'+0.5-\frac{\alpha}{2}}{2M'+1}\right]} \quad (5.37)$$

$$\omega_k = \omega_b \left(\frac{\omega_h}{\omega_b}\right)^{\left[\frac{k+M'+0.5+\frac{\alpha}{2}}{2M'+1}\right]} \quad (5.38)$$

Selection of  $M'$  leads to the determination of  $D_{M'}(s)$  from (5.36), which is an integer-order transfer function approximating the fractional-order differentiator  $D(s) = \left(\frac{s}{\omega_u}\right)^\alpha$ . Note that  $D_{M'}(s)$  consists of  $2M' + 1$  numbers of zeros or poles. According to [45], the order of the fractional operator can be any real value either positive or negative ( $\alpha \in \mathbb{R}$ ). To find the approximation of a non-integer integrator, the fractional order  $\alpha$ , in Eqs. (5.29) to (5.38), possesses the negative value.

The fractional-order differentiators are less sensitive to the high frequency noise as compared to the integer-order one. As known, the integer-order differentiator (*i.e.*,  $Y(s) = k_d s$ ) plays the

role of a linear filter in the frequency domain (*i.e.*,  $Y(\omega) = k_d \times j\omega$ ). The reason behind the sensitivity of the integer-order differentiator to the noise is that it amplifies the magnitude when the frequency increases. The greater value of the derivative gain  $k_d$  leads to the higher magnitude of the filter output in high frequencies. However, the non-integer differentiators do not follow this pattern as they constitute a plateau after middle frequencies. If the order of the differentiator  $\alpha$  decreases, the magnitude reduces as well. The Bode magnitude of  $s^\alpha$  is shown in Figure 5.4 for various values of  $\alpha$ . Referring to Figure 5.4, the magnitude reduces and a plateau is constituted at earlier frequencies when the order of the differentiator (*i.e.*, " $\alpha$ " in  $Y(s) = s^\alpha$ ) decreases. Therefore, the fractional-order differentiators amplify the magnitude of the high frequency noise much less as compared to the integer-order one. For instance, the amplitudes of the frequency response of integer order ( $s^1$ ) and fractional order ( $s^{0.17}$ ) differentiators equal 500 and 2.87, at  $\omega = 500$  rad/sec, respectively.

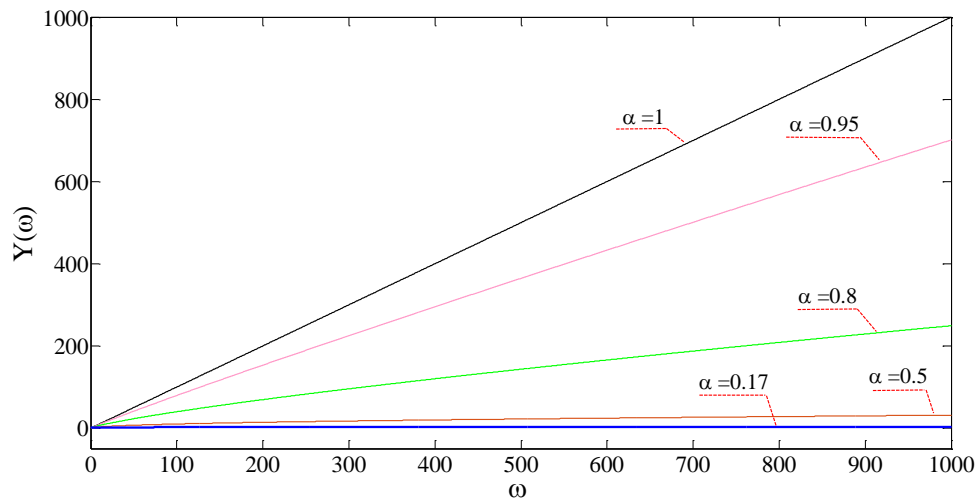


**Figure 5.4** Bode plot of  $s^\alpha$  for various values of  $\alpha$  between 0 and 1.

### 5.3. Fractional-order PID Controllers

The family of integer-order PID controllers is a well-known type of linear controllers used in many industrial applications. In the conventional PID schemes, each proportional, derivative and integral gains plays a specific role in controlling a system. For example, a proportional gain is used to reduce the rise time and decrease the steady state error. A derivative gain is useful for enhancing the stability and reducing the overshoot; however, it amplifies the high frequency noise and does not affect the steady-state error. Furthermore, the integral gain is utilized to eliminate the steady state error but makes the transient response worse. The FOPID schemes have been introduced to improve the overall performance of the system compared to the conventional PID controllers. The overall structure of an FOPID controller is given by

$$C_{FOPID} = K_P + K_i s^{-\lambda} + K_d s^\mu \quad (5.39)$$

It is seen that there are two more tuning parameters in FOPID controllers (*i.e.*,  $PI^\lambda D^\mu$ ) than in PID schemes.  $\lambda$  and  $\mu$  are positive and real numbers and are added to the conventional PID controllers to make a compromise between the pros and cons of the integral and derivative parts, respectively. In other words,  $\lambda$  and  $\mu$  enhance the performance of the controller and make the controller design more flexible [42].

### 5.4. Controller Parameters Tuning

There are various methods to tune the controller parameters in PID and FOPID controllers [50]-[55]. Most of these methods tune the controller parameters using a mathematical model of the system and system parameters. Since this study is on design of a position controller using experimental data, the iterative feedback tuning technique [55] is chosen to tune five parameters

of the FOPID controller. The IFT is a data-driven parameter tuning technique that is applicable to both model-based and data-driven physical systems. The control parameters of a FOPID scheme are defined as

$$\vec{\rho} = [\rho_1, \rho_2, \rho_3, \rho_4, \rho_5]^T = [K_p, K_i, K_d, \lambda, \mu]^T \quad (5.40)$$

In order to find a set of optimum values for the vector  $\vec{\rho}$ , an objective function must be minimized. The explicit solution for such optimization problem requires a knowledge on the plant and disturbances because the solutions need iterative gradient-based minimization procedures, and the gradient term of the criterion includes a fairly complicated function of the plant and disturbance dynamics [55]. This is why most of tuning methods are model-based and require an accurate or estimated model of a dynamic system. The IFT was developed aiming to tune the control parameters based on the input-output experimental data taken from physical systems. Consider a one degree-of-freedom control system for the plant  $P$ . With respect to Figure 5.5, the error and control signals are given by [55]

$$e = r - y = \left(1 - \frac{CP}{1 + CP}\right)r - \frac{1}{1 + CP}v \quad (5.41)$$

$$u = C(r - y) \quad (5.42)$$

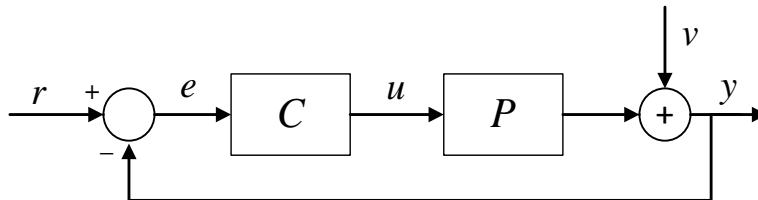


**Figure 5.5** Block diagram of control system:  $C$  is controller;  $r$  denotes reference signal;  $u$  is control signal;  $v$  represents output disturbance applied to output  $y$ .

The primary objective function is defined as [55]

$$J_P(\rho_i) = \frac{1}{2N} E \left[ \sum_{k=1}^N \{ \alpha_y [L_y \tilde{y}_k(\rho_i)]^2 + \alpha_u [L_u u_k(\rho_i)]^2 \} \right] \quad (5.43)$$

where  $E[\cdot]$  denotes the expectation with respect to the disturbance  $v$ ;  $k$  is the number of each data point acquired from the experimental setup, and  $N$  is the total number of data points in each experiment; the subscript  $i$  denotes the number of the iteration in the optimization algorithm. The objective function,  $J_P$ , is the performance index which contains two terms: (i) the first term is related to the tracking error between the desired response and the actual output of the system, and (ii) the second one is the penalty on the control effort. There are two weights  $\alpha_y$  and  $\alpha_u$  indicating the weight of each criterion in the performance index. The frequency weighted filters  $L_y$  and  $L_u$  are used when specific frequency bands, in the response of the closed-loop system, are of concern. The second criterion is used when the control signal exceeds the saturation levels. As the control signal does not exceed the maximum and minimum threshold values in the hydraulic actuation system under study, there is no need to use this criterion in the final objective function.

Typically, the objective function of Eq. (5.43) containing only the tracking criterion is used for the optimization problems. In order to consider the concept of the robust stability as a criterion, the following term is added [105]

$$J_R(\rho_i) = \frac{1}{2N} E \left[ \sum_{k=1}^N \{ \alpha_s [L_S C_k^{-1}(\rho_i) u_k(\rho_i)]^2 \} \right] \quad (5.44)$$

where  $J_R$  denotes the robustness index, and  $\alpha_s$  is a positive value indicating the weight;  $L_S$  is referred to as a stable and proper weighting filter to impose some specific sensitivity attenuations [105]. In this study, a combination of Eqs. (5.43) and (5.44) is considered, for the optimization problem, to minimize both tracking and robust stability criteria. In addition, the filters  $L_y$  and  $L_S$

are set to 1. The overall objective function, used in this part of study, is defined as

$$J(\rho_i) = \frac{1}{2N} E \left[ \sum_{k=1}^N \{ \alpha_y [\tilde{y}_k(\rho_i)]^2 + \alpha_s [C_k^{-1}(\rho_i) u_k(\rho_i)]^2 \} \right] \quad (5.45)$$

The objective of the criteria, in Eq. (5.45) is to tune the control parameters  $\vec{\rho}$  such that  $J(\rho)$  is minimized. The optimum vector  $\vec{\rho}$  is defined by

$$\rho^* = \arg \min_{\rho} J(\rho) \quad (5.46)$$

To obtain a minimum of  $J(\rho)$ , a solution for the following equation must be found:

$$\frac{\partial J(\rho)}{\partial \rho} = \frac{1}{N} E \left[ \sum_{k=1}^N \left\{ \alpha_y \tilde{y}_k(\rho) \frac{\partial \tilde{y}_k(\rho)}{\partial \rho} + \alpha_s [C_k^{-1}(\rho) u_k(\rho)] \left( \frac{\partial C_k^{-1}(\rho)}{\partial \rho} u_k(\rho) + C_k^{-1}(\rho) \frac{\partial u_k(\rho)}{\partial \rho} \right) \right\} \right] = 0 \quad (5.47)$$

where the gradients  $\frac{\partial \tilde{y}(\rho)}{\partial \rho}$  and  $\frac{\partial u(\rho)}{\partial \rho}$  include the nuisance signal  $v$  and the transfer function of the

plant. According to the IFT technique, there is no need to have a prior knowledge about the system

parameters and/or the model of the plant, and the gradient  $\frac{\partial J(\rho)}{\partial \rho}$  is quantified by performing two

experiments in each iteration  $i$  of the optimization procedure. In order to calculate this gradient,

some terms must be obtained from the experiments including: (i) the signals  $\tilde{y}(\rho)$  and  $u(\rho)$ , and

(ii) the gradients  $\frac{\partial \tilde{y}(\rho)}{\partial \rho}$  and  $\frac{\partial u(\rho)}{\partial \rho}$ . Note that  $\frac{\partial \tilde{y}(\rho)}{\partial \rho} = \frac{\partial y(\rho)}{\partial \rho}$ , because we define  $\tilde{y} = y - r$ . The

unbiased estimates of the gradients  $\frac{\partial \tilde{y}(\rho)}{\partial \rho}$  and  $\frac{\partial u(\rho)}{\partial \rho}$  are found by following the IFT procedure.

Based on the IFT, the unbiased estimates can be used instead of the expectation values of the

original gradients [55]. The unbiased estimate of the gradient  $\frac{\partial J(\rho)}{\partial \rho}$  (i.e.,  $est \left[ \frac{\partial J(\rho)}{\partial \rho} \right]$ ) is calculated,

based on the given objective function, as follows

$$est \left[ \frac{\partial J(\rho)}{\partial \rho} \right] = \frac{1}{N} \sum_{k=1}^N \left\{ \alpha_y \tilde{y}_k(\rho) est \left[ \frac{\partial y_k(\rho)}{\partial \rho} \right] + \alpha_s [C_k^{-1}(\rho) u_k(\rho)] \left( \frac{\partial C_k^{-1}(\rho)}{\partial \rho} u_k(\rho) + C_k^{-1}(\rho) est \left[ \frac{\partial u_k(\rho)}{\partial \rho} \right] \right) \right\} \quad (5.48)$$

Table 5.1 provides the procedure of conducting two experiments and storing the data for further steps in the IFT technique. The first experiment is a regular one considering the original reference input for the piston displacement. The second experiment is so-called “special” experiment because the reference input differs from the one used in the first experiment. In the special experiment, data of the position encoder stored in the first experiment (*i.e.*,  $y_i^1$ ) are subtracted from the original reference input, and the result is considered as the new reference input. The superscript used in  $r$ ,  $u$  and  $y$  is the experiment number, and the subscript  $i$  denotes the number of iteration in the optimization procedure.

**Table 5.1** Experiments required to obtain gradient of objective function based on IFT technique.

Experiment No.	Reference Signal	Control Signal	Output Signal
# 1 (Regular)	$r_i^1 = r$ (original reference input)	$u_i^1$	$y_i^1$
# 2 (Special)	$r_i^2 = r - y_i^1$	$u_i^2$	$y_i^2$

With respect to Table 5.1, data of  $r^1$ ,  $u^1$ ,  $y^1$ ,  $u^2$  and  $y^2$  are employed to quantify the estimates of gradients of  $y$  and  $u$  with respect to each control parameter [55]

$$\begin{cases} \tilde{y} = y^1 - r^1 & ; \quad est \left[ \frac{\partial y(\rho)}{\partial \rho} \right] = C^{-1} \frac{\partial C}{\partial \rho} y^2 \\ u = u^1 & ; \quad est \left[ \frac{\partial u(\rho)}{\partial \rho} \right] = C^{-1} \frac{\partial C}{\partial \rho} u^2 \end{cases} \quad (5.49)$$

The terms  $C^{-1}$ ,  $\frac{\partial C}{\partial \rho}$  and  $\frac{\partial C^{-1}}{\partial \rho}$ , used in Eqs. (5.48) and (5.49), play the role of filters in the Laplace domain, and are obtained from Eq. (5.39). By obtaining the gradients with respect to each control parameter,  $est\left\{\frac{\partial y(\rho)}{\partial \rho}\right\}$  and  $est\left\{\frac{\partial u(\rho)}{\partial \rho}\right\}$  are used, in Eq. (5.48), to find the value of  $est\left[\frac{\partial J(\rho)}{\partial \rho}\right]$  in each iteration  $i$ . Then, the controller parameters are updated according to the following equation:

$$\rho_{i+1} = \rho_i - \gamma_i R_i^{-1}(\rho_i) \text{est} \left[ \frac{\partial J}{\partial \rho}(\rho_i) \right] \quad (5.50)$$

where  $\gamma_i$  is the step size with a positive real value. The choice of the step size depends on the convergence rate of the objective function. For some optimization problems, one may need to update the step size according to some update strategies, *e.g.*, the Levenberg-Marquardt strategy [106]. In this study,  $\gamma_i = 1$  was good enough to achieve a fast convergence of the objective function. If a constant value of  $\gamma_i$  does not converge the optimization algorithm, the other choice can be  $\gamma_i = l/i$ , where  $l$  is a positive constant value (*e.g.*,  $l = 1$ ), and  $i$  is the iteration number. In Eq. (5.50),  $R_i$  is a positive definite matrix that is updated in each iteration  $i$ . A choice for  $R_i$  is given by [55]

$$R_i(\rho_i) = \frac{1}{N} \sum_{k=1}^N \left\{ \alpha_y \text{est} \left[ \frac{\partial y_k}{\partial \rho}(\rho_i) \right] \text{est} \left[ \frac{\partial y_k}{\partial \rho}(\rho_i) \right]^T + \alpha_s \left( \frac{1}{C} \text{est} \left[ \frac{\partial u_k}{\partial \rho}(\rho_i) \right] \right) \left( \frac{1}{C} \text{est} \left[ \frac{\partial u_k}{\partial \rho}(\rho_i) \right]^T \right) \right\} \quad (5.51)$$

Finally, the new value of objective function is calculated using the Taylor series expansion [55]

$$J(\rho_{i+1}) \cong J(\rho_i) - \gamma_i \text{est} \left[ \frac{\partial J}{\partial \rho}(\rho_i) \right]^T R_i^{-1}(\rho_i) \text{est} \left[ \frac{\partial J}{\partial \rho}(\rho_i) \right] \quad (5.52)$$

## 5.5. Design Procedure

Figure 5.6 describes the main steps to be followed in order to design a robust position controller for the hydraulic actuation system presented in Figure 3.1. The first step is to consider initial values for the controller parameters. The FOPID structure is then approximated using the Oustaloup technique. In the third step of the design procedure, two experiments are performed and data of the piston displacement and control signals, from both experiments, are obtained. The data are then used to determine the estimated gradients based on the IFT technique. Finally, the updated

controller parameters and the value of the objective function are quantified. If the new parameters do not minimize the objective function, another set of experiments are performed and the procedure shown in Figure 5.6 is repeated until the objective function is minimized.

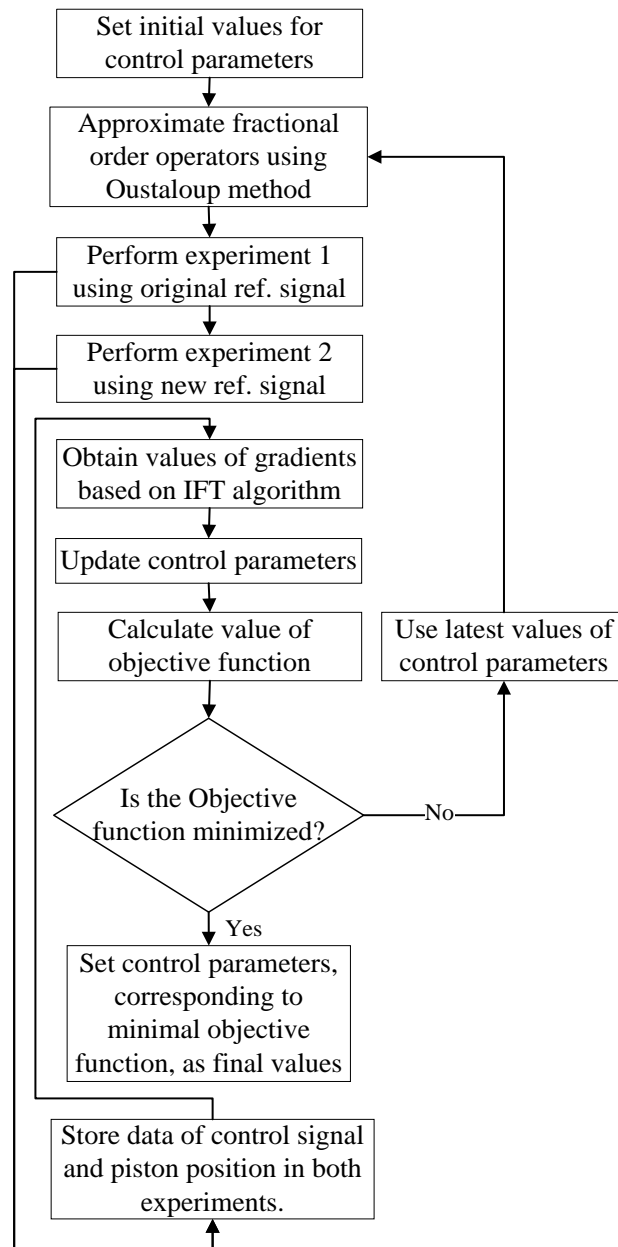


**Figure 5.6** Steps of FOPID controller design based on Oustaloup and IFT techniques.

## 5.6. Results and Discussion

The following points were considered to design an FOPID-based position controller:

(i) The IFT technique was found not much sensitive to the initial values of control parameters for the available hydraulic system. It was enough to choose  $K_d$  greater than  $K_p$  and  $K_i$  in a reasonable range. Also,  $\lambda$  close to 1 highlighted the drawbacks of the integer-order integrator. Regarding the parameter  $\mu$ , an effort was done to design a simpler controller without the derivative term (*i.e.*, FOPI); however, the FOPI controller created overshoot which was not desirable. Therefore, a small gain of  $\mu$  was chosen to overcome the effect of the integral and proportional gains in creating the overshoot. Based on the above observations, initial values for the control parameters, in the first iteration, were set to

$$\rho_{initial} = [K_p, K_i, K_d, \lambda, \mu]^T = [35, 45, 55, 0.65, 0.25]^T \quad (5.53)$$

(ii) In order to consider effect of the robust stability criterion, various values of the weight  $\alpha_s$ , were tested in the objective function [Eq. (5.45)]. Finally,  $\alpha_s = 0.02$  was found as a good choice that minimized the objective function and created good tracking response. If  $\alpha_s = 0.1$  or  $0.2$ , for example, the final value of the integral gain  $K_i$  increases dramatically and causes the fluctuations in tracking the desired response. Also,  $\alpha_y$  was set to one [55].

(iii) The parameter  $M'$ , used in the Oustaloup recursive technique, was set to 2 in order to approximate the fractional-order differentiators and integrators. In fact, the final values of control parameters did not change considerably when  $M' > 2$ .

(iv) Three iteration stages were required to find a set of optimum control parameters for this hydraulic actuation system. Results showed that the objective function of the second iteration was

minimum among three objective function values. Table 5.2 shows the control parameters obtained for the second and third iteration with corresponding objective function values. It is seen that the optimization process is fast. This is because the addition of the fractional orders of the integrator and differentiator to the controller makes the control system more flexible and faster in achieving the performance requirements. This is an advantage over the IOPID controllers because the orders of the integrator and differentiator are always set to  $-1$  and  $+1$  in an IOPID scheme.

**Table 5.2** Control parameters of each iteration with corresponding objective functions values.

Iteration No.	$K_p$	$K_i$	$K_d$	$\lambda$	$\mu$	$J$
1	35	45	55	0.65	0.25	$2.24 \times 10^{-7}$
<b>2</b>	<b>175.6</b>	<b>106.6</b>	<b>169.4</b>	<b>0.651</b>	<b>0.168</b>	<b><math>6.51 \times 10^{-8}</math></b>
3	780.4	686.8	593.8	0.654	0.089	$1.52 \times 10^{-5}$

According to Table 5.2, control parameters of the second iteration were the optimum values as they minimized the objective function including both tracking and robust stability criteria. Therefore, the FOPID-based robust controller designed based on the IFT tuning technique is given by

$$C_{FOPID} = 175.6 + 106.6s^{-0.651} + 169.4s^{0.168} \quad (5.54)$$

There is no guarantee that the optimum parameters obtained by the IFT technique are global. The IFT algorithm stops when the first minimum objective function is achieved. However, the experiments show that the tuned control parameters result in a good performance even though they may not be the global optimum. Investigation of the locality or globality of the control parameters obtained by the IFT technique requires an extensive study.

(v) To find the FOPID control parameters, a nominal plant was considered first. The nominal plant included a  $80 \text{ kN/m}$  spring emulating the external load while no extra masses/ slave actuators were attached/ connected to the main actuator. Next, the FOPID parameters were tuned by conducting the experiments of the IFT technique on the nominal plant. The robust stability term was also used in the objective function, which resulted in a set of control parameters making the hydraulic actuator robust against the system uncertainties. Once the FOPID controller was designed, it was employed in the experimental setup considering the possible uncertainties such as the variations in the external load, friction and the inertia for the robustness analysis. In order to show the robustness of the proposed controller to different uncertainties and operating conditions, various experiments were conducted using: (i) three different springs ( $K_{ext} = 45, 80 \text{ and } 160 \text{ kN/m}$ ) emulating the external loads, (ii) two masses resembling the uncertainties that may happen in the mass of the actuator over time (see Figure 3.4a), (iii) one operating mode showing the effect of change in the friction (Figure 3.4b), and (iv) five reference signals to prove how robust the controller is against various reference inputs.

To examine the efficacy of the proposed robust position controller, a previously-developed QFT controller [7] was also employed for the same setup, and its results were compared with those of the FOPID controller. The QFT controller and its prefilter, used for the comparison purpose, are the same as the ones used for the internal leakage detection [*i.e.*, Eqs. (4.1) and (4.2)].

In the first set of experiments, the performances of both FOPID and QFT controllers were examined using various reference inputs. In these experiments, the stiffness of the spring was  $160 \text{ kN/m}$ . Figure 5.7 demonstrates how the hydraulic actuator tracks the step response using both controllers. With respect to Figure 5.7, the FOPID controller improves the settling time, and is much less sensitive to the friction effect as it generates almost smooth behavior in the steady

state response. On the other hand, the QFT controller has caused the hunting in the steady state. The problem of the hunting phenomenon has already been well-established [68], [107], [108]. The hunting occurs because of the use of the integer-order integrator ( $s^{-1}$ ) in the QFT controller while the noticeable slip-stick friction exists in the system [68]. This is clearly shown in Figure 5.7 where the QFT controller results in the fluctuations, after 2 sec, due to the existence of breakaway (stick) and Coulomb (slip) frictions in the hydraulic system. The FOPID controller does not take the integer-order integral of the error. The difference between the integer-order and fractional-order integral is in the way the error is integrated. The integer-order integral (IOI) plays the role of a filter whose impulse response function has a perfect memory (see subsection 5.1.3). Perfect memory means that the integral of the error is always taken over the whole past history of the signal without mitigating the effect of the history [102]. The fractional-order integrator captures the past history of the error signal partially and accumulates the preserved memory of the error during the time evolution of the system with loss or dissipation [102]. The dissipation causes the control signal not to be affected by all past states of the error signal compared to the IOI. Thus, the control signal does not change after 2 sec, and no extra control input is generated by the FOPID controller. As a result, the hunting phenomenon does not occur. It should be noted that the error shown in the close-up version of the FOPID response is originating from the encoder resolution. In this test rig, an encoder (Bourns Inc., model: ENS1J-B28-L00256-0016R) was utilized whose resolution is 0.032 mm/pulse with 256 pulses/revolution. The error shown in Figure 5.7 is around 0.021 mm which is smaller than the encoder resolution; that is, the encoder is not able to measure the step final value (*i.e.*, 5 mm) accurately.

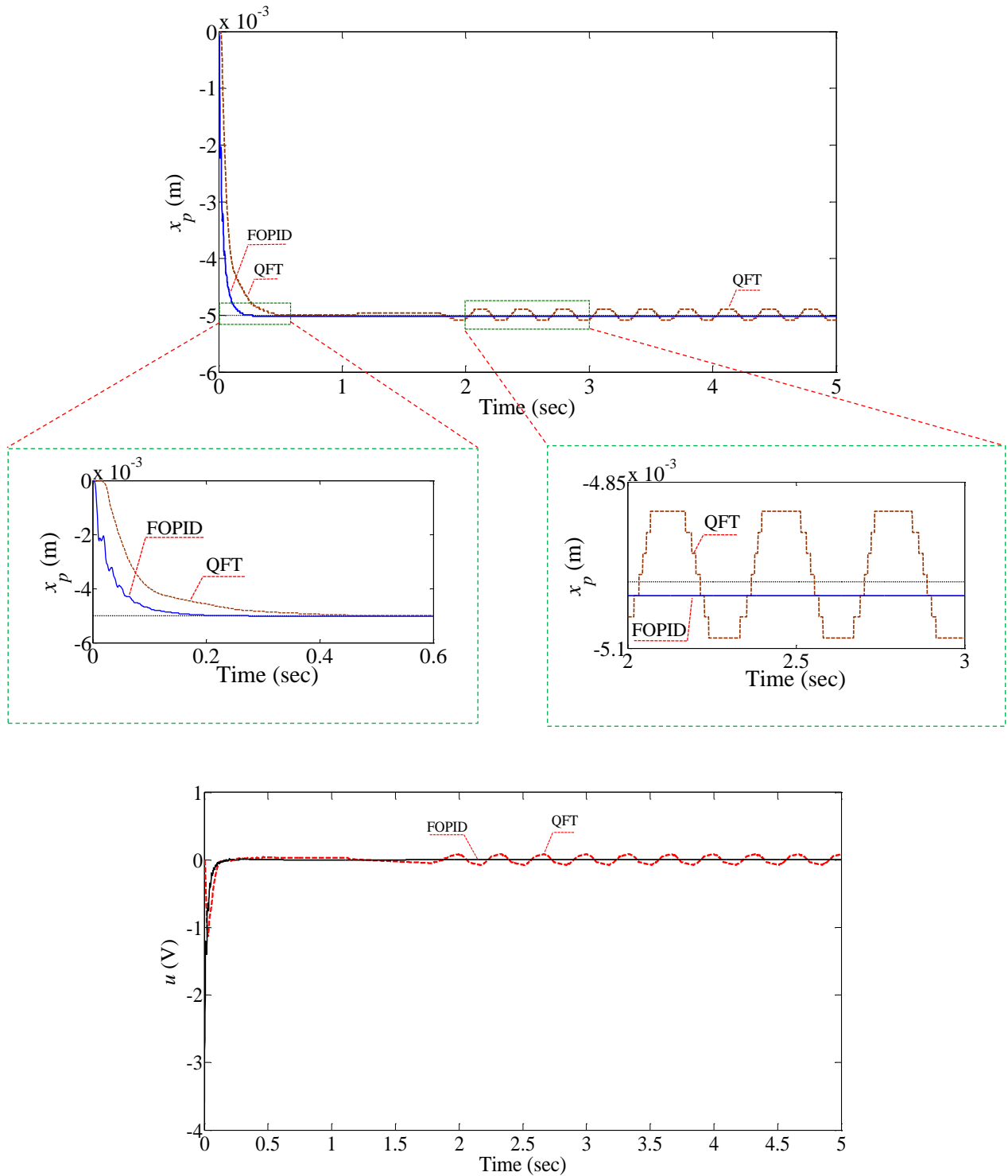


**Figure 5.7** Performance of FOPID and QFT controllers in tracking a step input of 5 mm pushing against a spring with stiffness of 160 kN/m.  $x_p$  represents piston displacement, and  $u$  is control signal.

To investigate the behavior of the FOPID controller in tracking variable step inputs, two more experiments were conducted. Figure 5.8 illustrates that the FOPID controller results in better tracking responses than the QFT controller. Moreover, the settling time of the system under FOPID scheme is still less than the one obtained when using the QFT controller.

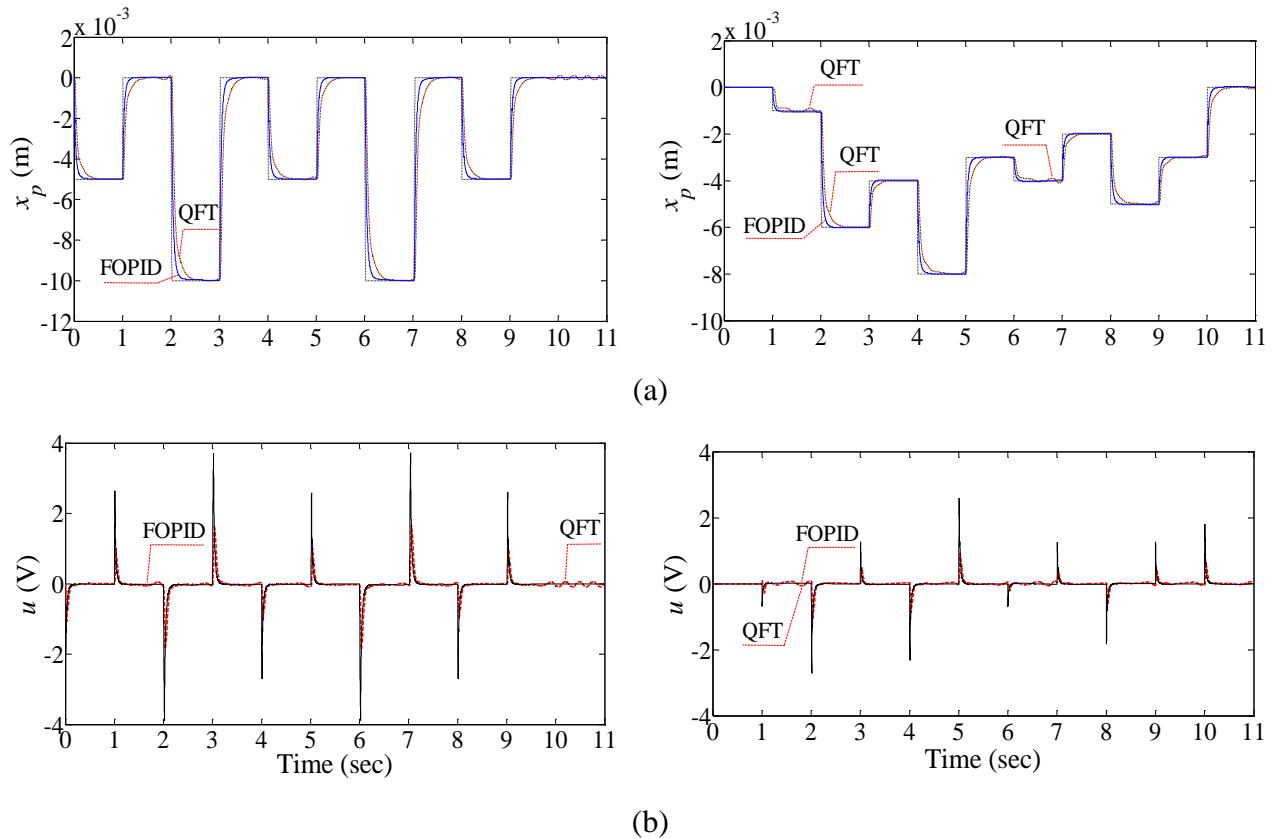


**Figure 5.8** Tracking responses to: (a) alternating step inputs and (b) random step inputs. Actuator is pushing against the spring with stiffness of  $160 \text{ kN/m}$ .

Sinusoidal signal was also used to observe the efficacy of both controllers in tracking the desired piston position varying constantly. As shown in Figure 5.9, the FOPID scheme tracks the sinusoidal input response better as compared to the QFT controller. With respect to Figure 5.9,

when the piston displacement is reaching the peak points, its velocity approaches zero. At the peak points, the breakaway friction is dominant. Around the peak points, the friction changes between the stick and slip values. In the hydraulic systems, the effect of the slip-stick friction is noticeable.

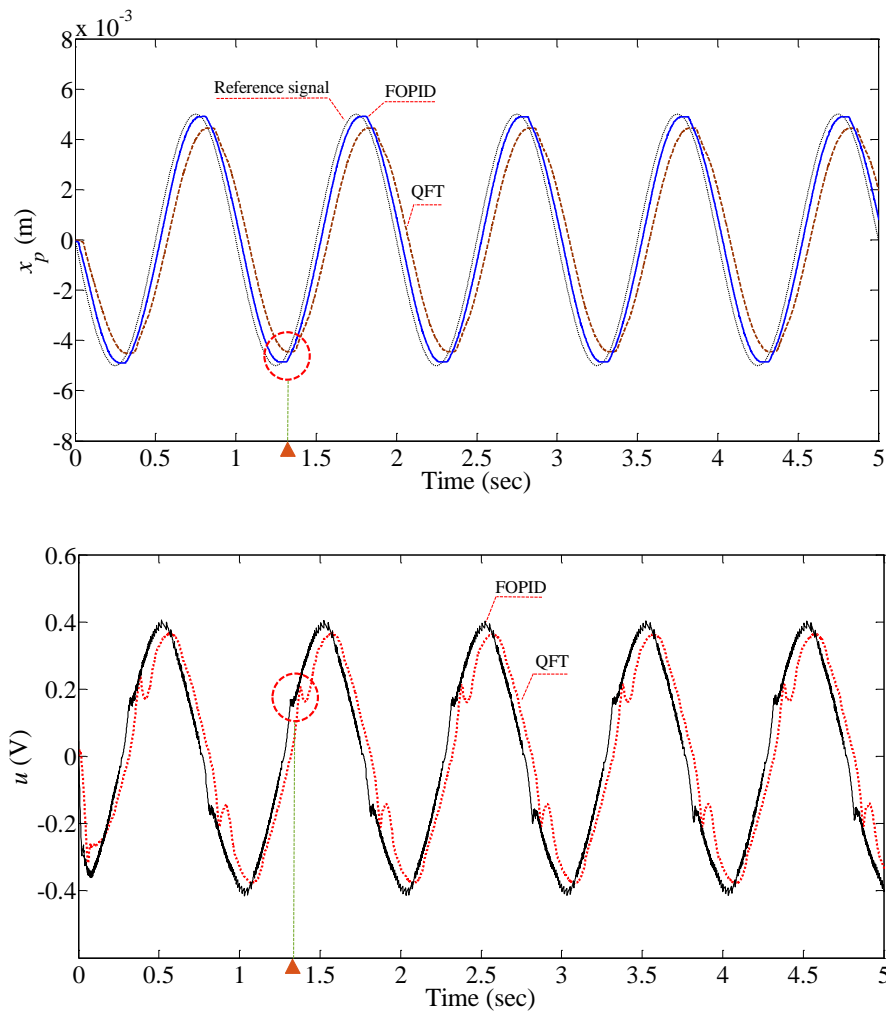


**Figure 5.9** Tracking responses to sinusoidal input. Stiffness of spring is  $160 \text{ kN/m}$ .

According to a set of the experimental results taken from the same test rig, the hydraulic actuator under study experiences a Coulomb friction of  $78 \text{ N}$  (in average) and the breakaway friction of  $200 \text{ N}$  (in average) while the actuation force equals around  $995 \text{ N}$  [68]. Therefore, the Coulomb

and breakaway frictions are large enough to cause the fluctuations in both FOPID and QFT control signals when the closed-loop response is tracking a sinusoidal reference input.

To verify the robustness of the FOPID controller to system uncertainties, including the external loads and change in the values of the friction and inertia, a set of experiments was conducted using combinations of three springs, two slave actuators and extra masses (see Figure 3.4). Figure 5.10 and Figure 5.11 provide results of five separate experiments for two reference inputs. In Figure 5.10, the error signals and corresponding control inputs of the experiments are shown when the piston tracks a fixed step input of 5 mm. Results of tracking the random step input are illustrated in Figure 5.11. Each experiment represents a certain change for the entire test. In the first and second experiments, we changed the external load by replacing the old spring (160 kN/m) by two new springs with the stiffness of 45 kN/m and 80 kN/m. In the third experiment, two extra actuators were connected to the main actuator to increase friction in the hydraulic actuator. In the fourth and fifth experiments, two extra masses were also added to the setup, without and with extra actuators, to investigate the robustness of the controller against changes in the value of combination of the mass and friction. In all cases, the same controller [Eq. (5.54)] was used. Results show that the FOPID controller is still robust against: (i) the external loads imposed by various springs, and (ii) the change in the values of the friction and inertia.

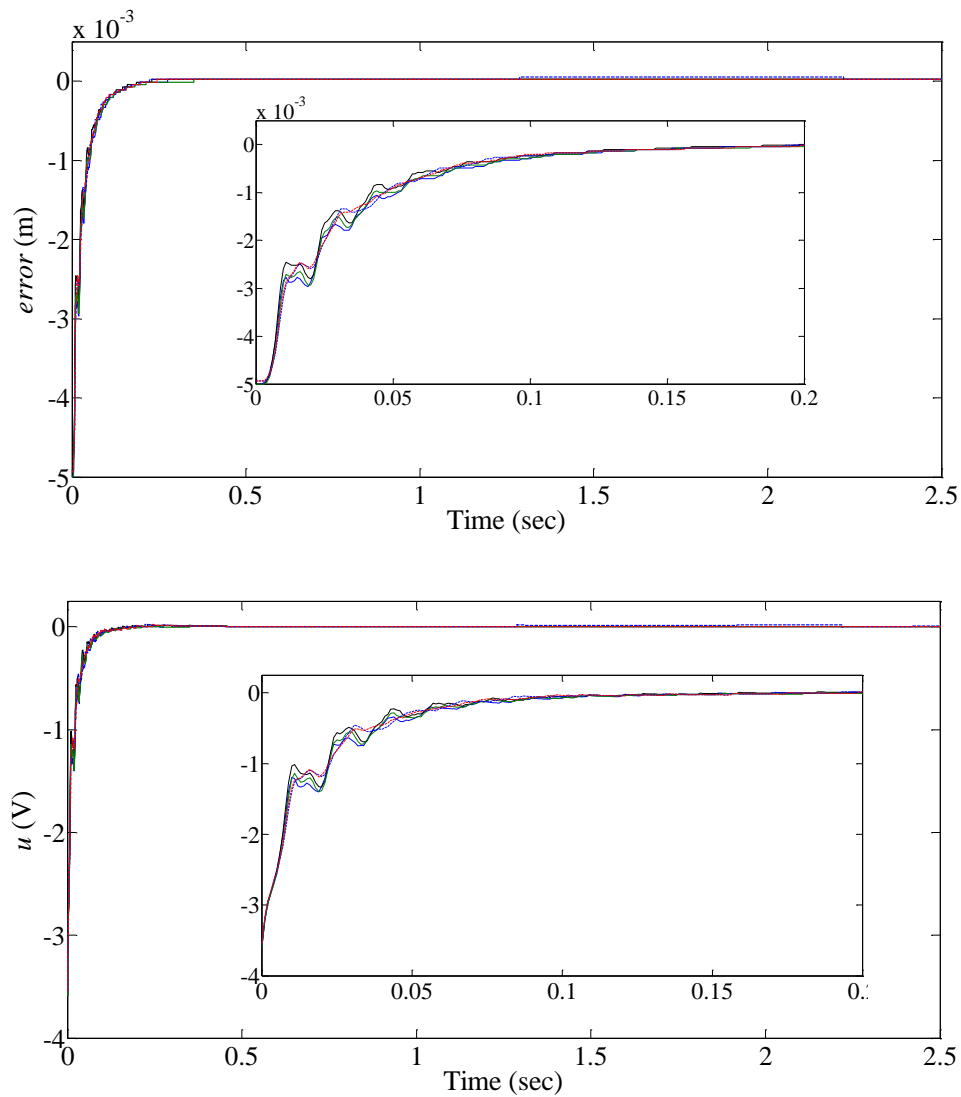


**Figure 5.10** Error signals and control inputs of five separate experiments showing robustness of FOPID controller when piston tracks step input of 5 mm. Stiffness of springs are equal to 45 kN/m, 80 kN/m and 160 kN/m, and extra masses and slave actuators are added to main actuator.

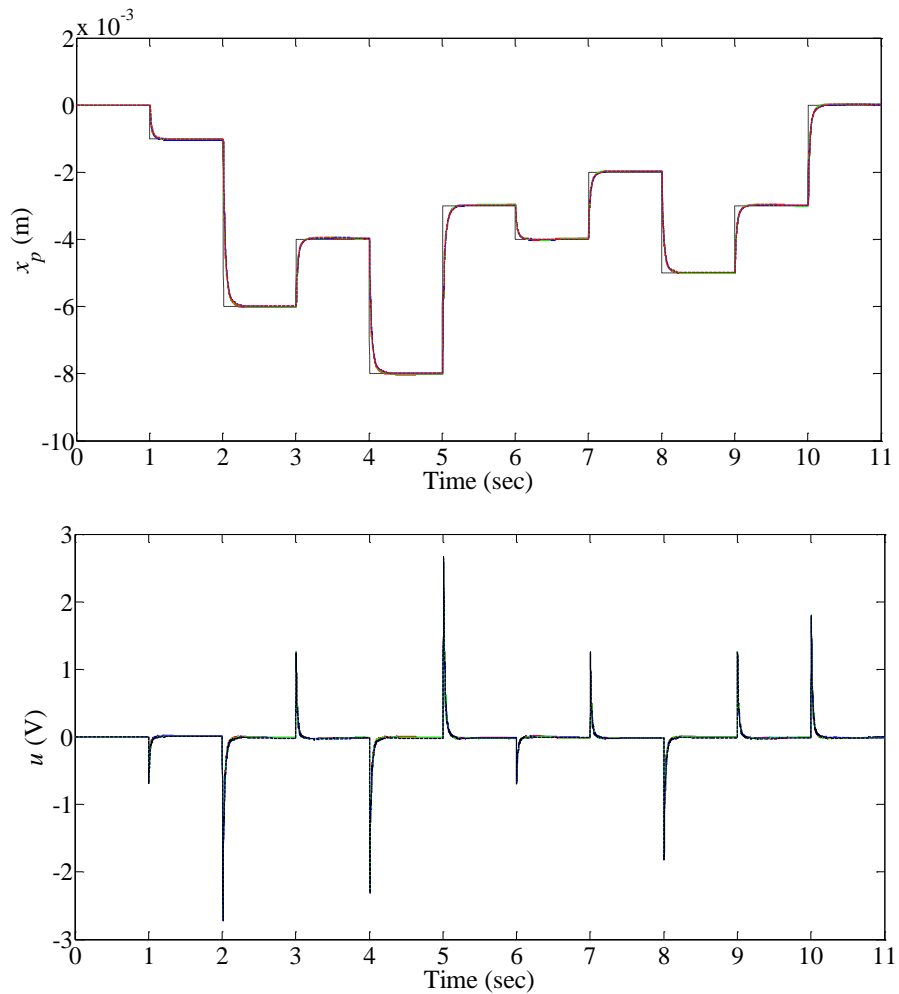


**Figure 5.11** Set of five experimental results considering various system uncertainties. Tracking responses of all experiments are comparable indicating robustness of FOPID controller.

Another experiment was conducted to emulate the sudden external force. At the beginning of this experiment, the actuator was at a distance away from the spring. Figure 5.12 illustrates the result of tracking a step input of 30 mm while the implement is 20 mm away from the spring (free motion), and then, pushes against the spring for 10 mm.

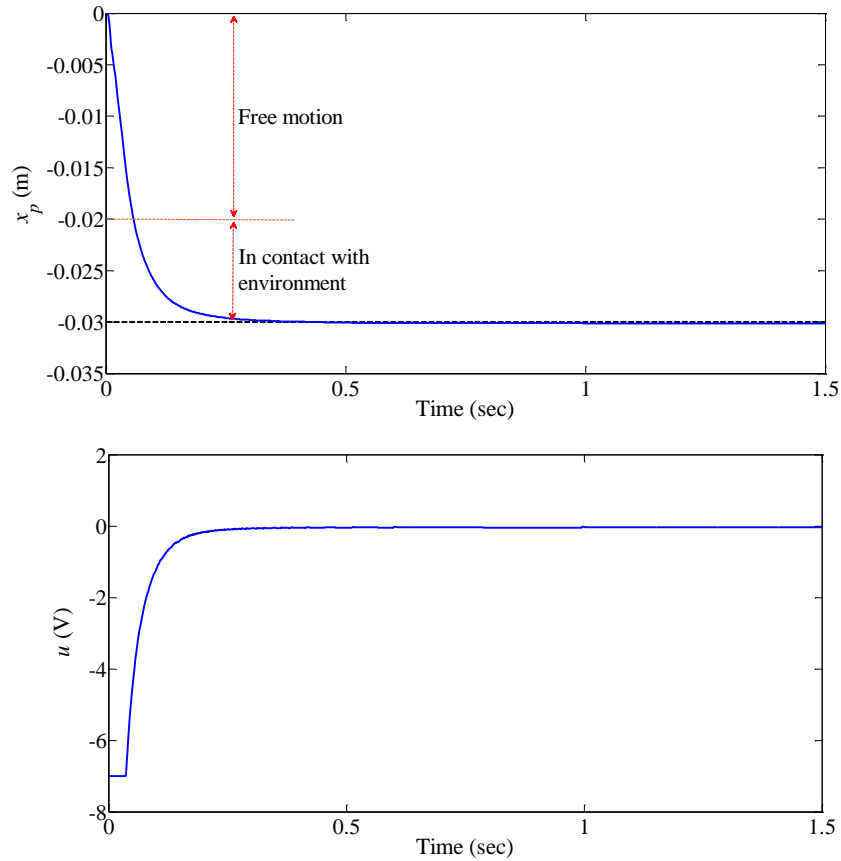


**Figure 5.12** Result of tracking step input of 30 mm when actuator experiences a sudden external force: (a) piston displacement; (b) control input. Stiffness of spring is 160 kN/m.

Finally, a set of experiments was designed to investigate the efficacy of the designed FOPID scheme in position control of a hydraulic actuator under varying external forces. The experimental setup, designed for this purpose, is shown in Figure 3.5. A loading actuator is utilized to generate a varying force applied to the main actuator. The loading part includes a valve which is controlled by a proportional force controller with a gain of  $K_p = 0.0033$ . The controller keeps the actual force close to the desired force profile. A load cell sensor is used to measure the actual force applied to the main actuator. A flexible coupling, between the load and main actuators, reduces the stiffness of the joint between them [15]. Such configuration can be used as a hardware-in-the-

loop simulator for applications such as aircraft [15] and wind turbines [109]. Figure 5.13 presents the block diagram of this configuration. The desired position and external load are given to the main actuator and load actuator, respectively. The piston displacement is controlled by the FOPID controller given in Eq. (5.54).

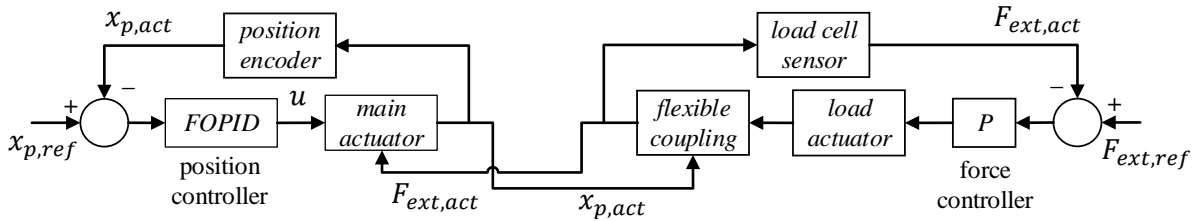


**Figure 5.13** Block diagram of hydraulic actuation system with load emulator;  $x_{p,ref}$  and  $x_{p,act}$  are position reference input and actual position, respectively;  $F_{ext,ref}$  and  $F_{ext,act}$  are desired and actual forces, respectively.

Result of tracking variable-step piston displacement in the presence of variable-step external load is illustrated in Figure 5.14. The external load is zero during the first 3 sec, and a force of 6 kN is then applied by the loading actuator. The value of the desired displacement changes at 6 sec while no change occurs in the external load. With respect to Figure 5.14, the FOPID controller was able to compensate for the effect of the variable external force and resulted in a good tracking response. The only undesirable tracking response occurred at 3 sec, when the value of external force changed to 6 kN abruptly. In another experiment, a sinusoidal external force was applied to the main actuator when tracking a fixed-step reference input. With respect to Figure 5.15, small oscillations have occurred in the displacement response which is because of the change in the direction of external load. However, the FOPID controller resulted in a good tracking response when the main actuator was under varying external loads.

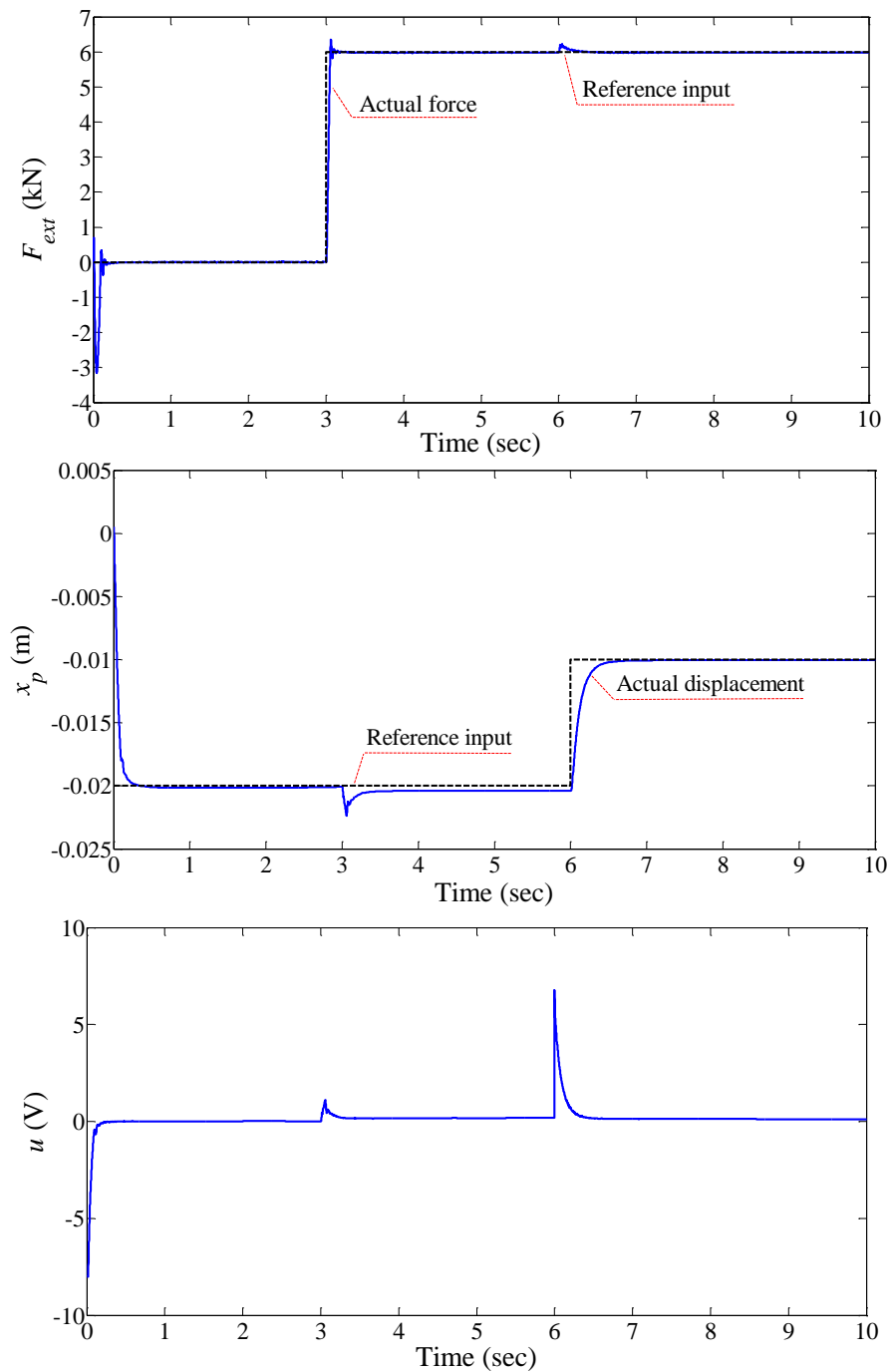


**Figure 5.14** Tracking of variable-step piston displacement when actuator is under variable-step external load.

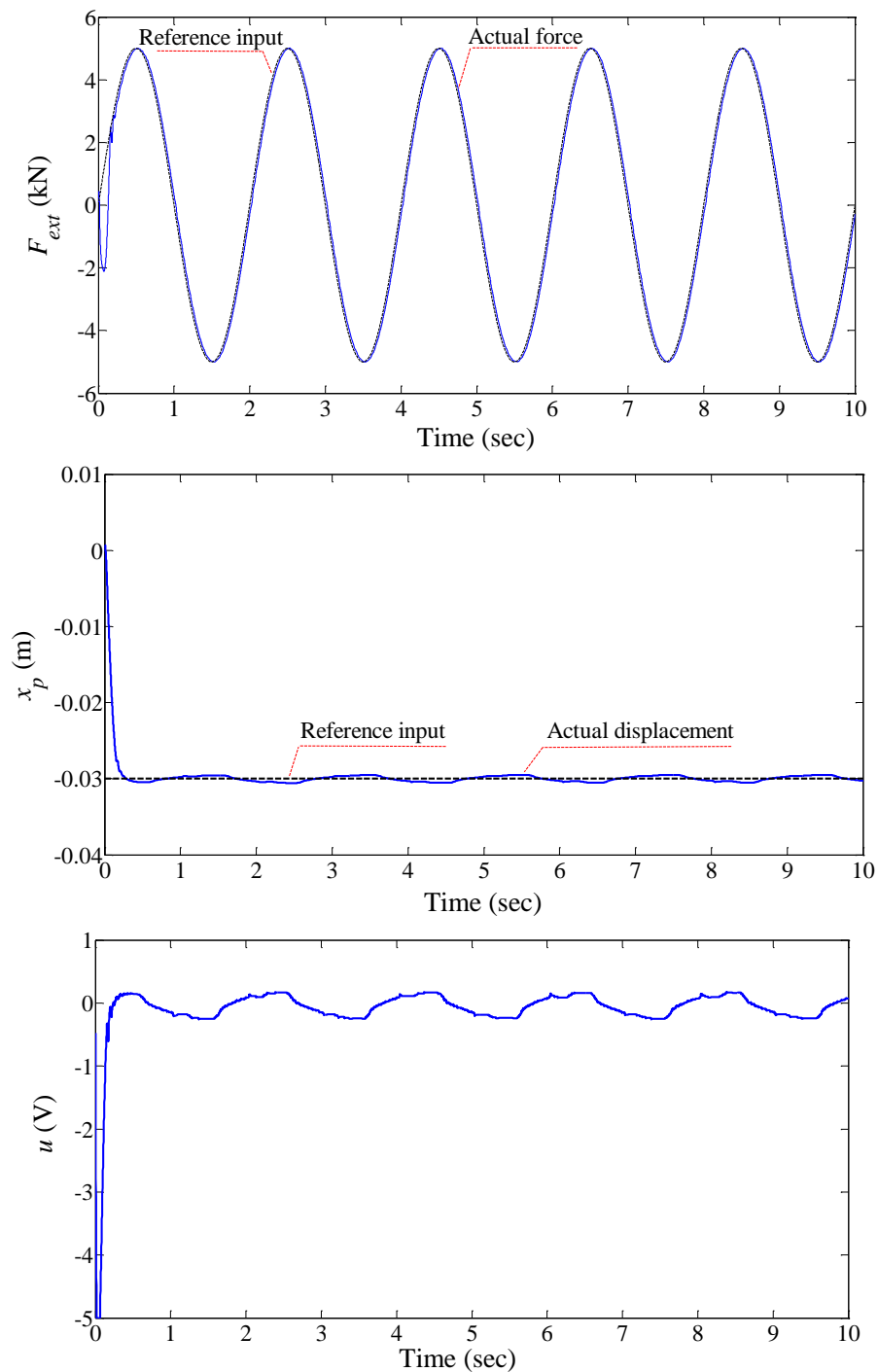


**Figure 5.15** Resulting position of hydraulic actuator under sinusoidal external load.

## 5.7. Summary

This chapter presented the procedure of designing a robust position controller for valve-controlled hydraulic actuators using the fractional-order PID schemes. First, various definitions and interpretations of the fractional-order operators were explained followed by the definition of the FOPID schemes. The Oustaloup recursive technique was employed to realize the infinite dimensional fractional-order operators in the Laplace domain. The iterative feedback tuning was used to tune five parameters of the FOPID controller using experimental data. To show the efficacy of the proposed FOPID-based robust controller, the results were compared to those of a previously-developed QFT controller. Experimental results showed the better performance of the proposed controller, in terms of improving both the settling time and sensitivity to the friction effect, as compared to the QFT one. In addition, the hydraulic actuator demonstrated robust behaviors towards various system uncertainties such as changes in the external load and increase in the values of friction and inertia.

This part of the thesis contributed to the development of a fractional-order PID scheme for the position control of hydraulic actuators which outperformed a previously developed proportional-based and integral-based position controller in the sense of tracking. Moreover, only experimental data taken from a position encoder were utilized for the controller parameters tuning.

In this chapter, the objectives (ii) and (iii) were achieved, and the research question (iii) was addressed.

## CHAPTER 6

# FAULT-TOLERANT CONTROLLER DESIGN

In this chapter, the results obtained from the internal leakage detection and design of the FOPID controller are employed to develop an FOPID-based fault-tolerant controller (FTC) for hydraulically-powered actuators. The goal is to develop a methodology, for designing FTCs, which does not rely on a prior knowledge about the model and parameters of the system and faults. The proposed methodology is based on introducing a set of synthetic errors to the hydraulic actuator. Synthetic errors are introduced to emulate an effect of the internal leakage on the system response. In Chapter 4, the wavelet transform revealed the best performance in detecting the internal leakage; thus, it is utilized to quantify the effect of various levels of synthetic errors on the error between the desired and actual displacement signals. In fact, the fault effect is investigated without (i) using any model of the fault, or (ii) reproducing the fault in the experimental setup. Having obtained results of the wavelet analysis, a quantity is defined corresponding to each level of the synthetic error, which is further used for the controller design. Next, FOPID controllers are designed, each for a certain level of the synthetic error, according to the procedure described in Figure 5.6. The robust stability index is utilized, in the tuning procedure, for compensation of the synthetic errors

effect. The robust stability index is determined based on the quantity derived from the wavelet analysis. Therefore, there is a connection between the wavelet analysis and the controller design procedure. A single FOPID controller is then chosen, from various designed controllers, which is the fault-tolerant position controller for the hydraulic actuator. Finally, a prefilter is designed in order to keep the tracking response within an acceptable region defined between a set of lower and upper bounds.

To design a fault-tolerant controller, only data of the position encoder, taken from experiments, are used. All experiments are conducted on a healthy hydraulic actuator (*i.e.*, no actual internal leakage is introduced to the hydraulic actuator). After designing an FTC, the internal leakage emulator is utilized, in the verification step, to create various levels of the internal leakage and verify the efficacy of the designed FTC when the hydraulic actuator experiences an actual fault (*e.g.*, the actuator internal leakage). Note that the leakage emulator is not used in the procedure of designing the fault-tolerant controller.

### **6.1. Introduction of Synthetic Errors**

The actuator internal leakage has been considered as the fault of choice to describe the procedure proposed here. Since the main effect of internal leakage on the system response is generation of errors, a set of synthetic errors is designed and applied to the healthy closed-loop hydraulic system to emulate the internal leakage effect approximately. The synthetic errors are introduced to the hydraulic actuator in the Simulink model connected to the experimental setup. Having applied the synthetic errors to the healthy actuator, displacement errors are subsequently generated in the piston position. Therefore, the synthetic errors are different from the piston

displacement errors. In other words, the synthetic error is a cause and the piston displacement error is the effect. To ensure that the synthetic errors are good representatives of *the internal leakage effect* on the system response, a wavelet analysis is performed on the generated piston displacement errors, and the results are compared with those already obtained in Section 4.4. In Chapter 4, the wavelet analysis of displacement error data revealed that the 4<sup>th</sup> level of the wavelet detailed coefficients is sensitive to the change in the flow rate of the internal leakage. To design the synthetic errors, the reference input, shown in Figure 6.1, is considered as the desired piston displacement.

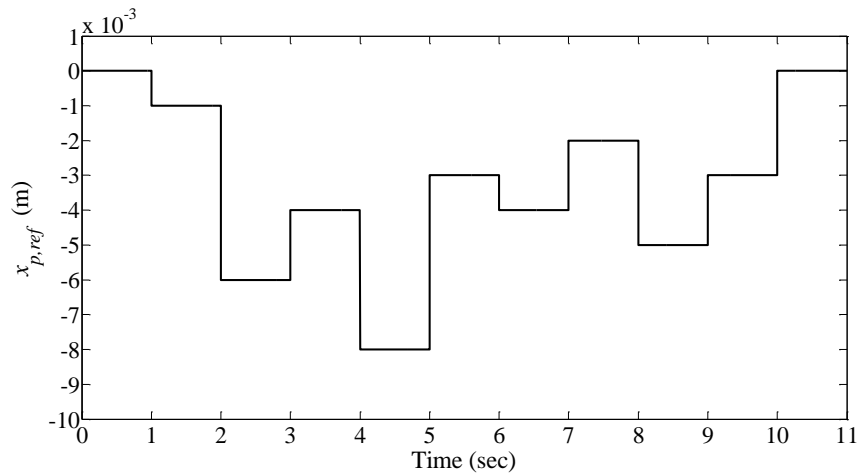


**Figure 6.1** Variable-step reference input ( $x_{p,ref}$ )

Figure 6.2 illustrates seven levels of the synthetic error representing the steady-state effect of different levels of the internal leakage on the piston position. The first and seventh levels of the synthetic error correspond to steady-state errors of 5% and 65% with respect to the reference input, respectively. The steady-state values have arbitrarily been chosen. The reason behind considering this range is to cover the effect of a wide range of the internal leakage on the piston displacement. The more the flow rate of the internal leakage is, the higher the value of steady-state

error will be in the absence of a fault-tolerant controller.

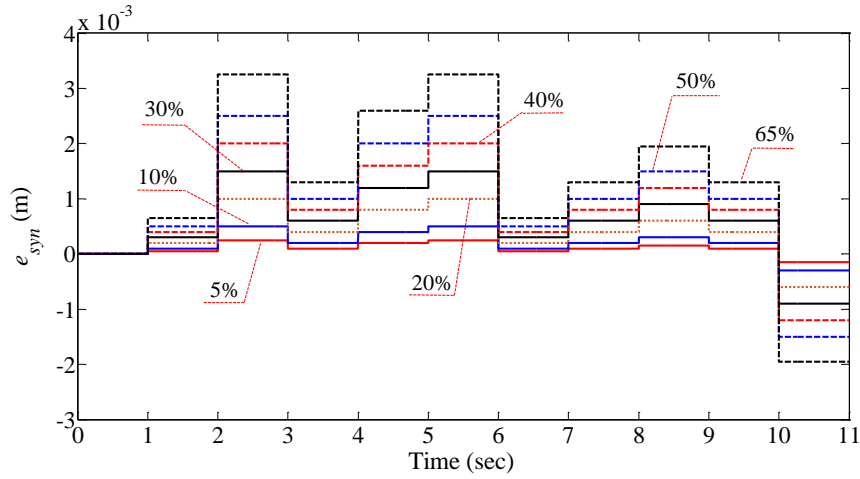


**Figure 6.2** Seven levels of synthetic error ( $e_{syn}$ ) generated based on reference input of different magnitudes. Synthetic errors range from 5% to 65% resembling effect of “small” to “large” internal leakage on piston displacement, respectively.

## 6.2. Wavelet Analysis

First, a healthy operating mode is considered for the hydraulic system under study. Healthy mode means that the hydraulic actuation system does not experience an internal leakage, which is hereafter called the “*base mode*”. In this step, each of synthetic errors of Figure 6.2 is applied to the healthy hydraulic actuator in separate experiments. Figure 6.3 illustrates the closed-loop system affected by the synthetic error. With respect to Figure 6.3, three different errors are defined;  $e_{syn}$  is the synthetic error applied to the closed-loop system to emulate effect of the internal leakage. The real error,  $e_r$ , is the one between the piston displacement,  $y$ , and reference input,  $r$ ,

$$e_r = r - y \quad (6.1)$$

The controller input,  $e_c$ , is defined as follows

$$e_c = e_r + e_{syn} \quad (6.2)$$

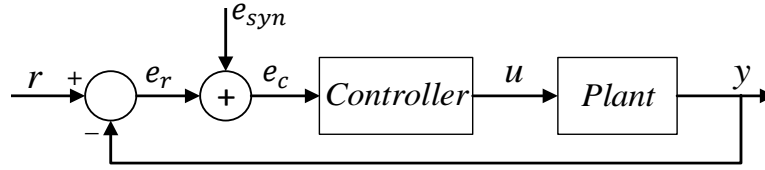


**Figure 6.3** Block diagram of closed-loop system affected by synthetic error:  $r$  denotes reference input;  $u$  is control signal;  $e_c$  is controller input;  $e_{syn}$  represents synthetic error introduced to closed-loop system;  $e_r$  is error between reference input and plant output. FOPID control scheme is presented by Eq. (6.3).

From the above error signals, the real error,  $e_r$ , is used for the wavelet analysis. As shown in Figure 6.3, a controller is required in the closed-loop system. In this step, the FOPID controller, designed in Chapter 5, is employed for the base mode, *i.e.*,

$$C_{FOPID} = 175.6 + 106.6s^{-0.651} + 169.4s^{0.168} \quad (6.3)$$

This controller is used in eight experiments. Since totally eight levels of the synthetic error (0%, 5%, 10%, 20%, 30%, 40%, 50%, 65%) are introduced to the hydraulic actuator, eight sets of real error data,  $e_r$ , are therefore obtained. The difference between the experiments is in the level of the synthetic error. Three of typical real errors, obtained from three experiments, are shown in Figure 6.4. Comparing the real error signals of Figure 6.4 with the displacement error data presented in Figure 4.22, it is concluded that the effect of the synthetic errors on the displacement error is relatively comparable to that of the actual internal leakage.

The next step is to apply the wavelet transform to the real errors data,  $e_r$ , and then, find the best sensitive wavelet detailed coefficient to the change of the synthetic error level. In this part of the study, five levels of the decomposition are performed on each set of the real error,  $e_r$ , and five

detailed coefficients are obtained for each  $e_r$ . The investigation of more decomposition levels did not change the outcome of the sensitivity analysis. To distinguish between the synthetic errors, each level of  $e_{syn}$  is represented by a percentage with respect to the reference input as shown in Table 6.1.

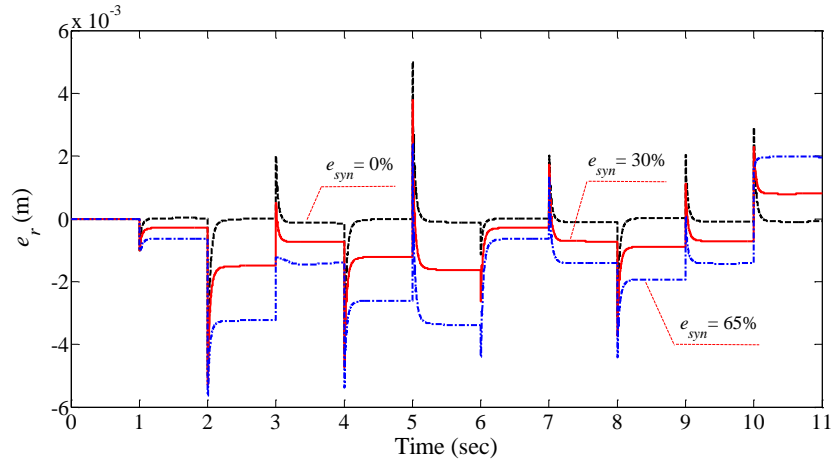


**Figure 6.4** Typical error signals,  $e_r$ , corresponding to three levels of synthetic errors.

The reason for investigating the behavior of only detailed coefficients is that they have shown good sensitivity to the internal leakage according to results of the internal leakage detection in Chapter 4 as well as the previous studies [11], [12]. Therefore, to find out if the designed synthetic errors could be good representatives of the internal leakage effects, one needs to verify whether any of the detailed coefficients shows a sensitivity to change of the synthetic error level. In order to apply the wavelet transform to the real error data, various standard mother wavelet functions were examined to find out which one operates better in detecting the effect of various levels of the synthetic error on the real error signal. The Daubechies-8 was finally chosen as it resulted in the best sensitivity analysis. Moreover, to investigate the effect of the synthetic error levels on the

wavelet detailed coefficients of the real error signal, the percentage of change of each coefficient with respect to that of the base mode (*i.e.*,  $e_{syn} = 0\%$ ) was calculated using

$$\delta_m^j (\%) = \frac{RMS(d_m^1) - RMS(d_m^j)}{RMS(d_m^1)} \times 100 \quad ; \quad j = 2, 3, \dots, 8 \quad (6.4)$$

where,  $\delta_m^j$  is the percentage of change; the subscript  $m$  refers to the number of the decomposition level ( $m = 1, 2, \dots, 5$ ); and, the superscript  $j$  denotes the counter of the synthetic error level such that  $j = 1$  belongs to  $e_{syn} = 0\%$ . Table 6.1 lists the RMS value of each wavelet detailed coefficient for eight operating modes.

**Table 6.1** Results of wavelet analysis on real errors of eight different conditions. No internal leakage was introduced into hydraulic actuator.

Operating Mode ( $e_{syn}$ )		Base mode	Seven levels of synthetic errors (Faulty operating modes)													
		0%	5% ( $j = 2$ )		10% ( $j = 3$ )		20% ( $j = 4$ )		30% ( $j = 5$ )		40% ( $j = 6$ )		50% ( $j = 7$ )		65% ( $j = 8$ )	
		$d_m^1$	$d_m^2$	$\delta_m^2$ (%)	$d_m^3$	$\delta_m^3$ (%)	$d_m^4$	$\delta_m^4$ (%)	$d_m^5$	$\delta_m^5$ (%)	$d_m^6$	$\delta_m^6$ (%)	$d_m^7$	$\delta_m^7$ (%)	$d_m^8$	$\delta_m^8$ (%)
RMS values of 5 decomposition levels	$m = 1$ ( $\times 10^{-5}$ )	4.35	4.35	-0.06	4.35	-0.03	4.35	-0.02	4.35	-0.02	4.35	0.00	4.35	-0.03	4.35	0.01
	$m = 2$ ( $\times 10^{-5}$ )	8.52	8.52	-0.09	8.52	-0.01	8.51	0.02	8.55	-0.35	8.52	-0.09	8.51	0.02	8.52	0.01
	$m = 3$ ( $\times 10^{-4}$ )	1.98	1.99	-0.37	1.99	-0.70	2.00	-0.99	2.00	-0.83	1.98	0.14	2.00	-0.89	1.99	-0.34
	$m = 4$ ( $\times 10^{-4}$ )	4.61	4.58	0.55	4.55	1.17	4.54	1.50	4.49	2.46	4.45	3.50	4.44	3.71	4.37	5.25
	$m = 5$ ( $\times 10^{-4}$ )	6.58	6.59	-0.09	6.56	0.32	6.55	0.59	6.59	-0.05	6.67	-1.25	6.60	-0.19	6.66	-1.15

The percentage of change of detailed coefficients of faulty operating modes with respect to those of the base mode was also calculated according to Eq. (6.4). It is confirmed, from Table 6.1, that the fourth level of detailed coefficients has shown the best sensitivity to the change in the level of the synthetic error. Other wavelet detailed coefficients did not exhibit any specific behavior toward different levels of the synthetic error. The results are in line with those obtained from

performing the wavelet analysis on the displacement error,  $e_r$ , when the hydraulic actuator experiences various levels of the actual internal leakage (see Table 4.8). Therefore, one can conclude that the synthetic errors are good substitutes for the effects of various levels of the internal leakage on the piston displacement error.

After finding the best sensitive wavelet detailed coefficient,  $d_4$ , (which belongs to the 4<sup>th</sup> level of decomposition), the approximation coefficient of the preceding level (*i.e.*,  $a_3$ ) is employed for the further analysis; because, each detailed coefficient is extracted from approximation coefficient of the previous level (see Figure 4.17). The reason for using the approximation coefficient of the preceding level is that it both contains all frequency components of the sensitive detailed coefficient  $d_4$ , and does not degrade the amplitude of the real error signal significantly. However, the detailed coefficients of a signal are not good representatives of that signal in terms of the amplitude and shape. Thus, the only usage of the detailed coefficients is in the sensitivity analysis part. In the final step of the wavelet analysis, a quantity is defined, based on the RMS values of  $a_3$ , as follows

$$\beta^j = \left[ \frac{RMS(a_3^j)}{RMS(a_3^1)} \right]^2 \quad j = 2, 3, 4, \dots, 8 \quad (6.5)$$

where  $a_3^j$  is the approximation coefficient of the third decomposition level of the real error when  $j^{th}$  level of the synthetic error is applied to hydraulic actuator;  $a_3^1$  represents the corresponding coefficient when the synthetic error is zero ( $e_{syn} = 0\%$ ). Note that  $\beta^j$  is not defined for  $j = 1$ . The parameter  $\beta^j$  quantifies effect of the  $j^{th}$  level of the synthetic error on the real error by employing the wavelet analysis. In fact, the wavelet transform is used to find out which frequency band of the real error signal is more affected by the synthetic error.  $\beta^j$  is hereafter called the “*fault-sensitive parameter*”, which is, in effect, the ratio of energy of wavelet of two operating modes.

The RMS value of the approximation coefficient  $a_3$  for various levels of the synthetic error as well as the value of  $\beta$  corresponding to each synthetic error level are listed in Table 6.2. This parameter is then used in the next step which is the controller design considering various levels of synthetic errors.

**Table 6.2** RMS values of level three wavelet approximation coefficient,  $a_3$ , and fault-sensitive parameter,  $\beta$ , corresponding to various levels of synthetic error.

Operating Mode		Base mode	Seven levels of synthetic errors ( $e_{syn}$ )						
		0% ( $j = 1$ )	5% ( $j = 2$ )	10% ( $j = 3$ )	20% ( $j = 4$ )	30% ( $j = 5$ )	40% ( $j = 6$ )	50% ( $j = 7$ )	65% ( $j = 8$ )
RMS Value	$a_3 (\times 10^{-3})$	1.12	1.23	1.47	2.07	2.83	3.59	4.41	5.65
	$\beta$	ND*	1.21	1.72	3.42	6.39	10.27	15.50	25.44

\* ND = Not Defined.  $\beta$  is defined for faulty operating modes only

### 6.3. Controller Design for Faulty Operating Modes

According to Figure 6.3, seven synthetic errors have been applied to the hydraulic actuator to emulate the effect of different levels of the internal leakage. Therefore, an FOPID controller will be designed for each synthetic error. Note that the zero-synthetic error ( $e_{syn} = 0\%$ ) implies that there is no internal leakage in the hydraulic actuator, and the FOPID controller already designed for the base mode is considered for  $e_{syn} = 0\%$  [Eq. (6.3)]. The procedure of designing an FOPID position controller for each faulty operating mode is the same as the one for the base mode. The objective function, to be minimized, is as follows

$$J(\rho_i) = \frac{1}{2N} E \left[ \sum_{k=1}^N \{ \alpha_y [\tilde{y}_k(\rho_i)]^2 + \alpha_s [C_k^{-1}(\rho_i) u_k(\rho_i)]^2 \} \right] \quad (6.6)$$

The importance of the robust stability index,  $\alpha_s$ , in designing a fault-tolerant controller is revealed here. In fact, this term helps the designer tune the controller parameters corresponding to each level of the synthetic error properly. If only the tracking term,  $\alpha_y$ , is used in the objective function, it will not result in a set of controller parameters capable of compensating fault effects. The fault-sensitive parameter  $\beta$  produced by the wavelet analysis is, in fact, the quantity used as the robust stability index in the controller design for each faulty mode, *i.e.*,  $\alpha_s^j = \beta^j$  ( $j = 2, 3, 4, \dots, 8$ ). Since the synthetic errors generate steady-state errors in the piston displacement, their effect must be compensated by tuning the integral parameters,  $K_i$  and  $\lambda$ , properly. The robust stability criterion affects the integral parameters,  $K_i$  and  $\lambda$ , significantly. A higher value of  $\alpha_s$  leads to higher values of  $K_i$  and  $\lambda$ . The fault-sensitive parameter  $\beta$  is the quantity representing effects of various levels of the synthetic error (or, the effect of the fault) on the piston displacement. By using  $\beta$  in the objective function (*i.e.*,  $\alpha_s = \beta$ ), resulting integral parameters will be able to compensate for the synthetic error (or, fault) effect for each faulty operating mode.

To design an FOPID controller for each of seven levels of the synthetic error, the same initial values of control parameters are used for the first iteration:

$$\rho_{initial} = [K_p, K_i, K_d, \lambda, \mu]^T = [35, 45, 55, 0.65, 0.25]^T \quad (6.7)$$

Moreover, the tracking index,  $\alpha_y$ , is the same and equal to 1 in all seven designs. The only difference, in the controller design for various faulty operating modes, is in the value of the robust stability index, because  $\alpha_s^j = \beta^j$  ( $j = 2, 3, \dots, 8$ ). By following the procedure described in Figure 5.6, seven sets of FOPID parameters were obtained, corresponding to seven values of  $\alpha_s$ , which are listed in Table 6.3. It is seen that the robust stability index  $\alpha_s$  affects the optimized values of FOPID parameters. The higher the value of the robust stability index, the lower the proportional

and derivative gains are. This reveals an importance of the robust stability criterion in designing a controller capable of compensating for the fault effect.

**Table 6.3** FOPID controller parameters of seven faulty operating modes and those of base mode. Faulty mode means synthetic error was introduced to closed-loop system. Maximum value of each controller parameter is highlighted.

Operating Mode ( $e_{syn}$ )	Base mode	Faulty modes created by synthetic errors							
	0%	5% ( $j = 2$ )	10% ( $j = 3$ )	20% ( $j = 4$ )	30% ( $j = 5$ )	40% ( $j = 6$ )	50% ( $j = 7$ )	65% ( $j = 8$ )	
$\alpha_y$	1	1	1	1	1	1	1	1	
$\alpha_s^j = \beta^j$	0.02	1.21	1.72	3.42	6.39	10.27	15.50	25.44	
FOPID control parameters	$K_p$	175.6	63.9	56.7	46.2	39.2	35.9	34.2	32.7
	$K_i$	106.6	353.6	362.2	507.9	606.7	729.7	849.1	1161.4
	$K_d$	169.4	68.7	64.3	58.8	55.4	53.5	51.8	50.3
	$\lambda$	0.651	0.692	0.713	0.739	0.738	0.764	0.804	0.859
	$\mu$	0.168	0.154	0.154	0.151	0.154	0.153	0.146	0.142

Having designed various FOPID controllers for the above operating modes, a unique FOPID scheme is chosen as the fault-tolerant controller. As illustrated in Table 6.3, eight sets of FOPID parameters are designed for eight operating modes including the base mode. To find a single set of controller parameters suitable for all ranges of the synthetic errors, from 0% to 65%, the maximum value of each controller parameter is chosen as follows

$$\vec{\rho}_{FTC} = [175.6, 1161.4, 169.4, 0.859, 0.168]^T \quad (6.8)$$

The vector  $\vec{\rho}_{FTC}$  represents parameters of the fault-tolerant controller. It is seen that the FTC parameters either belong to the base mode ( $e_{syn} = 0\%$ ) or the operating mode with the maximum

synthetic error (as highlighted in Table 6.3). It means that only two operating modes, in the controller design procedure, are required to achieve a set of control parameters for the FTC. However, one needs to consider more than two operating modes for the wavelet analysis to ensure that the chosen decomposition level is truly sensitive to the change in the level of the synthetic errors.

The reasons behind choosing maximum values of each controller parameter are to: (i) ensure the steady state error is always suppressed under a wide range of fault; (ii) decrease the oscillation in the steady state response; and (iii) keep the rise time as low as possible. To achieve (i), maximum values of “ $K_i$ ” and “ $\lambda$ ” should be chosen although they make the controller stiffer. If other value of “ $K_i$ ” is chosen, the controller would not be able to compensate for the large leakages. In order to reach minimum oscillations in the steady state response, the maximum value of “ $K_d$ ” and “ $\mu$ ” are chosen. As shown in Figure A.1 (see Appendix A), there is larger oscillation in the steady state response when lower  $K_d$  is used in the controller structure. Finally, the highest value of “ $K_p$ ” is selected to achieve the minimum rise time.

Furthermore, one may suggest that the controller corresponding to  $e_{syn} = 65\%$  (i.e.,  $C_{e_{syn}=65\%} = 32.7 + 1161.4s^{-0.859} + 50.3s^{0.142}$ ) can be a good choice for the FTC. A set of comparisons was performed between the tracking results when the FTC controller [Eq. (6.8)] and the controller corresponding to  $e_{syn} = 65\%$  are used in the hydraulic actuator (see Appendix A) in order to show better performance of the FTC. Results prove that the FTC should contain maximum values of all controller parameters to reduce the oscillations in the steady state response because the value of  $K_d (= 50.3)$ , in  $C_{e_{syn}=65\%}$ , is not high enough to overcome the overshoot and oscillations caused by the proportional and integral gains even if a prefilter is used.

It is also important to prove the system stability when the FTC controller is employed specifically for the healthy operating mode (*i.e.*, no leakage condition), because the value of  $K_i$  (= 1161.4) can be high for the healthy hydraulic actuator, and one requires to ensure that the system remains stable if the FTC of (6.8) is used in the healthy mode. Since this thesis deals with only the experimental data taken from test rig, an experiment was conducted without introducing a synthetic error to the plant, and input-output data was taken from the hydraulic actuator to derive a transfer function describing the plant behavior approximately. Then, the stability was proven using conventional techniques. Details of the stability analysis are mentioned in Appendix B.

#### 6.4. Prefilter Design

The final step is the inclusion of a prefilter into the closed-loop system, as illustrated in Figure 5.6. Note that the synthetic error will no longer be introduced into the system after determining the FTC parameters.

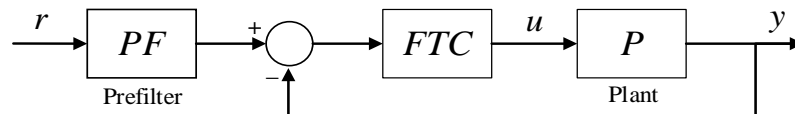


**Figure 6.5** Block diagram of closed-loop system consisting of a two-degree of freedom fault-tolerant controller.

The prefilter is necessary in designing a fault-tolerant controller because the proposed FTC scheme by itself does not result in a good performance for a wide range of the faults, and it generates the overshoot in the system response if there exists no internal leakage in the hydraulic

actuator. Therefore, one needs to design a prefilter to guarantee the performance of the entire system in presence of a wide range of the internal leakage that may occur [7], [15], [68].

Since this study deals with design of an FTC system using data-driven techniques, the prefilter is also designed based on experimental data. First, a set of upper and lower bounds, within which the final system response should lie, is defined. The upper bound, considered here, features a 2% settling time of 0.29 sec and a maximum overshoot of 2%. The lower bound has a 2% settling time of 0.98 sec with no overshoot. Transfer functions of the upper and lower bounds are defined as follows [68]

$$T_U(s) = \frac{(\frac{1}{4.7}s + 1)(\frac{1}{40}s + 1)}{(\frac{1}{6}s + 1)(\frac{1}{8}s + 1)(\frac{1}{30}s + 1)} \quad (6.9)$$

$$T_L(s) = \frac{1}{(\frac{1}{5}s + 1)(\frac{1}{9}s + 1)(\frac{1}{37}s + 1)(\frac{1}{200}s + 1)^2} \quad (6.10)$$

With respect to Figure 6.5, the system responses without and with the prefilter, in the Laplace domain, are expressed as follows

$$Y_{nl,wopf}(s) = \frac{FTC(s)P(s)}{1 + FTC(s)P(s)}R(s) \quad (6.11)$$

$$Y_{nl,wpf}(s) = PF(s) \frac{FTC(s)P(s)}{1 + FTC(s)P(s)}R(s) \quad (6.12)$$

where subscripts "*nl,wopf*" and "*nl,wpf*" mean "no leakage" condition (*i.e.*, healthy operating mode) without and with prefilter, respectively. In the FTC, the value of  $K_i$  is large for the healthy operating mode, which generates the overshoot in the system response  $y_{nl,wopf}(t)$ . By designing a suitable prefilter, the response  $y_{nl,wpf}(t)$  will lie between the responses of the lower and upper bounds. To design a prefilter, the following inequality must be met in the frequency domain [110]:

$$|T_L(j\omega)| \leq |PF(j\omega)| \left| \frac{FTC(j\omega)P(j\omega)}{1 + FTC(j\omega)P(j\omega)} \right| \leq |T_U(j\omega)| \quad (6.13)$$

where,

$$\left| \frac{FTC(j\omega)P(j\omega)}{1 + FTC(j\omega)P(j\omega)} \right| = \left| \frac{Y_{nl,wopf}(j\omega)}{R(j\omega)} \right| \quad (6.14)$$

Substituting Eq. (6.14) into (6.13),

$$|T_L(j\omega)| \leq |PF(j\omega)| \left| \frac{Y_{nl,wopf}(j\omega)}{R(j\omega)} \right| \leq |T_U(j\omega)| \quad (6.15)$$

In the Bode diagram, the magnitude relationship will be

$$20 \log(|T_L(j\omega)|) \leq 20 \log(|PF(j\omega)|) + 20 \log\left(\left| \frac{Y_{nl,wopf}(j\omega)}{R(j\omega)} \right|\right) \leq 20 \log(|T_U(j\omega)|) \quad (6.16)$$

In the above equation,  $|Y_{nl,wopf}(j\omega)|$  refers to the magnitude of the system frequency response in the healthy operating mode when there is no prefilter, *i.e.*,  $PF = 1$ . To find it, one needs to obtain the frequency response of the piston displacement using the experimental data. In this step, an experiment is performed by employing the FTC of Eq. (6.8) and considering  $PF = 1$  in the healthy operating mode. In this experiment, a constant step input of magnitude  $A$  (*e.g.*  $A = 0.01 \text{ m}$ ) is considered as the reference input, *i.e.*,  $r(t) = Au(t)$ . After acquiring data of  $y_{nl,wopf}$  from the experiment, its frequency response,  $Y_{nl,wopf}(j\omega)$ , can numerically be evaluated using the truncated continuous-time Fourier transform as follows [111] and [112]

$$Y_{nl,wopf}(j\omega) \cong \frac{1 - \cos(\omega h) + j \sin(\omega h)}{j\omega} \times \sum_{k=0}^{N-1} y_{nf,wopf}(kh) [\cos(\omega kh) - j \sin(\omega kh)] \quad (6.17)$$

where  $h$  refers to the width of the fixed integration interval. The efficacy of Eq. (6.17) in obtaining the frequency response of a set of experimental data has already been proven in [112]. Moreover,

the frequency response of the step input  $r(t) = Au(t)$  is numerically calculated using Eq. (6.17). This is because the frequency components of the term  $R(j\omega)$ , in the fraction  $\frac{Y_{nl,wopf}(j\omega)}{R(j\omega)}$ , must coincide with those of the term  $Y_{nf,wopf}(j\omega)$ . Moreover, the starting frequency in Eq. (6.17) is taken equal to the low-transitional frequency,  $\omega_b$ , defined in the Oustaloup technique. The reason is to avoid the problem of “division by zero” by considering the initial  $\omega$  equal to zero.

If the Bode magnitude of the term  $\left| \frac{Y_{nl,wopf}(j\omega)}{R(j\omega)} \right|$  is plotted, it is observed that the plot lies above that of the upper bound  $T_U(j\omega)$  because  $PF = 1$ . To design the prefilter, a program was written in MATLAB<sup>®</sup> software, and a set of poles and zeros was added to the pre-filter structure until the Bode magnitude plot of  $|PF(j\omega)| \left| \frac{Y_{nl,wopf}(j\omega)}{R(j\omega)} \right|$  shifted into the region between the plots of the lower and upper bounds. This is in line with the procedure mentioned in the QFT [110]. The designed prefilter is then used, with the FTC of Eq. (6.8), in the hydraulic actuator experiencing a wide range of the internal leakage. To meet the inequality (6.16), the following prefilter was designed and added to the system which kept the closed-loop frequency response inside the region generated by the bounds:

$$PF(s) = \frac{2.4(s + 25)}{(s + 5)(s + 12)} \quad (6.18)$$

## 6.5. Results and Discussion

The internal leakage emulator, shown in Figure 3.3, was employed to introduce the actual internal leakage into the hydraulic actuator, and examine the efficacy of the proposed fault-tolerant control system in compensating the effect of the internal leakage fault. Various reference inputs with different magnitudes were considered for the tracking purposes.

In all experiments, the 2-DOF control system comprising the FTC [Eq. (6.17)] and the prefilter [Eq. (6.18)] was utilized, and the actuator was pushing against the spring with stiffness of  $160 \text{ kN/m}$ . Figure 6.6 shows the system response to a variable step input for various levels of the internal leakage. To create different levels of the internal leakage, the position of the needle valve was changed. Notice that the abbreviations “NL”, “SL”, “ML” and “LL” are referred to as “No Leakage”, “Small Leakage”, “Medium Leakage” and “Large Leakage”, respectively. The type of the leakage was defined by the angle at which the needle valve opened. For the “no leakage” mode, the needle valve was completely closed. For the “SL”, “ML” and “LL” modes, the needle valve opened at a quarter, two and three quarters, respectively. With respect to Figure 6.6a, the effect of the internal leakage has been compensated by employing the proposed FTC scheme, and the piston position has tracked the reference input well. In addition, Figure 6.7b provides the information about the internal leakage flow rate and contains the flow rate values for three leaky modes. In the large leakage mode (LL), the flow rate reaches around  $7 \text{ L/min}$ . The close-up of the piston position, presented in Figure 6.6b, distinguishes the small discrepancy between the responses of NL, SL, ML and LL modes.

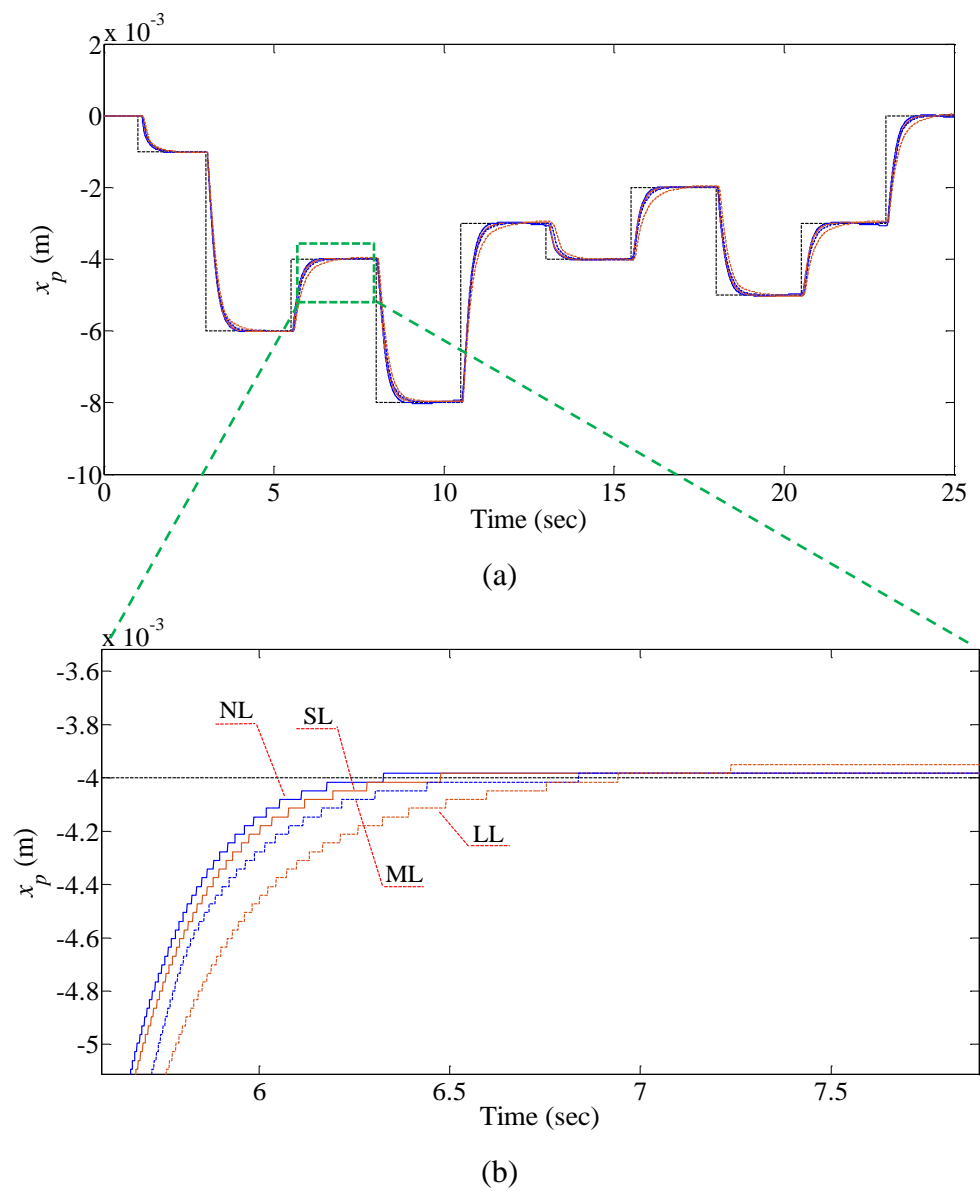


**Figure 6.6** Tracking responses to alternating step input in four operating modes NL, SL, ML and LL: (a) piston position; (b) close-up of piston position response.

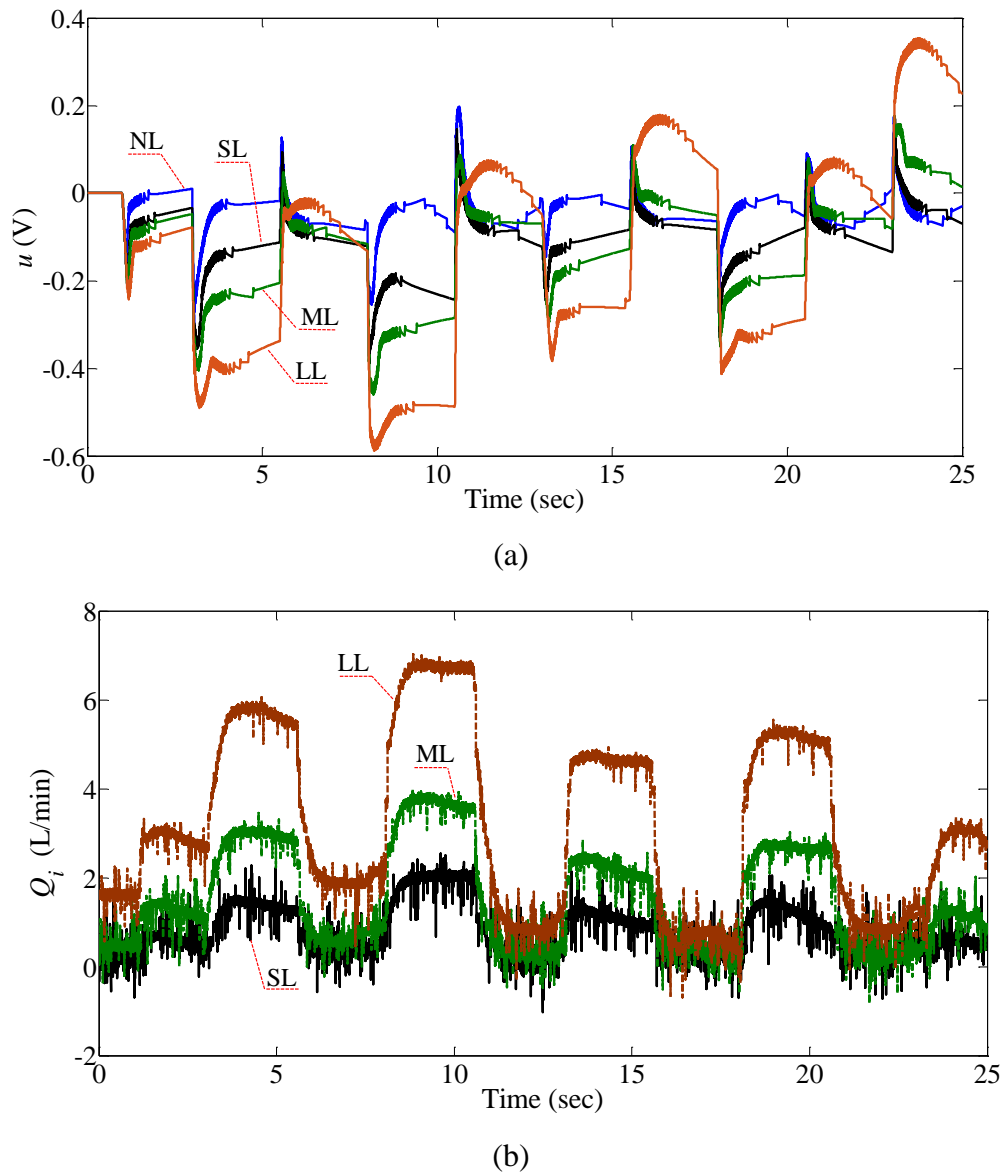


**Figure 6.7** (a) control signals corresponding to each level of internal leakage introduced to hydraulic actuator when tracking alternating step input of Figure 6.6; (b) leakage flow rates.

In order to observe the ability of the system in tracking the reference signals of higher magnitudes, four more experiments were conducted considering the variable step input shown in

Figure 6.8. With respect to this figure, the control system was capable of compensating for the effect of the internal leakage up to 11.5 L/min.

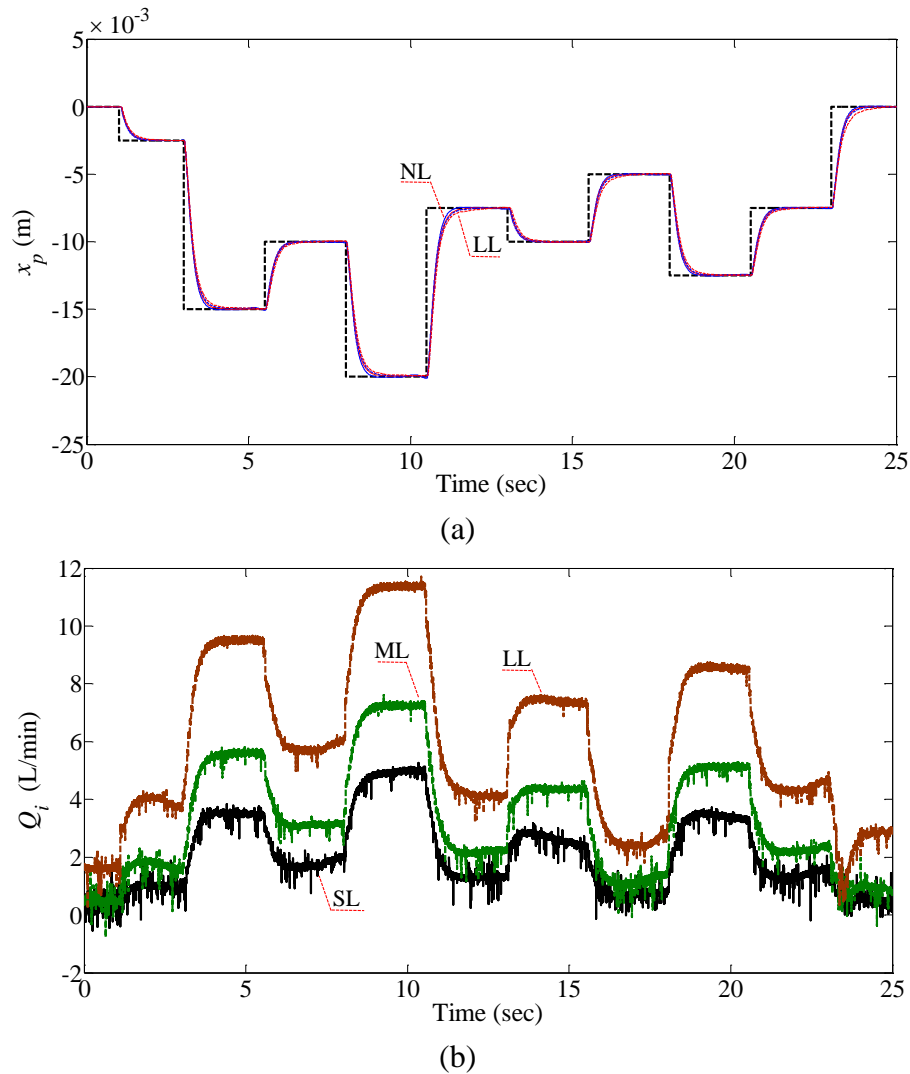
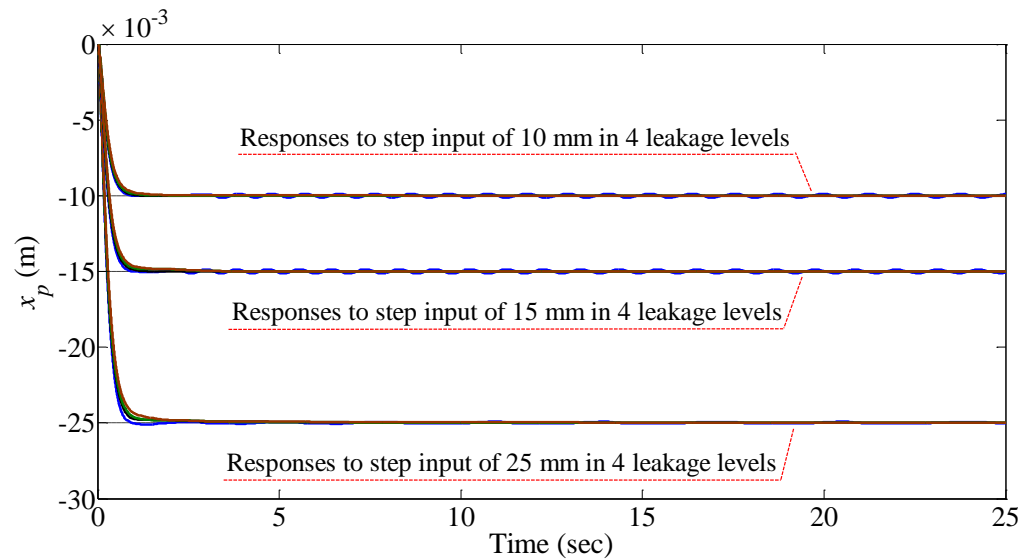


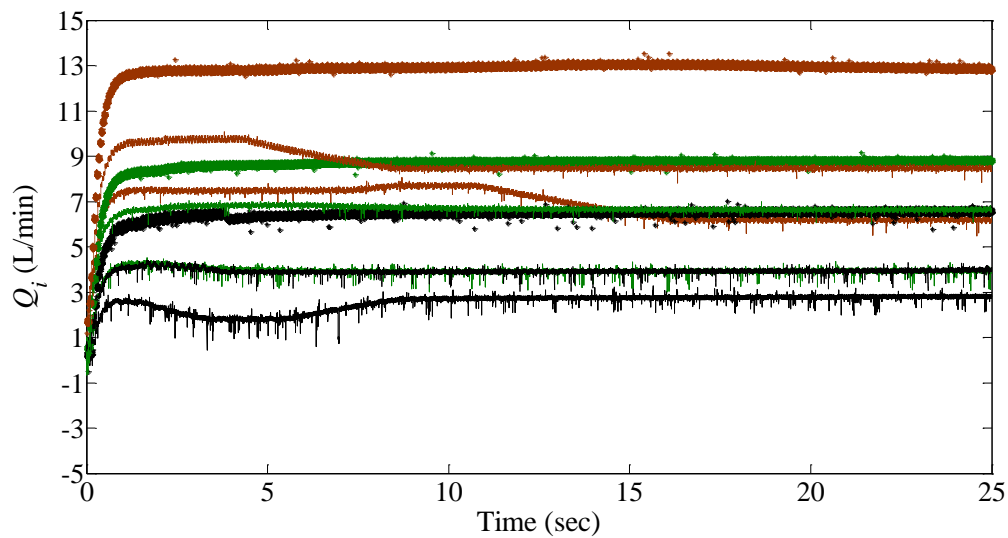
**Figure 6.8** Tracking responses to alternating step input of high magnitudes in four operating modes: (a) position response; (b) leakage flow rates.

The system responses to three constant step inputs of 10 mm, 15 mm and 25 mm are also illustrated in Figure 6.9. For each step input, four experiments were performed in NL, SL, ML and

LL operating modes. Results prove that the piston displacement tracks various step inputs well although the flow rate of the internal leakage reaches around  $13 \text{ L/min}$  (see Figure 6.9b). Note that Figure 6.9a comprises twelve results of three reference inputs and four operating modes.



(a)



(b)

**Figure 6.9** Tracking responses to step inputs of 10 mm, 15 mm and 25 mm, each in four operating modes: (a) position response; (b) leakage flow rates.

As observed in Figure 6.9a, there is a small hunting in the system response when step inputs of 10 mm and 15 mm are tracked in the NL mode. This is because there exists slip-stick friction in the hydraulic actuator, and the order of the integrator, in the FTC, is relatively high (*i.e.*,  $\lambda = 0.859$ ). Moreover, the hunting phenomenon occurs when the integer-order integrator ( $s^{-1}$ ) is used in the control system of a hydraulic actuator experiencing a noticeable friction. If the fractional-order integrator is used, the lower the order of the integrator is, the smoother the system response will be. On the other hand, if the order of the fractional integrator decreases, the tolerance level to the internal leakage will subsequently reduce. Therefore, there is a trade-off between existence of small hunting in the steady state response (for small step inputs) and tolerance level to the leakage.

In the final set of experiments, the internal leakage flow rate was increased gradually while the experiment was running. Figure 6.10 shows the results of tracking a step input of 20 mm. As shown, the level of the leakage has increased almost every 5 sec during the experiment. Although the leakage flow rate starts changing from almost zero to greater than 10 L/min, the piston displacement tracks the step input well. The only undesirable performance has occurred around 6 sec which is because of changing the needle valve position abruptly. This abrupt change can be observed in Figure 6.10b when the leakage flow rate jumps from less than 4 L/min to more than 6 L/min immediately.

Overall, the results of all experiments prove the efficacy of the proposed methodology in designing a fault-tolerant position controller using the data of a position sensor only. Beside the advantages of the proposed methodology, its drawback may be the number of experiments required for the wavelet analysis and the controller design steps. This number can be reduced according to the design objectives. For example, there is no need to consider the synthetic errors of 50% and 65% if the tolerance to the less flow rate of the internal leakage is of concern. Consideration of

synthetic errors up to 65% has resulted in the tolerance to the internal leakage with the flow rate up to 13 L/min (see Figure 6.9b). Notice that a lower level of the synthetic error results in a lower value of the integral gain and its fractional-order in the FTC of Eq. (6.17).

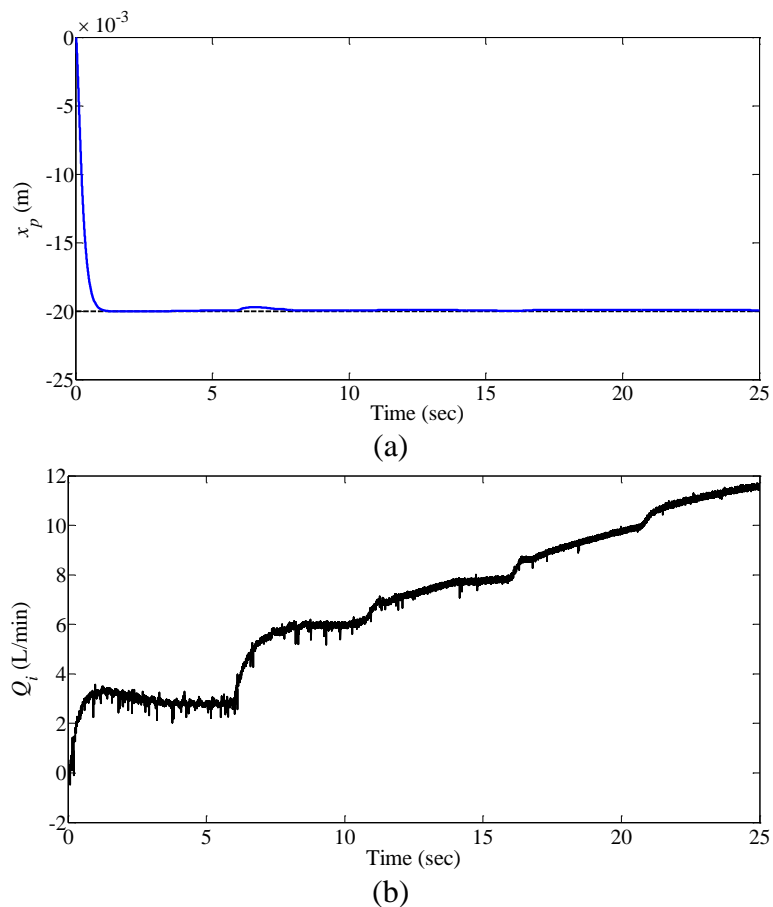


**Figure 6.10** Tracking response to step input of 20 mm in presence of varying internal leakage: (a) displacement response; (b) leakage flow rates.

## 6.6. Summary

In Chapter 6, a practical methodology was developed for designing fault-tolerant controllers in the hydraulic actuators. The methodology was exemplified with the design of a controller

tolerant to the internal leakage. The design procedure was based on introducing a set of synthetic errors to the hydraulic actuation system aiming to emulate the effect of the internal leakage on the system performance. A sensitivity analysis was conducted on the experimental data using the wavelet transform to find the best sensitive wavelet coefficient to the change in the level of the synthetic errors applied to the hydraulic system. Then, a fault-sensitive parameter was defined based on the results produced by the wavelet analysis, which was used in the controller design for several faulty operating modes. The FOPID schemes designed for all operating modes were collected and a single fault-tolerant controller was chosen. Moreover, a prefilter was designed to guarantee the system performance in the transient state. Several experiments were carried out to show the efficacy of the proposed methodology. Results proved that the developed FOPID-based FTC scheme was capable of tracking various reference inputs with different magnitudes. Moreover, the FTC made the hydraulic system tolerant to the internal leakage up to 13  $L/min$ .

The main contribution of this part of the thesis was development of a methodology for designing fault-tolerant position controllers using experimental data taken from a position sensor, and without requiring: (i) a prior information about the model and parameters of the plant and faults, and (ii) reproducing the fault in real experimental setup for the controller design. This approach may be of interest to industrial applications where the derivation of the accurate models for the systems is difficult, and there exist many sources of uncertainties and faults. In addition, it could be applicable to other systems which suffer from the faults effects on their performance.

Based on the results of this chapter, the objective (iv) was met, and the research question (iv) was answered.

# CHAPTER 7

## CONCLUSIONS

In this thesis, the application of data-driven techniques of the fault detection and fault-tolerant controller design to a valve-controlled hydraulic actuation system, experiencing the internal leakage, was investigated. Overall, four major concepts were covered: (i) multiscale analysis of experimental data, (ii) fractional-order PID schemes, (iii) realization of fractional-order operators, and (iv) control parameter tuning without requiring the system model.

### 7.1. Thesis Contributions

This thesis addressed the use of data-driven techniques of the controller design in hydraulic actuators. It also contributed to the fault detection using multiscale analysis of experimental data. The summary of the contributions made by this research study can be listed as follows

- (i) The concept of the multiscale analysis of experimental data was presented and the internal leakage in the hydraulic actuators was detected, for the first time, by quantifying a set of

multiscale measures obtained from one of the pressure signals of the actuator chambers. Details on the proper performance of the sampling, stationarity and fractality tests were provided. The concepts of reconstruction of an embedding space, finding an optimal lag and determination of a minimum embedding dimension using a single-variable experimental data were explained. In practice, these concepts are prerequisites for the multiscale analysis. Results proved that the pressure signal of the hydraulic actuators revealed the fractality property, which has the potential for further studies in order to extract useful information about the signal and the hydraulic actuation system. The wavelet transform showed reliable results in detecting various levels of the actuator internal leakage. Furthermore, the wavelet transform was applied to data of displacement error of different operating modes, and the results revealed the sensitivity of level four of the wavelet detailed coefficients to change in the flow rate of the internal leakage.

- (ii) A fractional-order PID (FOPID) position controller was designed using experimental data taken from an encoder reading the piston displacement. Controller parameters were tuned considering an objective function which included both tracking and robust stability criteria. The robust stability criterion was used, for the first time, in the procedure of the controller parameter tuning in hydraulic actuators. The proposed FOPID controller demonstrated good robustness properties and better tracking performance than a QFT controller designed for the same test rig before. Since the FOPID structure did not include integer-order integrators, it could overcome the hunting phenomenon. As known, hunting occurs when an integer-order integrator is used in the hydraulic actuators experiencing a noticeable slip-stick friction.

- (iii) A novel methodology was developed for designing fault-tolerant position controllers in hydraulic actuators. In the proposed methodology, there was no need for having a prior knowledge about the model of the hydraulic system and the fault as well as emulation of the fault during the experiments. The procedure was based on introducing a set of synthetic errors into the hydraulic actuator that is otherwise operating in the healthy mode. The synthetic errors were employed to emulate the fault effects on the system response. Results of implementing the designed FTC proved that the methodology works well for the hydraulic actuator experiencing the internal leakage.

## 7.2. Thesis Conclusions

There are some facts that can be concluded based on this study:

- (i) Fractional-order controllers (FOCs) outperforms the integer-order control schemes because of the flexibility that exists in the FOC structure. Integer-order operators are special cases of the fractional-order ones, and are useful for limited number of applications because the order of the integrator and differentiator is always equal to one. For instance, the Integer-order Calculus is not able to answer many questions about the dynamical systems exhibiting the chaotic behavior. Therefore, the use of fractional-order operators in predicting the behavior of dynamical systems seems to be more useful than that of the integer-order operators.
- (ii) There are various types of faults, parametric and non-parametric uncertainties in industrial equipment, which make the problem of analyzing the systems for the fault detection and controller design challenging. Since today's data acquisition systems are advanced enough

to acquire experimental data with high accuracy, the application of data-driven techniques, in the analysis and control of various industrial systems, can be more advantageous than the use of model-based methods.

### 7.3. Extension of This Work

The suggestions for the extension of this work include, but are not limited to, the following tasks:

- (i) Statistical analysis of the results obtained from data-driven techniques, e.g., calculation of standard error of measures in order to provide a range of uncertainties for the results.
- (ii) Multiscale analysis of experimental data taken from a hydraulic actuation system experiencing multiple faults (*e.g.*, combinations of the external leakage, change in the fluid compliance and the internal leakage), and investigating the possibility of isolating each fault using various multiscale measures.
- (iii) Investigating the efficacy of the methodology, proposed for the FTC, in designing position controllers tolerant to multiple faults.
- (iv) Stability analysis of fault-tolerant control system by modelling the hydraulic actuator with piecewise-affine system formulations or by approximating it as a linear system with polytopic parameter uncertainties.
- (v) Design of speed control systems for hydraulic actuators using FOPID schemes.

# APPENDIX A – COMPARISON BETWEEN FOPID CONTROLLERS

In Chapter 6, eight FOPID controllers were designed, each corresponding to one operating condition (see Table 6.3). The operating conditions were defined based on the introduction of synthetic errors to the healthy hydraulic actuator. This appendix provides a comparison between the performances of the designed FTC and the controller corresponding to the synthetic error of  $e_{syn} = 65\%$ . The controllers are as follows:

$$C_{FTC} = 175.6 + 1161.4s^{-0.859} + 169.4s^{0.168} \quad (\text{A.1})$$

$$C_{e_{syn}=65\%} = 32.7 + 1161.4s^{-0.859} + 50.3s^{0.142} \quad (\text{A.2})$$

For each controller, a number of experiments were performed in “no leakage” and “large leakage” operating modes with and without the prefilter. Tracking results are shown in Figure A.1 to Figure A.4. As illustrated, the Controller  $C_{e_{syn}=65\%}$  creates large overshoots and oscillations in tracking the step input, in “no leakage”, because the value of  $K_d$  is not large enough to suppress the effect of the integral and proportional gains. Even when the prefilter is used (see Figure A.2), the oscillations still exist in the steady-state response. On the other hand, the fault-tolerant controller,  $C_{FTC}$ , results in better tracking responses specially when the prefilter is used. In the

“large leakage” operating mode, tracking results of the controller  $C_{FTC}$  are also better as compared to those of the controller  $C_{e_{syn}=65\%}$ .

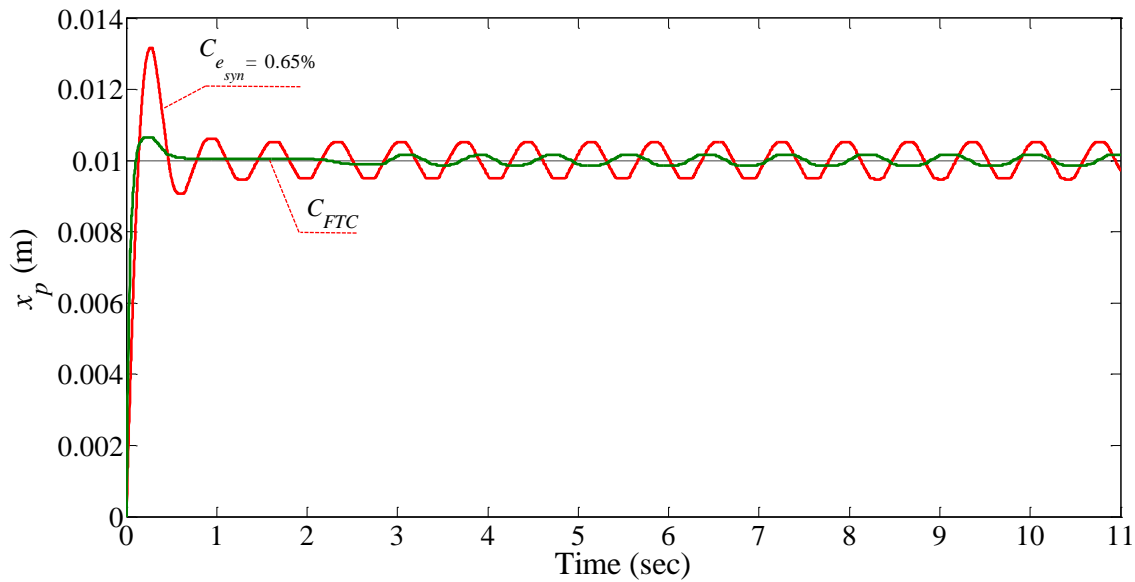


**Figure A.1** Tracking responses to step input of 10 mm when no prefilter is used and there is no internal leakage in the hydraulic actuator.

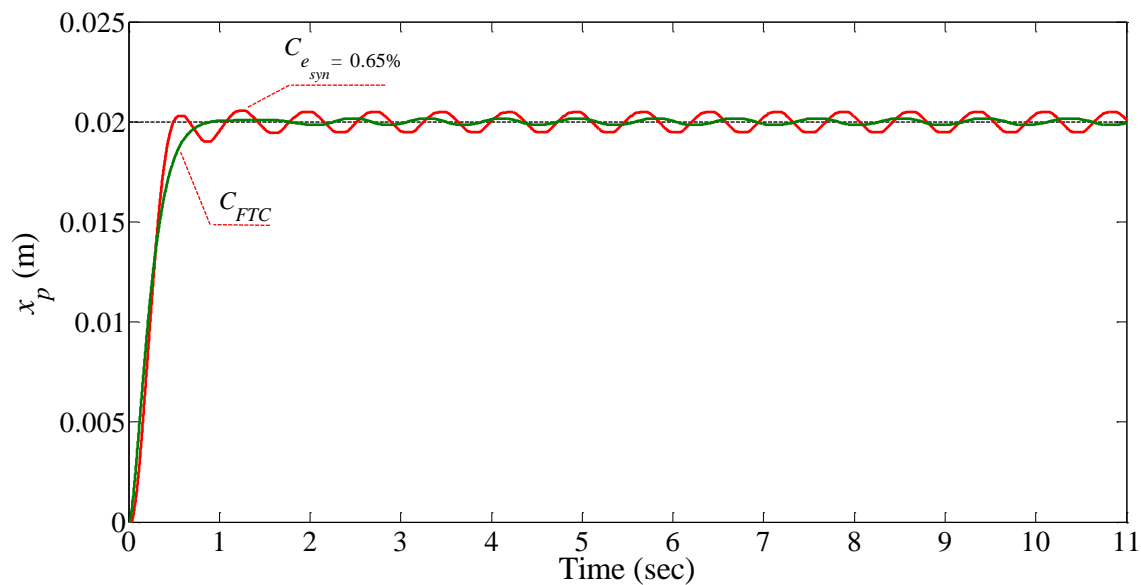


**Figure A.2** Tracking responses to step input of 20 mm with prefilter and no internal leakage.

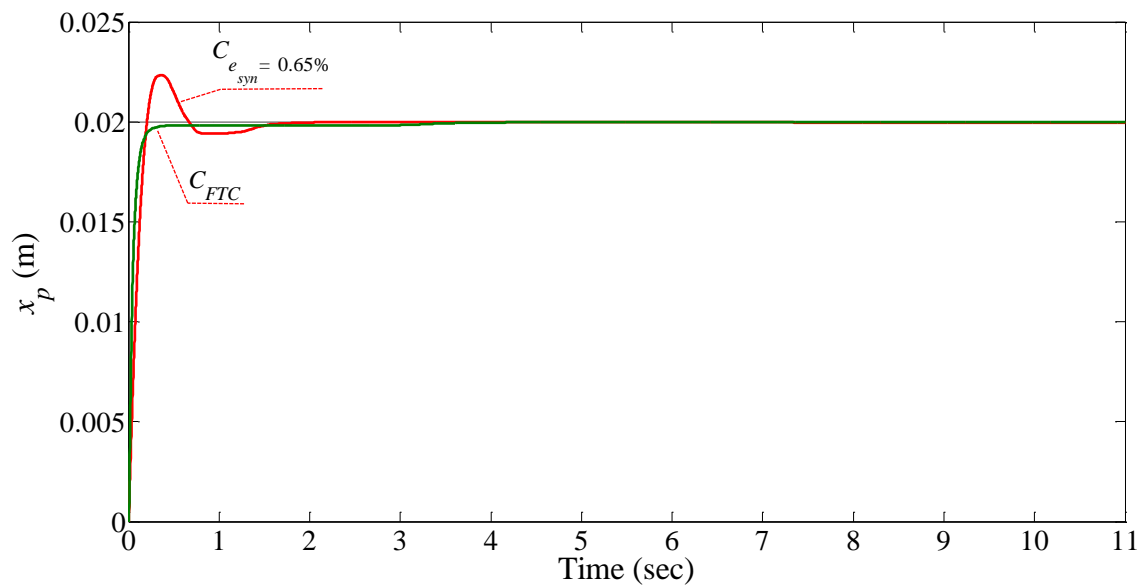


**Figure A.3** Tracking responses to step input of 20 mm when there is a large internal leakage ( $\bar{Q}_i = 11.19$  L/min). No prefilter is used.

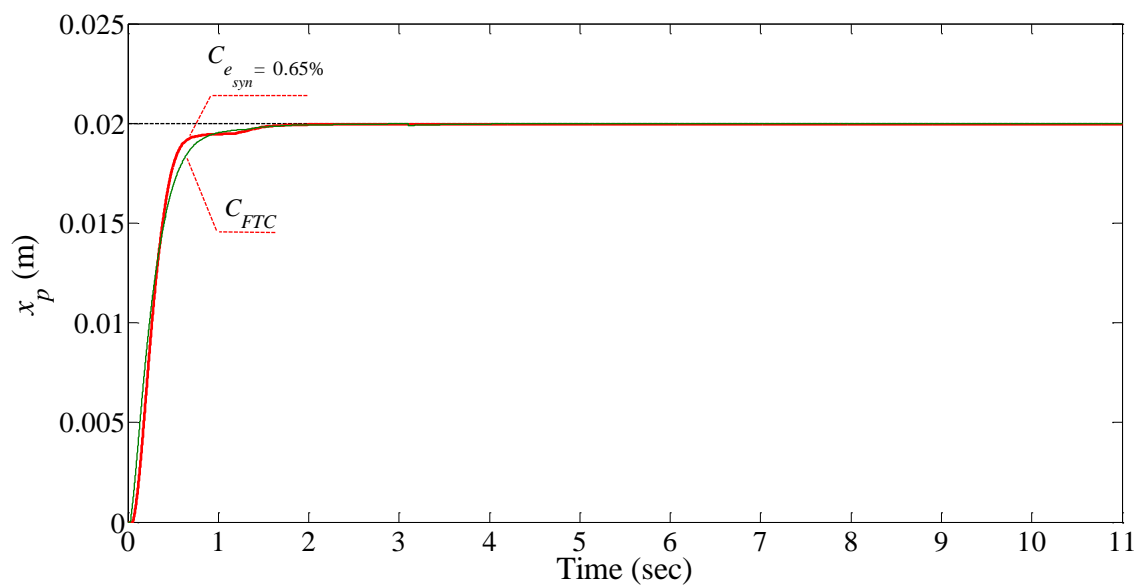


**Figure A.4** Tracking responses to step input of 20 mm with prefilter and large internal leakage ( $\bar{Q}_i = 11.3$  L/min).

To show that the designed FTC does not generate control signals exceeding the threshold values (*i.e.*,  $\pm 10$  Volts), the control signals were obtained when the FTC was used in the closed-loop hydraulic system with and without the prefilter in “no leakage” operating mode (Figure A.5).

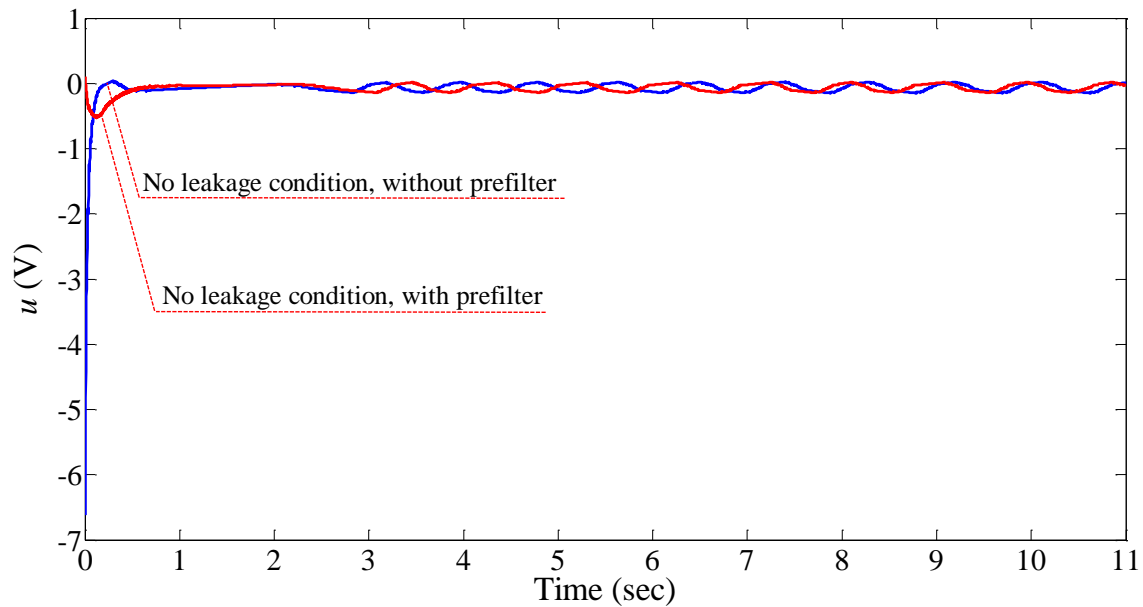


**Figure A.5** Control signals generated by FTC in healthy operating mode with and without prefilter.

## APPENDIX B – STABILITY ANALYSIS

In this appendix, an analysis has been carried out to prove stability of the hydraulic actuator when fault-tolerant controller of (6.8) is used in the *healthy operating mode*. The reason for performance of stability analysis only for the healthy condition is that the value of  $K_i$ , used in the FTC structure, affects the system performance more in healthy operating mode than in other conditions (*i.e.*, faulty modes). In fact, the more the level of synthetic error (*i.e.*, level of the internal leakage in real operating conditions) is, the less the amount of overshoot and oscillations will be in the system response. Therefore, the healthy operating mode is considered as an extreme condition when FTC of (6.8) is used. However, the same stability analysis can be performed on other faulty conditions as well.

For the stability analysis, an experiment was conducted first to capture input-output data from the test rig. The input signal was defined as an alternating step input shown in Figure B.1. It was then given to the servovalve, and piston displacement data was then measured using the position encoder (see Figure B.2). A set of transfer functions, describing the behavior of hydraulic actuator, was obtained from the experimental data based on the vector fitting technique. Details on the vector fitting-based system identification technique are provided in [113]. The transfer functions are found as follows

$$G_1(s) = \frac{1.13s + 0.66}{s^3 + 15.82s^2 + 10.62s + 0.26} \quad (\text{B.1})$$

$$G_2(s) = \frac{343.083s^2 + 615.59s + 96.52}{s^5 + 66.11s^4 + 5215.04s^3 + 8304.04s^2 + 1790.68s + 20.59} \quad (\text{B.2})$$

Transfer functions of (B.1) and (B.2) are obtained by inputting the numbers of zeros and poles to the system identification program [113]. The idea for selection of numbers of zeros and poles was taken from a previous study carried out by Karpenko [14]. One reason behind derivation of two transfer functions from one set of input-output data was to investigate the efficacy of the identification technique in generating transfer functions when different numbers of zeros and poles are used. To ensure the obtained transfer functions can be good representative in describing the behavior of the healthy hydraulic actuator, the same input signal was given to both  $G_1(s)$  and  $G_2(s)$ , and the outputs were compared with the displacement measured by the encoder (*i.e.*, Figure B.2). The outputs of both transfer functions are shown in Figure B.3, which are comparable with the encoder measurements.

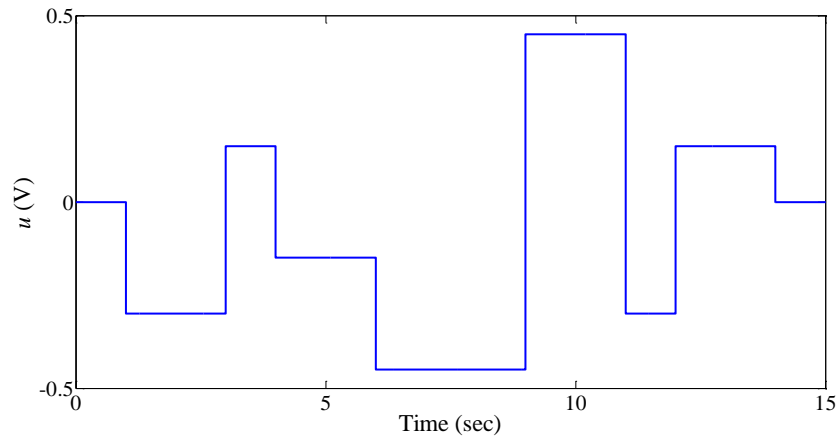


**Figure B.1** Input signal given to servovalve in open-loop configuration.

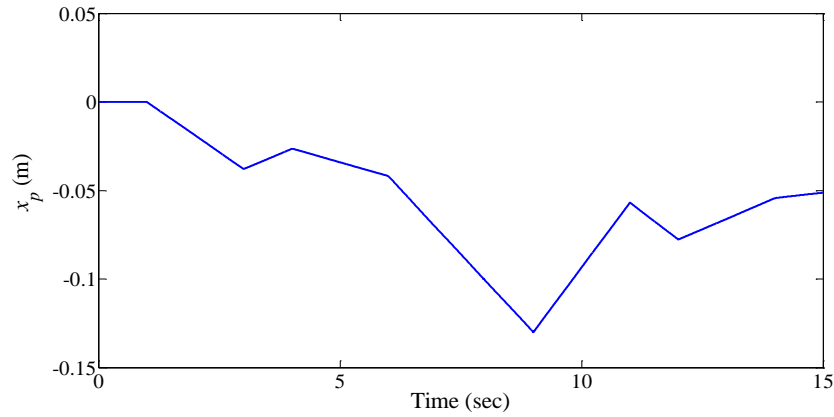


**Figure B.2** Piston displacement data measured by position encoder of test rig.

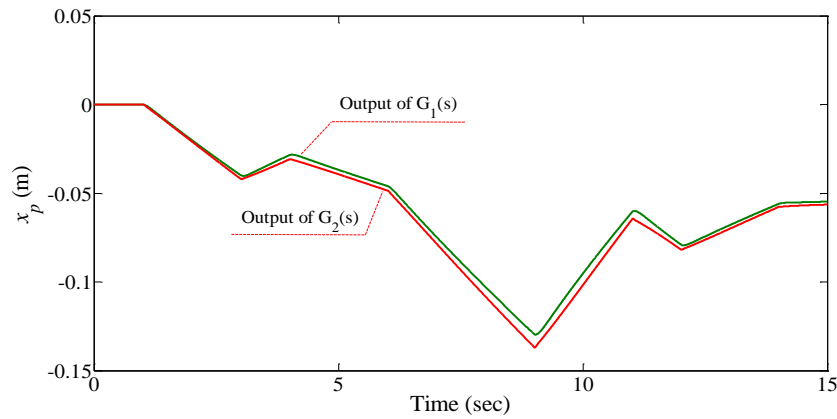


**Figure B.3** Outputs obtained from transfer functions  $G_1(s)$  and  $G_2(s)$ .

With respect to the FOPID-based fault-tolerant controller, there is a need for realization of the fractional-order operators to be usable in real applications. This is already done using Oustaloup recursive technique (see Chapter 5). According to Eq. (5.36) in Chapter 5, the realization form of the fractional-order PID controller is a linear transfer function. Having both transfer functions of the hydraulic actuator [ $G_1(s)$  or  $G_2(s)$ ] and the controller, one can employ well-known techniques of the stability analysis such as Routh-Hurwitz or Nyquist methods to investigate the stability of the closed-loop system. Results of the stability analysis considering both transfer functions  $G_1(s)$  and  $G_2(s)$  are shown in Figures B.4 and B.5 as well as Tables B.1 and B.2. Figures B.4 and B.5

show that Nyquist diagrams do not encircle the point  $(-1, 0)$  when the FTC of (6.8) is used in the closed-loop hydraulic actuator, and the system is therefore stable. Results of the Routh-Hurwitz stability analysis are also given in Tables B.1 and B.2 which illustrate that there is no change in the sign of values listed in the first column. As a result, the closed-loop healthy hydraulic actuator, which includes the FTC of (6.8), is stable. Another interesting alternative for the stability analysis is to model the hydraulic actuator with piecewise-affine system formulations or approximate it as a linear system with polytopic parameter uncertainties, and then, use some classical techniques to prove the stability.

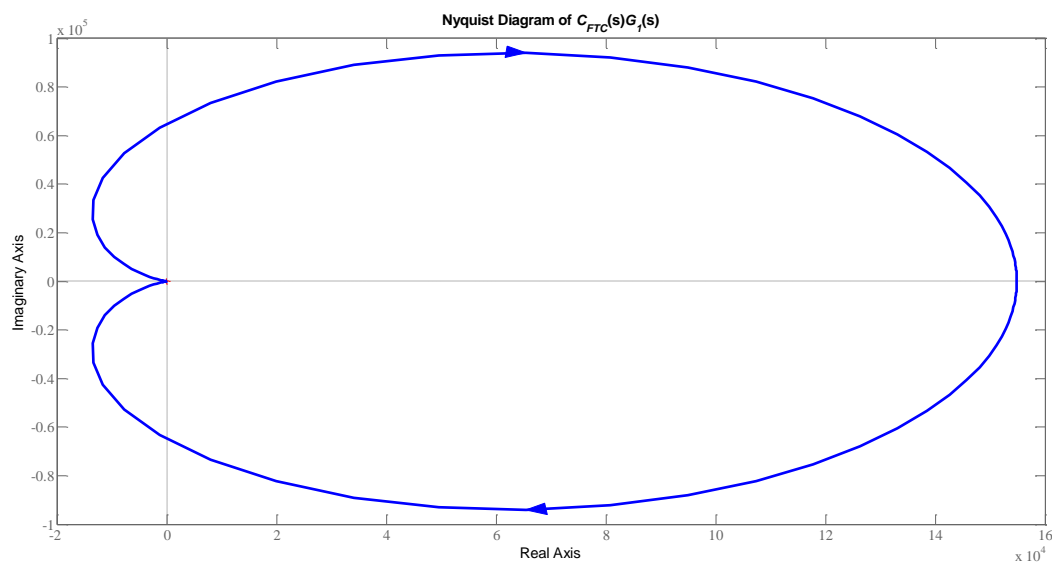


**Figure B.4** Nyquist diagram of open-loop transfer function  $C_{FTC}(s)G_1(s)$

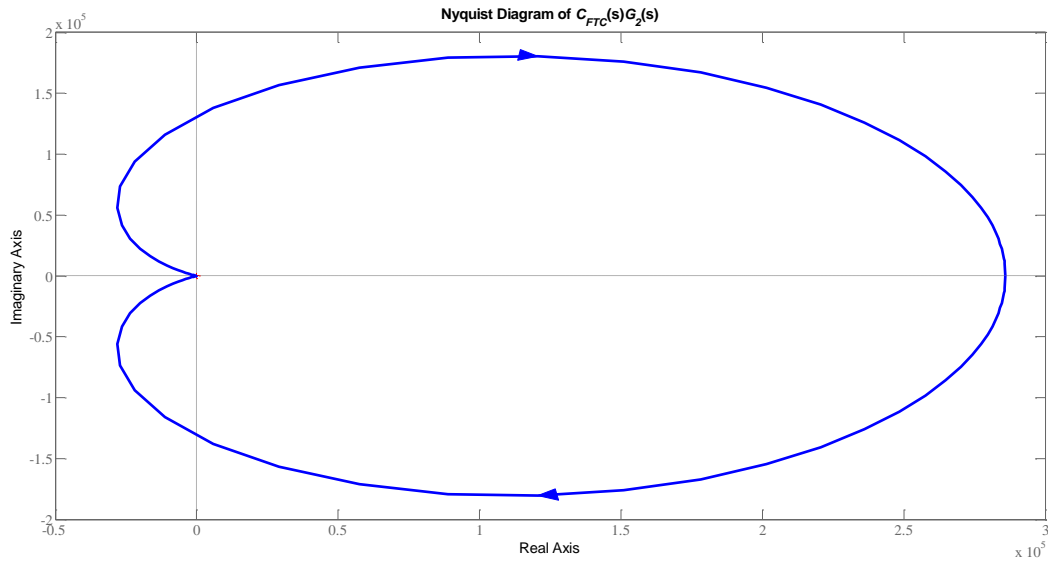


**Figure B.5** Nyquist diagram of open-loop transfer function  $C_{FTC}(s)G_2(s)$

**Table B.1** Result of Routh-Hurwitz stability analysis considering  $G_1(s)$  as plant transfer function.

<b>1</b>	8.0E+04	2.3E+08	1.0E+11	6.5E+12	4.6E+13	3.1E+13	1.8E+12	5.5E+09
<b>4.9E+02</b>	5.8E+06	5.8E+09	1.1E+12	2.3E+13	5.1E+13	1.1E+13	1.6E+11	6.5E+07
<b>6.8E+04</b>	2.2E+08	9.7E+10	6.5E+12	4.6E+13	3.1E+13	1.8E+12	5.5E+09	0
<b>4.2E+06</b>	5.1E+09	1.0E+12	2.3E+13	5.1E+13	1.1E+13	1.5E+11	6.5E+07	0
<b>1.3E+08</b>	8.1E+10	6.1E+12	4.5E+13	3.1E+13	1.8E+12	5.5E+09	0	0
<b>2.6E+09</b>	8.2E+11	2.1E+13	5.0E+13	1.1E+13	1.5E+11	6.5E+07	0	0
<b>3.8E+10</b>	5.0E+12	4.2E+13	3.1E+13	1.8E+12	5.5E+09	0	0	0
<b>4.8E+11</b>	1.8E+13	4.8E+13	1.0E+13	1.5E+11	6.5E+07	0	0	0
<b>3.5E+12</b>	3.8E+13	3.0E+13	1.8E+12	5.5E+09	0	0	0	0
<b>1.3E+13</b>	4.4E+13	1.0E+13	1.5E+11	6.5E+07	0	0	0	0
<b>2.7E+13</b>	2.7E+13	1.8E+12	5.5E+09	0	0	0	0	0
<b>3.0E+13</b>	9.3E+12	1.5E+11	6.5E+07	0	0	0	0	0
<b>1.9E+13</b>	1.6E+12	5.4E+09	0	0	0	0	0	0
<b>6.6E+12</b>	1.4E+11	6.5E+07	0	0	0	0	0	0
<b>1.2E+12</b>	5.2E+09	0	0	0	0	0	0	0
<b>1.1E+11</b>	6.5E+07	0	0	0	0	0	0	0
<b>4.5E+09</b>	0	0	0	0	0	0	0	0
<b>6.5E+07</b>	0	0	0	0	0	0	0	0

**Table B.2** Result of Routh-Hurwitz stability analysis considering  $G_2(s)$  as plant transfer function.

<b>1</b>	1.1E+05	8.8E+08	1.5E+12	3.5E+14	9.2E+15	3.0E+16	1.1E+16	3.7E+14	8.5E+11
<b>5.4E+02</b>	1.2E+07	4.6E+10	3.1E+13	2.4E+15	2.2E+16	2.4E+16	2.7E+15	2.6E+13	9.6E+09
<b>8.7E+04</b>	7.9E+08	1.5E+12	3.5E+14	9.2E+15	3.0E+16	1.1E+16	3.7E+14	8.5E+11	0
<b>6.8E+06</b>	3.7E+10	2.8E+13	2.3E+15	2.1E+16	2.4E+16	2.7E+15	2.6E+13	9.6E+09	0
<b>3.3E+08</b>	1.1E+12	3.2E+14	8.9E+15	2.9E+16	1.1E+16	3.7E+14	8.5E+11	0	0
<b>1.3E+10</b>	2.2E+13	2.1E+15	2.1E+16	2.3E+16	2.7E+15	2.6E+13	9.6E+09	0	0
<b>5.8E+11</b>	2.7E+14	8.4E+15	2.9E+16	1.1E+16	3.7E+14	8.5E+11	0	0	0
<b>1.6E+13</b>	1.9E+15	2.0E+16	2.3E+16	2.7E+15	2.6E+13	9.6E+09	0	0	0
<b>1.9E+14</b>	7.7E+15	2.8E+16	1.1E+16	3.7E+14	8.5E+11	0	0	0	0
<b>1.3E+15</b>	1.8E+16	2.2E+16	2.7E+15	2.6E+13	9.6E+09	0	0	0	0
<b>5.0E+15</b>	2.5E+16	1.0E+16	3.7E+14	8.5E+11	0	0	0	0	0
<b>1.1E+16</b>	2.0E+16	2.6E+15	2.6E+13	9.6E+09	0	0	0	0	0
<b>1.6E+16</b>	9.1E+15	3.6E+14	8.4E+11	0	0	0	0	0	0
<b>1.3E+16</b>	2.3E+15	2.5E+13	9.6E+09	0	0	0	0	0	0
<b>6.3E+15</b>	3.2E+14	8.3E+11	0	0	0	0	0	0	0
<b>1.6E+15</b>	2.4E+13	9.6E+09	0	0	0	0	0	0	0
<b>2.3E+14</b>	7.9E+11	0	0	0	0	0	0	0	0
<b>1.8E+13</b>	9.6E+09	0	0	0	0	0	0	0	0
<b>6.7E+11</b>	0	0	0	0	0	0	0	0	0
<b>9.6E+09</b>	0	0	0	0	0	0	0	0	0

## REFERENCES

- [1] G. Altare and A. Vacca, "A design solution for efficient and compact electro-hydraulic actuators," *Procedia Engineering*, vol. 106, pp. 8-16, 2015.
- [2] X. Cui, S. Wang, Q. Li and J. Shi, "Reliability assessment of aircraft power and actuation system based on three-axis control," in *IEEE International Conference on Advanced Intelligent Mechatronics*, pp. 382-387, Busan, Korea, July 07, 2015.
- [3] Z. Wang, R. Duan, G. Sun and M. Chi, "Hydraulic quadruped robot joint force control based on double internal model controller," *Int. Journal of Control and Automation*, vol. 9, no. 1, pp. 241-250, 2016.
- [4] H. Kaminaga, S. Otsuki and Y. Nakamura, "Design of an ankle-knee joint system of a humanoid robot with a linear electro-hydrostatic actuator driven parallel ankle mechanism and redundant biarticular actuators," in *IEEE-RAS International Conference on Humanoid Robots (Humanoids)*, pp. 384-389, Atlanta, USA, Oct. 15, 2013.
- [5] B. B. Ghosh, B. K. Sarkar and R. Saha, "Realtime performance analysis of different combinations of fuzzy-PID and bias controllers for a two degree of freedom electrohydraulic parallel manipulator," *Robotics and Computer-Integrated Manufacturing*, vol. 34, pp. 62-69, 2015.
- [6] W. Y. Lee, M. J. Kim and W. K. Chung, "An approach to development of electro hydrostatic actuator (EHA)-based robot joints," in *IEEE International Conference on Industrial Technology*, pp. 99-106, Seville, Spain, Mar. 17, 2015.
- [7] M. Karpenko and N. Sepehri, "On quantitative feedback design for robust position control of hydraulic actuators," *Control Engineering Practice*, vol. 18, no. 3, pp. 289-299, 2010.
- [8] M. Karpenko and N. Sepehri, "Quantitative fault tolerant control design for a leaking hydraulic actuator," *Journal of Dynamic Systems, Measurement and Control*, vol. 132, no. 5, pp. 054505-054505-7, 2010.
- [9] M. Karpenko and N. Sepehri, "Hardware-in-the-loop simulator for research on fault tolerant control of electrohydraulic actuators in a flight control application," *Mechatronics*, vol. 19, no. 7, pp. 1067-1077, 2009.
- [10] C. Alozie, "Internal leakage diagnosis in valve controlled acruation systems and electrohydrostatic actuation systems," M.Sc. thesis, Winnipeg, MB, Canada, 2014.

- [11] A. Y. Goharrizi and N. Sepehri, "Application of fast Fourier and wavelet transforms towards actuator leakage diagnosis: A comparative study," *Int. Journal of Fluid Power*, vol. 14, no. 2, pp. 39-51, 2013.
- [12] A. Maddahi, W. Kinsner and N. Sepehri, "Internal leakage detection in electrohydrostatic actuators using multiscale analysis of experimental data," *IEEE Transactions on Instrumentation and Measurement*, vol. 65, no. 12, pp. 2734-2747, 2016.
- [13] J. C. Sprott, *Chaos and Time-Series Analysis*, Oxford: Oxford Univ. Press, 2003, p. 507.
- [14] A. Y. Goharrizi, "Leakage detection in hydraulic actuators based on wavelet transform," Ph.D. thesis, Winnipeg, MB, Canada, 2011.
- [15] M. Karpenko, "Quantitative fault tolerant control design for a hydraulic actuator with a leaking piston seal," Ph.D. thesis, Winnipeg, MB, Canada, 2008.
- [16] W. Kinsner, "A unified approach to fractal dimensions," *Int. Journal of Cognitive Informatics and Natural Intelligence*, vol. 1, no. 4, pp. 26-46, 2007.
- [17] W. Kinsner, *Polyscale analysis and fractional operators for cognitive systems*, London, UK: Keynote Talk, p. 6, Aug. 18-20, 2014.
- [18] M. Karpenko, "Fault tolerant control design for an electrohydraulic actuator with application to positioning of aircraft flight control surfaces," M.Sc. thesis, Winnipeg, MB, Canada, 2002.
- [19] H. Tan and N. Sepehri, "Parametric fault diagnosis for electrohydraulic cylinder drive units," *IEEE Transactions on Industrial Electronics*, vol. 49, no.1, pp. 96-106, 2002.
- [20] T. T. Le, J. Watton and D. T. Pham, "Fault classification of fluid power system using a dynamic feature extraction technique and neural networks," *Journal of Systems and Control Engineering*, vol. 211, no. 2, pp. 87-97, 1998.
- [21] Z. Shi, F. Gu, B. Lennox and A. D. Ball, "The development of an adaptive threshold for model-based fault detection of a nonlinear electro-hydraulic system," *Control Engineering Practice*, vol. 13, no. 11, pp. 1357-1367, 2005.
- [22] P. M. Frank, "On-line fault detection in uncertain nonlinear system using diagnostic observers: A survey," *Int. Journal of Systems Science*, vol. 25, no. 12, pp. 2129-2154, 1994.
- [23] D. Yu, D. N. Shields and J. L. Mahtani, "Fault detection for bilinear systems with application to a hydraulic system," in *Proc. of IEEE Conf. Control Appl.*, pp. 1379-1384, Glasgow, UK, Aug. 24-26, 1994.
- [24] L. An and N. Sepehri, "Hydraulic actuator leakage fault detection using extended Kalman filter," *Int. Journal of Fluid Power*, vol. 6, no. 1, pp. 41-51, 2005.
- [25] X. Wang and V. L. Syrmos, "Fault detection, identification and estimation in electrohydraulic actuator system using EKF-based multiple-model estimation," in *Proc. 16th Mediterranean Conf. Control and Automation*, pp. 1693-1698, Ajaccio, France, June 25, 2008.

- [26] H. H. Afshari, S. A. Gadsden and S. R. Habibi, "Robust fault diagnosis of an electro-hydrostatic actuator using the novel dynamic second-order SVSF and IMM strategy," *Int. Journal of Fluid Power*, vol. 15, no. 3, pp. 181-196, 2014.
- [27] H. Liu, D. Liu, C. Lu and X. Wang, "Fault diagnosis of hydraulic servo system using the unscented Kalman filter," *Asian Journal of Control*, vol. 16, no. 6, pp. 1713-1725, 2014.
- [28] A. Y. Goharrizi and N. Sepehri, "A wavelet-based approach for external leakage detection and isolation from internal leakage in valve-controlled hydraulic actuators," *IEEE Transactions on Industrial Electronics*, vol. 58, no. 9, pp. 4374-4384, 2011.
- [29] A. Y. Goharrizi and N. Sepehri, "Internal leakage detection in hydraulic actuators using empirical mode decomposition and Hilbert spectrum," *IEEE Transactions on Instrumentation and Measurement*, vol. 61, no. 2, pp. 368-378, 2012.
- [30] W. Kinsner, *Fractal and chaos engineering*, Winnipeg, MB: Lecture Notes, University of Manitoba, 2015.
- [31] Y. Li, X. M., Y. Wei and W. Huang, "A new rolling bearing fault diagnosis method based on multiscale permutation entropy and improved support vector machine based binary tree," *Journal of Measurement*, vol. 77, pp. 80-94, 2016.
- [32] D. You, X. Gao and S. Katayama, "WPD-PCA-based laser welding process monitoring and defects diagnosis by using FNN and SVM," *IEEE Transactions on Industrial Electronics*, vol. 62, no. 1, pp. 628-636, 2015.
- [33] W. Jiang, Z. Zheng, Y. Zhu and Y. Li, "Demodulation for hydraulic pump fault signals based on local mean decomposition and improved adaptive multiscale morphology analysis," *Journal of Mechanical Systems and Signal Processing*, vol. 58, pp. 179-205, 2015.
- [34] P. Sekhavat, N. Sepehri and Q. Wu, "Impact stabilizing controller for hydraulic actuators with friction: theory and experiments," *Control Engineering Practice*, vol. 14, no.12, pp. 1423-1433, 2006.
- [35] J. Seo, R. Venugopal and J. P. Kenne, "Feedback linearization based control of a rotational hydraulic drive," *Control Engineering Practice*, vol. 15, no.12, pp. 1495-1507, 2007.
- [36] P. Nakkarat and S. Kuntanapreeda, "Observer-based backstepping force control of an electrohydraulic actuator," *Control Engineering Practice*, vol. 17, no. 8, pp. 895-902, 2009.
- [37] N. Niksefat and N. Sepehri, "Fault tolerant control of electrohydraulic servo positioning systems," in *Proc. American Control Conference*, vol. 6, pp. 4472-4477, Arlington, USA, Jun. 25-27 2001.
- [38] N. Niksefat and N. Sepehri, "A QFT fault tolerant control for electrohydraulic positioning systems," *IEEE Transactions on Control Systems Technology*, vol. 10, no. 4, pp. 626-632, 2002.

- [39] M. Karpenko and N. Sepehri, "Robust position control of an electrohydraulic actuator with a faulty actuator piston seal," *Journal of Dynamic Systems, Measurement, and Control*, vol. 125, no. 3, pp. 413-423, 2003.
- [40] M. Karpenko and N. Sepehri, "Fault-tolerant control of a servohydraulic positioning system with crossport leakage," *IEEE Transactions on Control Systems Technology*, vol. 13, no. 1, pp. 155-161, 2005.
- [41] Y. M. Zhang and J. Jiang, "Active fault-tolerant control system against partial actuator failures," in *IEEE Proc. of Control Theory Applications*, vol. 149, no. 1, pp. 95-104, 2002.
- [42] Y. Chen, B. M. Vinagre and I. Podlubny, "Continued fraction expansion approaches to discretizing fractional order derivatives – an expository review," *Nonlinear Dynamics*, vol. 38, no. 1-4, pp. 155-170, 2004.
- [43] A. Carpinteri, B. Chiaia, P. D. Panagiotopoulos, R. Lenormand, R. Gorenflo and F. Mainardi, *Fractals and Fractional Calculus in Continuum Mechanics*, Vienna: Springer-Verlag Wien, 1997.
- [44] B. M. Vinagre, I. Podlubny, A. Hernandez and V. Feliu, "Some approximations of fractional order operators used in control theory and applications," *Fractional calculus and applied analysis*, vol. 3, no. 3, pp. 231–248, 2000.
- [45] A. Oustaloup, F. Levron, B. Mathieu and F. M. Nanot, "Frequency-band complex noninteger differentiator: characterization and synthesis," *IEEE Transactions Circuits and Systems-I: Fundamental Theory and Applications*, vol. 47, no. 1, pp. 25–39, 2000.
- [46] A. Chareff, H. H. Sun, Y. Y. Tsao and B. Onaral, "Fractal system as represented by singularity function," *IEEE Transactions on Automatic Control*, vol. 37, no. 9, pp. 1465-1470, 1992.
- [47] S. C. D. Roy, "On the realization of a constant-argument immittance or fractional operator," *IEEE Transactions on Circuit Theory*, vol. 14, no. 3, pp. 264–274, 1967.
- [48] G. E. Carlson and C. A. Halijak, "Approximation of fractional capacitors  $(1/s)^{1/n}$  by a regular Newton process," *IEEE Transactions on Circuit Theory*, vol. 11, no. 2, pp. 210–213, 1964.
- [49] K. Matsuda and H. Fujii, " $H_\infty$  optimized wave-absorbing control: analytical and experimental results," *Journal of Guidance, Control, and Dynamics*, vol. 16, no. 6, pp. 1146-1153, 1993.
- [50] A. Karimi, L. Miskovic and D. Bonvin, "Iterative correlation-based controller tuning," *International Journal of Adaptive Control and Signal Processing*, vol. 18, no. 8, pp. 645-664, 2004.
- [51] M. C. Campi, A. Lecchini and S. M. Savaresi, "Virtual reference feedback tuning: a direct method for the design of feedback controllers," *Automatica*, vol. 38, no. 8, pp. 1337-1346, 2002.

- [52] Y. Li, X. Meng, B. Zheng and Y. Ding, "Parameter identification of fractional order linear system based on Haar wavelet operational matrix," *ISA Transactions*, vol. 59, pp. 79-84, 2015.
- [53] K. J. Astrom and T. Hagglund, *PID Controllers: Theory, Design and Tuning*, Research Triangle Park, NC: International Society for Measurement and Controls, 1995.
- [54] V. Shekher, P. Rai and P. O., "Tuning and analysis of fractional order PID controller," *International Journal of Electronic and Electrical Engineering*, vol. 5, no. 1, pp. 11-21, 2012.
- [55] H. Hjalmarsson, M. Gevers, S. Gunnarsson and O. Lequin, "Iterative feedback tuning: theory and applications," *IEEE Control Systems*, vol. 18, no. 4, pp. 26-41, 1998.
- [56] B. Xu, D. Chen, H. Zhang and F. Wang, "Modeling and stability analysis of a fractional-order Francis hydro-turbine governing system," *Chaos, Solitons & Fractals*, vol. 75, pp. 50-61, 2015.
- [57] U. S. Banu and A. W. Nasir, "Design, analysis and performance evaluation of fractional order proportional integral for three interacting tank process in frequency domain considered as third order system," *IFAC-PapersOnLine*, vol. 48, no. 30, pp. 179-184, 2015.
- [58] Y. Xu, J. Zhou, X. Xue, W. Fu, W. Zhu and C. Li, "An adaptively fast fuzzy fractional order PID control for pumped storage hydro unit using improved gravitational search algorithm," *Energy Conversion and Management*, vol. 111, pp. 67-78, 2016.
- [59] P. Roy and B. K. Roy, "Fractional order PI control applied to level control in coupled two tank MIMO system with experimental validation," *Control Engineering Practice*, vol. 48, pp. 119-135, 2016.
- [60] C. Izaguirre-Espinosa, A. J. Muñoz-Vázquez, A. Sánchez-Orta, V. Parra-Vega and G. Sanahuja, "Fractional attitude-reactive control for robust quadrotor position stabilization without resolving underactuation," *Control Engineering Practice*, vol. 53, pp. 47-56, 2016.
- [61] P. Lanusse, D. N. Gruel, A. Lamara, A. Lesobre, X. Wang, Y. Chamailard and A. Oustaloup, "Development of a fractional order based MIMO controller for high dynamic engine testbeds," *Control Engineering Practice*, vol. 56, pp. 174-189, 2016.
- [62] J. Ma, Y. Yao and D. Liu, "Fractional order model reference adaptive control for a hydraulic driven flight motion simulator," in *IEEE 41<sup>st</sup> Southeastern Symposium on System Theory*, pp. 340-343, Tullahoma, USA, 2009.
- [63] Z. Jiangbo, W. Junzheng and W. Shoukun, "Fractional order control to the electro-hydraulic system in insulator fatigue test device," *Mechatronics*, vol. 23, no. 7, pp. 828-839, 2013.
- [64] Z. Jiangbo and W. Junzheng, "The fractional order PI control for an energy saving electro-hydraulic system," *Transactions on the Institute of Measurement and Control*, vol. 39, no. 4, pp. 505-519, 2017.
- [65] Q. Gao, Y. Hou, T. Deng, C. Wang and R. Hou, "Extended state observer-based fractional order proportional-integral-derivative controller for a novel electro-hydraulic servo system

- with iso-actuation balancing and positioning," *Advances in Mechanical Engineering*, vol. 7, no. 12, pp. 1-11, 2015.
- [66] A. Rajasekhar, S. Das and P. N. Suganthan, "Design of fractional order controller for a servohydraulic positioning system with micro artificial bee colony algorithm," in *2012 IEEE Congress on Evolutionary Computation*, pp. 1-8, Brisbane, Australia, June 10-15, 2012.
- [67] A. Kavas and D. G. Feitelson, "Comparing Windows, NT, Linux, and QNX as the basis for cluster systems," *J. of Concurrency and Computation: Practice and Experience*, vol. 13, no. 15, pp. 1303-1332, 2001.
- [68] G. Ren, M. Esfandiari, J. Song and N. Sepehri, "Position control of an electrohydrostatic actuator with tolerance to internal leakage," *IEEE Transactions on Control Systems Technology*, vol. 24, no. 6, pp. 2224-2232, 2016.
- [69] Z. M. Hussain, A. Z. Sadik and P. O'Shea, *Digital signal processing: An introduction with MATLAB and applications*, Springer-Verlag Berlin Heidelberg, 2011.
- [70] L. A. Smith, "Intrinsic limits on dimension calculations," *Physics Letter A*, vol. 133, no. 6, pp. 283-288, 1988.
- [71] M. Ding, E. Grebogi, E. Ott, T. Sauer and J. Yorke, "Plateau onset for correlation dimension: when does it occur?," *Physical Review Letter*, vol. 70, no. 25, pp. 3872-3875, 1993.
- [72] A. C. Tsonis, *Chaos: From Theory to Applications*, New York, NY: Plenum, 1992.
- [73] M. T. Rosenstein, J. J. Collins and C. J. De Luca, "A practical method for calculating largest Lyapunov exponents from small data sets," *Phys. D, Nonlinear Phenomena*, vol. 65, no. 1-2, pp. 117-134, 1993.
- [74] A. M. Fraser and H. L. Swinney, "Independent coordinates for strange attractors from mutual information," *Phys. Rev. A*, vol. 33, no. 2, pp. 1134-1140, 1986.
- [75] A. M. Fraser, "Reconstructing attractors from scalar time series: A comparison of singular system and redundancy criteria," *Phys. D, Nonlinear Phenomena*, vol. 34, no. 3, pp. 391-404, 1989.
- [76] F. J. Pineda and J. C. Sommerer, "Estimating generalized dimensions and choosing time delays: A fast algorithm," *Time Series Prediction: Forecasting the Future and Understanding the Past*, vol. 15, pp. 367-385, 1993.
- [77] F. Takens, *Detecting strange attractors in turbulence*, vol. 898, D. R. a. L. Young, Ed., pp. 366-381, New York, USA, NY: Springer, 1981.
- [78] T. Sauer, J. A. Yorke and M. Casdagli, "'Embedology,'" *J. Statist. Phys.*, vol. 65, no. 3, pp. 579-616, 1991.
- [79] P. Grassberger and I. Procaccia, "Characterization of strange attractors," *Phys. Rev. Lett.*, vol. 50, no. 5, pp. 346-349, 1983.

- [80] D. S. Broomhead and G. P. King, "Extracting qualitative dynamics from experimental data," *Phys. D, Nonlinear Phenomena*, vol. 20, no. 2-3, pp. 217-236, 1986.
- [81] M. B. Kennel, R. Brown and H. D. I. Abarbanel, "Determining embedding dimension for phase-space reconstruction using a geometrical construction," *Phys. Rev. A*, vol. 45, no.6, pp. 3403-3411, 1992.
- [82] L. Cao, "Practical method for determining the minimum embedding dimension of a scalar time series," *Phys. D, Nonlinear Phenomena*, vol. 110, no. 1-2, pp. 43-50, 1997.
- [83] L. Jiao, W. Moon and W. Kinsner, "Variance fractal dimension analysis of seismic refraction signals," in *Conf. Proc. IEEE on Communications*, Winnipeg, MB, Canada, May 22-23, 1997.
- [84] W. Kinsner, V. Cheung, K. Cannons, J. Pear and T. Martin, "Signal classification through multifractal analysis and complex domain neural networks," *IEEE Transactions on Systems, Man, and Cybernetics- Part C: Applications and Review*, vol. 36, no. 2, pp. 196-203, 2006.
- [85] R. Gencay and W. D. Dechert, "An algorithm for the n Lyapunov exponents of an n-dimensional unknown dynamical system," *Physica D*, vol. 59, no. 1-3 pp. 142-157, 1992.
- [86] A. Wolf, S. J. B., H. L. Swinney and J. A. Vastano, "Determining Lyapunov exponents from a time-series," *Physica D*, vol. 16, no. 3, pp. 285-317, 1985.
- [87] T. M. Krueel, M. Esworth and F. W. Schreider, *Introduction to non-linear mechanics*, Princeton, NJ: Princeton Univ. Press, 1993.
- [88] Y. B. Pesin, "Characteristic Lyapunov exponents and smooth ergodic theory," *Russian Mathematical Survey*, vol. 32, no. 4, pp. 55-114, 1977.
- [89] P. Grassberger and I. Procaccia, "Measuring the strangeness of strange attractors," *Physica D*, vol. 9, no. 1-2, pp. 189-208, 1983.
- [90] P. Grassberger and I. Procaccia, "Estimation of the kolmogrov entropy from a chaotic signal," *Physica Review A*, vol. 28, no. 4, pp. 2591-2593, 1983.
- [91] A. Cohen and I. Procaccia, "Computing the Kolmogorov entropy time signals of dissipative and conservative dynamical systems," *Physical Review A*, vol. 31, no. 3, pp. 1872-1882, 1985.
- [92] C. S. Burrus, R. A. Gopinath and H. Gwa, *Introduction to wavelets and wavelet transforms*, Prentice Hall, 1998.
- [93] A. Ukil and R. Zivanovic, "Abrupt change detection in power system fault analysis using adaptive whitening filter and wavelet transform," *Electric Power Systems Research*, vol. 76, no. 9-10, pp. 815-823, 2006.
- [94] S. Mallat, "A theory for multiresolution signal decomposition: The wavelet representation," *IEE Transactions on Pattern Analysis and Machine Intelligence*, vol. 11, no. 7, pp. 674-693, 1989.

- [95] G. Strang and N. T., Wavelet and filter banks, Wellesley-Cambridge Press, 1996.
- [96] J. Cusido, L. Romeral, J. A. Ortega, J. A. Rosero and A. G. Espinosa, "Fault detection in induction machines using power spectral density in wavelet decomposition," *IEEE Transactions on Industrial Electronics*, vol. 55, no. 2, pp. 633-643, 2008.
- [97] G. Jumarie, "Modified Riemann-Liouville derivative and fractional Taylor series of nondifferentiable functions further results," *Computers and Mathematics with Applications*, vol. 51, no. 9-10, pp. 1367-1376, 2006.
- [98] X. Wang, "Fractional geometric calculus: Toward a unified mathematical language for physics and Engineering," *Proc. of the 5<sup>th</sup> Symposium on Fractional Differentiation and its Applications*, pp. 1-6, Nanjing, China, 2012.
- [99] C. F. M. Coimbra, "Mechanics with variable-order differential operators," *Annalen der Physik*, vol. 12, no. 11-12, pp. 692-703, 2003.
- [100] M. T. Nasri and W. Kinsner, "An evaluation of integer- and fractional-order controllers for small satellites," in *IEEE 13<sup>th</sup> Int. Conf. on Cognitive Informatics and Cognitive Computing*, pp. 30-38, London, UK, Aug 18-20, 2014.
- [101] D. Eager, A.-M. Pendrill and N. Reistad, "Beyond velocity and acceleration: jerk, snap and higher derivatives," *European Journal of Physics*, vol. 37, no. 6, pp. 1-11, 2016.
- [102] M. Moshrefi-Torbati and J. K. Hammond, "Physical and geometrical interpretation of fractional operators," *J. of Franklin Institute*, vol. 335B, no. 6, pp. 1077-1086, 1998.
- [103] J. F. Gomez-Aguilar, R. Razo-Hernandez and D. Granados-Lieberman, "A physical interpretation of fractional calculus in observable terms: analysis of the fractional time constancy and the transitory response," *Revista Mexicana de Fisica*, vol. 60, no. 1, pp. 32-38, 2014.
- [104] M. H. Tavassoli, A. Tavassoli and M. R. Ostad Rahimi, "The geometric and physical interpretation of fractional order derivatives of polynomial functions," *Differential Geometry - Dynamical Systems*, vol. 15, pp. 93-104, 2013.
- [105] H. Prochazka, M. Gevers, B. D. O. Anderson and C. Ferrera, "Iterative feedback tuning for robust controller design and optimization," in *IEEE 44<sup>th</sup> Conf. on Design and Control, and European Control Conf.*, pp. 3602-3607, Seville, Spain, Dec. 15, 2005.
- [106] D. W. Marquardt, "An algorithm for least-squares estimation of nonlinear parameters," *J. of Society for Industrial and Applied Mathematics*, vol. 11, no. 2, pp. 431-441, 1963.
- [107] D. A. Haessig and B. Friedland, "On the modeling and simulation of friction," *J. of Dynamic Systems, Measurement, and Control*, vol. 113, no. 3, pp. 354-362, 1991.
- [108] B. Armstrong and C. C. de Wit, "Friction modeling and compensation," in *The Control Handbook*, pp. 1369-1382, CRC Press, 1996.
- [109] H. C. Pederson, T. O. Anderson and J. Liniger, "Investigation of load reduction possibilities in wind turbines using a fluid power pitch systems," in *Proc. of ASME/BATH 2015*

- Symposium on Fluid Power & Motion Control*, pp. V001T01A051-V001T01A051, Chicago, USA, Oct. 12-14, 2015.
- [110] C. H. Houpis and S. J. Rasmussen, *Quantitative Feedback Theory: Fundamentals and Applications*, New York, NY: Marcel Dekker, 1999.
- [111] L. N. G. Filon, "On a quadrature formula for trigonometric integrals," in *Proc. of the Royal Society of Edinburgh*, vol. 49, pp. 38-47, 1930.
- [112] M. Karpenko and N. Sepehri, "Equivalent time-invariant modelling of electrohydraulic actuators with application to robust control synthesis," *Int. J. of Fluid Power*, vol. 9, no. 3, pp. 7-18, 2008.
- [113] A. A. Ozdemir and S. Gumussoy, "Transfer Function Estimation in System identification Toolbox via Vector Fitting", *IFAC-PapersOnline*, vol. 50, no. 1, pp. 6232-6237, 2017.